

ABSTRACT

Title of Ph.D. Dissertation: THIN TWO-PHASE HEAT SPREADERS WITH
BOILING ENHANCEMENT MICROSTRUCTURES
FOR THERMAL MANAGEMENT OF ELECTRONIC
SYSTEMS

Sunil S Murthy, Doctor of Philosophy, 2004

Dissertation directed by: Professor Yogendra K. Joshi
Department of Mechanical Engineering

The current study goes over a design methodology for thin, two-phase heat spreaders for space constrained cooling applications. The evaporator section of the heat spreader employs enhancement structures to improve the spreader plate performance. The thermal performances of two such spreader prototypes, with integrated fins for cooling, were studied under both natural convection as well as forced air-cooled conditions. The results show a significant improvement in performance of the spreader plate compared to a solid metal plate subjected to similar boundary conditions. A design constraint on the evaporator and the condenser sections of the heat spreader ensures the enhanced structure remains flooded under all orientations, resulting in an orientation insensitive heat spreader.

A predictive thermal performance model of the spreader plate was developed based on a semi-analytical model for boiling from structured surfaces. The semi-

analytical model was validated against measured quantities from flow visualization studies reported in the literature and was found to predict the bubble departure diameter within $\pm 20\%$, bubble frequency within $\pm 35\%$ and heat fluxes within $\pm 30\%$. 2D numerical simulation, using level set formulation, was also carried out to understand the physics behind bubble departure from structured surfaces.

THIN TWO-PHASE HEAT SPREADERS WITH BOILING ENHANCEMENT
MICROSTRUCTURES FOR THERMAL MANAGEMENT OF ELECTRONIC
SYSTEMS

by

Sunil S. Murthy

Dissertation submitted to the Faculty of the Graduate School of the
University of Maryland, College Park in partial fulfillment
of the requirements for the degree of
Doctor of Philosophy
2004

Advisory Committee:

Professor Yogendra K. Joshi, Chair/Advisor
Assistant Professor Reza Ghodssi
Associate Professor Jungho Kim
Associate Professor Cheng Lee
Professor Michael Ohadi

TABLE OF CONTENTS

LIST OF TABLES	iv
LIST OF FIGURES	v
NOMENCLATURE	xi
CHAPTER 1: INTRODUCTION	1
1.1 Motivation and Background	2
1.2 Literature Review	7
1.2.1 Review of enhanced surfaces in boiling	7
1.2.2 Review of flow visualization studies in boiling from enhanced surfaces	8
1.2.2.1 Nakayama et. al. visualization study	11
1.2.2.2 Arshad and Thome visualization study	11
1.2.2.3 Chien and Webb visualization study	12
1.2.2.4 Ghiu et al. visualization study	13
1.2.3 Analytical models for boiling from structured surfaces	15
1.2.3.1 Nakayama's suction-evaporation model	15
1.2.3.2 Webb and Haider model	16
1.2.3.3 Chien and Webb's suction-evaporation model	17
1.2.3.4 Ramaswamy et al. semi-analytical model	19
1.2.4 Numerical simulation of two-phase flows	19
1.2.4.1 Level set method	21
1.3 Overview of the Current Study	22
CHAPTER 2: EXPERIMENTAL SETUP AND PROCEDURES	24
2.1 Experimental setup	27
2.1.1 Copper prototype: Forced convection	27
2.1.2 Aluminum prototype: Natural convection	29
2.2 Data Acquisition	31
2.3 Experimental Procedures	32
2.4 Uncertainty Analysis	33
CHAPTER 3: TWO-PHASE HEAT SPREADER THERMAL PERFORMANCE	35
3.1 Baseline Study	35
3.2 Effect of Condenser Cooling	39
3.3 Effect of Enhancement Structure Size	41
3.4 Effect of Liquid Fill Ratio	42
3.5 Effect of Starting System Pressure	44
3.6 Effect of Coolant Fluid	48
3.7 Effect of Stack Height	49

3.8 Orientation Study	53
3.9 Summary and Conclusions	56
CHAPTER 4: SEMI-ANALYTICAL MODEL FOR BOILING FROM ENHANCED STRUCTURES	57
4.1 Semi-Analytical Model	59
4.1.1 Modeling bubble departure diameter	60
4.1.2 Modeling tunnel heat transfer	63
4.1.3 Modeling bubble frequency	64
4.1.4 Modeling initial film thickness	68
4.1.5 Modeling external heat transfer	69
4.1.6 Modeling nucleation site density	70
4.1.7 Prediction procedure	70
4.2 Results of Semi-Analytical Model	71
4.2.1 Prediction of departure diameter	72
4.2.2 Prediction of frequency	73
4.2.3 Prediction of heat flux	74
4.2.4 Performance prediction of two-phase heat spreaders	77
4.3 Summary and Conclusions	79
CHAPTER 5: NUMERICAL SIMULATION OF BOILING FROM ENHANCED STRUCTURES	81
5.1 Projection Method	81
5.1.1 Predictor step	84
5.1.2 Projection step	86
5.1.3 Validation of flow solver	88
5.2 Level Set Formulation	90
5.2.1 Level set validation	92
5.3 Numerical Analysis	93
5.4 Solution Algorithm	97
5.5 Numerical Simulation Results	98
5.6 Summary and Conclusions	102
CHAPTER 6: SUMMARY, CONCLUSIONS AND RECOMMENDATIONS FOR FUTURE WORK	104
6.1 Summary	104
6.2 Conclusions	104
6.3 Recommendation for Future Work	106
REFERENCES	109

LIST OF TABLES

Table 1.1: Material properties of composites solids used instead of copper and aluminum metal plates.	5
Table 1.2: Boiling performance of enhanced surfaces in fluorinerts (Ramaswamy, 1999).	9
Table 2.1: Comparison of two-phase thermosyphon performance with that of a solid spreader plate for different condenser conditions.	24
Table 3.1: Transport properties of various liquid coolants (Danielson et al., [1987]).	50
Table 4.1: Geometrical details for the parametric studies in literature.	73
Table 5.1: Convergence study for lid-driven cavity flow.	90

LIST OF FIGURES

Figure 1.1:	Geometric configuration of a model used to study solid heat spreader performance.	3
Figure 1.2:	Variation in thermal resistance with respect to the spreader thickness. Higher thermal conductivity plates result in lower resistance values	3
Figure 1.3:	Enhanced structures for electronics cooling - (a) Anderson and Mudawar (1989), (b) and (c) Oktay (1992), (d) Mudawar and Anderson (1993), (e) Nakayama et al. (1984)	10
Figure 1.4:	Nakayama et al. (1980a) visualization apparatus	12
Figure 1.5:	Liquid-vapor interface in the tunnel, Nakayama et al. (1980a)	12
Figure 1.6:	Arshad and Thome's (1983) conceptual sketches of the boiling phenomena in triangular tunnel	13
Figure 1.7:	Schematic of Chien and Webb's (1998b) visualization experiments	14
Figure 1.8:	Transparent quartz enhancement structures used in Ghiu et al. (2001) visualization studies	14
Figure 1.9:	Possible modes of boiling (Nakayama et al., 1980b)	16
Figure 1.10:	Bubble formation and departure in one cycle for the flooded mode (Webb and Haider, 1992)	18
Figure 2.1	Schematic representation of the two-phase heat spreader	27

Figure 2.2:	Exploded view of the two-phase spreader plate prototype employed in the experimental runs	28
Figure 2.3	Schematic of the experimental set up for forced convection experiments	29
Figure 2.4	Detailed view of the heater assembly used in the forced convection experimental set-up	30
Figure 2.5	(a) 4.5 mm thick aluminum prototype used in the natural convection experiments. (b) Ceramic test package used for supplying the heat. 9 mm x 9mm porous copper structure with 310 μm channels attached to the thermal test die enhancing boiling heat transfer	30
Figure 2.6	Schematic of the thermal test die used in the natural convection experiments. Die heating is realized through two 38 Ω resistors in parallel	31
Figure 3.1:	Performance enhancement on using the microstructure when compared to the base study without the enhancement structure. Inclusion of the enhancement structure in the evaporator section resulted in better heat transfer performance of the two-phase spreader	37
Figure 3.2:	Performance evaluation of the thin two-phase spreader under natural-air cooled conditions	38
Figure 3.3:	Plot of the total resistance and the boiling resistance for the naturally air-cooled flat plate two-phase heat spreader. The onset of boiling in the system results in a sudden drop in the resistances	39
Figure 3.4:	Variation of heat spreader wall temperature with respect to the total heat dissipated for different airflow rates employed to cool the condenser. The performance of the two-phase spreader plate was found to be dependent on the external convection resistance.	41

Figure 3.5:	Boiling performance plot for two different microstructure base area sizes. The larger enhancement structure with more nucleation sites did not result in significant improvement in the heat transfer performance.	43
Figure 3.6:	(a) Shows a quarter geometry of the heat spreader used for modeling the temperature profile variation along the evaporator. (b) Temperature gradient as a result of spreading along the evaporator section causes the channels along the edges to remain inactive.	44
Figure 3.7:	Performance evaluation of the heat spreader for different fill ratios of FC-72. Fill ratios resulting in flooding of the evaporator section show similar heat transfer performance.	46
Figure 3.8:	Variation of h_{coeff} with q'' of PF5060 for different starting system pressures.	47
Figure 3.9:	Heat flux versus wall temperature of PF5060 for 34.1, 42.6 and 60.6 kPa. Decrease in system pressure results in lower wall temperature.	47
Figure 3.10:	Heat transfer coefficient as a function of wall superheat for a system pressure of 34.1 (kPa).	48
Figure 3.11:	Thermal performance for three different Fluorinert liquids with the starting system pressure almost equal to the saturation pressure at room temperature.	49
Figure 3.12:	Effect of varying stack height on boiling heat transfer of PF5060.	51
Figure 3.13:	Boundary conditions on the enhanced structure for numerical analysis.	52
Figure 3.14:	Comparison of conduction model predictions of stacked structures with experimental results obtained with PF5060.	53

Figure 3.15: Plot of two-phase spreader performance at various orientations. Slight deterioration in performance observed at high heat fluxes for 90° inclination.	54
Figure 3.16: Snapshots of steady state boiling from the enhancement structure in the evaporator section of the two-phase heat spreader at 90° inclination. Rapid evaporation at high heat fluxes result in partial dry out of the enhancement structure	55
Figure 4.1: Envisioned bubble formation and departure in the “flooded” mode regime	60
Figure 4.2: Geometry of vapor plug inside the tunnel used for computing Q_m'' and Q_f'' .	65
Figure 4.3: Comparison of experimental nucleation site density with those predicted using correlation in Eq. 4.37.	71
Figure 4.4: Schematic of the enhancement structures reported in literature used for validating the semi-analytical model. The geometric parameters of the structures are summarized in table 4.1.	74
Figure 4.5: Comparison of bubble departure diameter – prediction vs. experiments	75
Figure 4.6: Comparison of frequency – prediction vs. experiments	76
Figure 4.7: Comparison of prediction vs. experiments for Chien’s and Nakayama’s structures (a) heat flux (b) heat transfer coefficient	76
Figure 4.8: Comparison of heat flux variation with wall temperature for Ramaswamy’s structures of pore size (a) $D_p=150\ \mu\text{m}$ and (b) $D_p=200\ \mu\text{m}$.	78
Figure 4.9: Algorithm for the two-phase spreader thermal performance model based on the semi-analytical model for enhanced boiling.	78

Figure 4.10: Thermal performance predictions of the forced air-cooled two- phase heat spreader (a) Air velocity of 1 m/s (b) Air velocity of 2 m/s.	80
Figure 5.1: Velocity vectors obtained for a Re=400 lid-driven cavity flow on a 16 x 16 grid.	89
Figure 5.2: 2D cavity velocity profile comparison with Ghia et al. [1982] for Re = 400. (a) X component of velocity as a function of y through center. (b) Y component of velocity as a function of x through center.	89
Figure 5.3: Interface Γ enclosing Ω^c in a region Ω . Interface Γ is represented by zero level set.	90
Figure 5.4: Zoomed comparison of a notched disc (Zalesak's problem) that has been rotated one revolution about the center of the domain	93
Figure 5.5: Computational grid with boundary conditions	95
Figure 5.6: Envisioned bubble growth from a surface pore of an enhanced structure.	97
Figure 5.7: Bubble growth from a pore size of 120 μm for $\Delta T = 3$ K.	100
Figure 5.8: Flow patterns during bubble growth for $\Delta T = 5$ K and $D_p = 120$ μm at (a) $t = 0.016$ s and (b) $t = 0.032$ s.	101
Figure 5.9: Bubble shape from a 120 μm pore cavity at $t = 0.03$ s for different wall superheat values.	102
Figure 5.10: Plot of bubble diameter variation with time for growth from a 120 μm cavity at different wall superheats.	103

Figure 6.1: Schematic of possible computational domain for numerical simulation of bubble growth from enhanced surface.

108

NOMENCLATURE

C_{tg}	empirical constant for growth rate
C_h	Hamaker constant (J)
c_p	specific heat of liquid (J/kg-K)
D	diameter (m)
F	force (N)
f	frequency (Hz)
h_{fg}	latent heat of vaporization (J/kg)
k	thermal conductivity (W/m-K)
L	length of thin film region
Q''	heat flux (W/m ²)
m	mass (kg)
n_s	nucleation site density (m ⁻²)
Pr	Prandtl number
p	pressure (Pa)
R	instantaneous bubble radius
R_c	effective surface active cavity size
r_e	equilibrium bubble radius
r_t	tunnel radius
T_w	wall temperature (°C)
T_{sat}	saturation temperature (°C)
t	time (s)
ΔT_{sup}	wall superheat

V	volume (m ³)
u	velocity (m/s)
v	velocity (m/s)
x_m	mean length of liquid slug (m)

Greek Symbols

σ	surface tension (N/m)
θ	contact angle (degrees)
ρ	density
δ	film thickness (μm)
δ_o	initial film thickness (μm)

Subscript

B	bouyancy
b	bubble
bi	bubble inertia
ex	external
f	film
L	lift
l	liquid
m	menisci
max	maximum
min	minimum

mom momentum
ne non-evaporating
p pore
sat saturation
t tunnel
ug unsteady growth
v vapor

CHAPTER 1: INTRODUCTION

The evolution of the microprocessor has led to significant increase in the number of I/O pads, the number of high frequency interconnects, and power dissipation. The primary objective of thermal management is to ensure that the temperature of each component is maintained within the maximum allowable limit. Operation of components at temperatures higher than the allowable limit may result in irreversible changes in its operating characteristics or may even cause physical destruction of the component. Also, most failure mechanisms encountered in electronic components are kinetic in nature and depend exponentially on the device operating temperature. Thus, precise control of component operating temperatures is necessary to ensure product reliability.

One of the key challenges facing the design of future electronic systems is the growing size of thermal management hardware, in the face of shrinking system sizes. Taking computing products as an example, the thickness of portable computers has been reduced from around 40 mm in 1993 to less than 20 mm today, while the heat dissipation from the microprocessor chip has increased from around 2 W to 15 W in some designs. On the other hand, advanced workstation computers are built with an increasing number of chips in ever tighter three-dimensional space. The increase in performance of these workstations has reduced board-to-board spacing, and as a result, the available space for thermal design in a computer system. Current state-of-the-art for infrastructure equipment involves increasingly larger air-cooled heat sinks. Enormous pumping power will be needed if one resorts to forced convection air-cooling for large

systems of the future. While demonstrations of large thermal dissipation capabilities through various advanced cooling schemes have been made over the past decade, air-cooling has remained the mainstay in most electronic systems. It is clear that for a number of applications, direct air-cooling will have to be replaced with other high performance compact cooling techniques.

1.1 Motivation and Background

Microelectronic equipment at the extreme ends of the product spectrum, super computers at the high end and portable computers at the low end, face a common challenge in heat transfer engineering, namely removal of increasingly large amount of heat from thin spaced enclosures. Current technology for cooling electronic systems in thin space enclosures involves the use of solid metal plates to spread the heat. In order to illustrate the limitations of this methodology, it is instructive to study the effect of the spreader aspect ratio on the thermal resistance.

A thin plate shown in Figure 1.1 is used to study the heat transfer performance of solid heat spreaders. Figure 1.2 shows a plot of the variation in the thermal resistance (R) of the spreader with change in spreader thickness for different thermal conductivity of the spreader material. The thermal resistance was defined as:

$$R_{\text{thermal}} = (T_{\text{heater}} - T_{\text{wall}}) / Q \quad (1.1)$$

As it can be seen in Figure 1.2, the thermal resistance of the plate increases sharply with decrease in the plate thickness. Large reduction in overall thermal resistance can be achieved by increasing the thermal conductivity of the spreader plate.

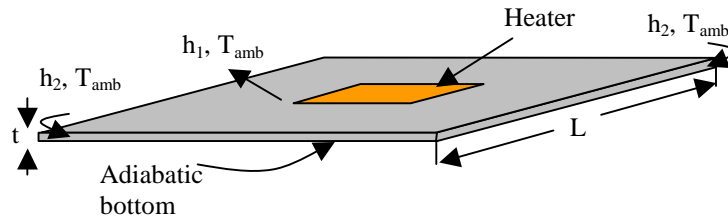


Figure 1.1. Geometric configuration of a model used to study solid heat spreader performance.

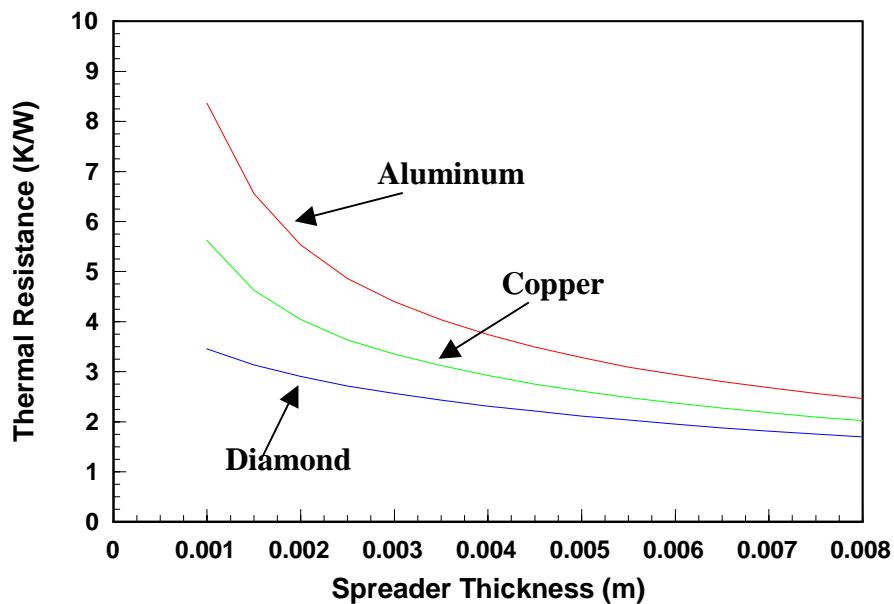


Figure 1.2. Variation in thermal resistance with respect to the spreader thickness. Higher thermal conductivity plates result in lower resistance values.

Advanced composite materials with high thermal conductivity and matching thermal expansion coefficient to that of silicon are progressively being used to replace aluminum (Saraswati and Polese [1999]) and copper (Sepulveda et al. [2000]) metal plate heat spreaders (Table 1.1). Recent attempts in improving the thermal performance of the spreader material have also focused on the development of silicon substrate with micro-whiskers perpendicular to the surface (Hammel et al. [1999]). Different forms of

carbon, such as processed natural graphite, carbon-carbon composites and diamond-like carbon offer lots of possibilities for maximizing conductive heat transfer due to their higher thermal conductivity. Natural diamond with high thermal conductivity (2000 W/mK) and matching thermal expansion coefficient (1-2 ppm/K) has been used in bonding devices such as laser diodes to dissipate the thermal load (Behr and Luy [1990], Eisele and Haddad [1995]). The advent of low-pressure synthesis of diamond, coupled with inexpensive large chemical vapor deposition process has made it possible to consider the use of diamond in electronics for heat removal (Fabis and Windischmann [2000]). However, continuous and defect free growth of diamond is a difficult task. The presence of defects such as amorphous carbon / carbide phases and voids reduces the thermal conductivity of the diamond films and hence its capacity to be an effective heat spreader (Jagannadham [1998]). High thermal conductivity materials like Aluminum Nitride (370 W/mK) can be used to fill the void like regions formed during the growth of diamond, thereby making the multilayer AlN / diamond composite structure an effective heat spreader (Yoganand et al. [2002]). Unfortunately, the contamination of wafers during deposition of diamond has prevented the integration of diamond heat spreaders with silicon technology.

The use of liquid-vapor phase change to transport heat across the system has been proposed as an alternative to the polycrystalline diamond or AlN ceramic heat spreaders, mainly due to the high cost of fabricating heat spreaders from these types of materials. Particular emphasis has been placed on the development of flat plate heat pipes for cooling electronic systems in space-constrained applications. Successful

demonstration of the use of flat heat pipes for cooling printed wiring boards (Basiulis et al. [1986]) with heat fluxes up to 2 W/cm^2 has been achieved in the past.

Table 1.1: Material properties of composites solids used instead of copper and aluminum metal plates

Material	Density (g/cm^3)	Thermal Conductivity (W/mK)	CTE ($\text{ppm}/^\circ\text{C}$)
Silicon	2.3	151	4.2
Aluminum	2.7	238	23.6
AlN	3.3	170-200	4.5
Beryllia	3.9	250	7.6
Copper	8.9	398	17.8
Cu W (10-20% Cu)	15.7-17.0	180-200	6.5-8.3
Cu Mo (15-20% Mo)	10.0	160-170	7.0-8.0

There has been considerable amount of research on micro heat pipe arrays and flat plate micro heat pipes (Peterson [1992], [1996]). Flat heat pipes with a segmented vapor space machined on a silicon substrate have been suggested as an alternative to the conductive cooling of integrated circuits using diamond films (Benson et al. [1996]) with the flat plate heat pipe exhibiting a thermal conductivity approximately five times that of the silicon material over a wide range of power densities. The design of wick structures in flat plate heat pipes has also become a focus of renewed interest. Experimental and theoretical analyses of heat transport capabilities of flat miniature heat pipes with trapezoidal and rectangular micro capillary grooves (Hopkins et al.

[1999]) and triangular microgrooves (Park et al. [2001]) have been carried out with the objective of increasing the fluid flow to the evaporator section. Heat pipe integrated with an aluminum plate has been utilized for CPU heat removal of 18W from notebook computers, while maintaining the CPU below 85 °C (Take and Webb [2001]).

Heat removal using flat plate and micro heat pipes is subject to several constraints (Cao et al. [1993], Ha and Peterson [1998]). The circulation rate of the working fluid is often limited by insufficient driving pressure. This so-called ‘capillary limit’ restricts the application of heat pipes to moderate chip heat dissipation rates and relatively small heat transport distances.

There exists a need for thermal management devices that have superior cooling performance than conventional heat pipes, while remaining compact and orientation independent. This motivation led to the design of a flat two-phase heat spreader plate. The orientation independence of the device is derived from the geometrical design of the enclosure that contains the liquid, while high heat removal capability is achieved through boiling. Ample supply of liquid to the evaporator, coupled with known boiling enhancement techniques help in overcoming the performance constraints of conventional heat pipes and thermosyphons.

Enhanced boiling surfaces have demonstrated higher heat fluxes and lower temperature overshoot prior to boiling initiation. Tubes with enhanced surfaces have been used in the refrigeration and chemical industries extensively to achieve the above objectives. It is well documented that re-entrant cavities have the characteristic ability to entrap vapors, thereby becoming active nucleation sites for boiling initiation (Nakayama et al. [1980a], Chien and Webb [1998a]). The efficient performance of

enhanced structures in pool boiling makes them good candidates for incorporation into the evaporator section of two-phase heat spreader to accommodate higher heat fluxes.

1.2 Literature Review

1.2.1 Review of enhanced surfaces in boiling

There are two fundamental issues addressed in almost all two-phase heat transfer studies – incipience overshoot and critical heat flux. Before boiling initiates, the primary mode of heat transfer is single-phase convection. The temperature of the heated surface has to be raised beyond the boiling point of the working fluid for boiling to occur. This excess temperature required to initiate boiling is called incipience overshoot. After initiation, the bubble generation spreads quickly over the entire surface and the temperature drops suddenly. This problem is magnified for low surface tension fluids (e.g. fluorocarbons). As the heat flux is raised further, the highly thermally efficient regime of nucleate boiling follows, culminating in a limit where the entire surface is covered with a thin vapor blanket and the heat transfer rates drop again. This is called the critical heat flux and is the maximum limit of heat dissipation achievable.

To reduce the incipience excursion and increase the critical heat flux (CHF), enhanced surfaces have been used in the past. Heat exchangers and process equipment use enhanced tubes that promote boiling/condensation and improve the performance significantly. These surfaces consist of interconnected tunnels and pores. These integral enhancement schemes promote boiling initiation while the increase in surface area contributes to the increase in CHF. Thome [1990] and Webb [1994] have surveyed

the various enhanced surfaces reported in the literature for heat exchangers in power and process applications. A list of some of the surfaces developed for electronic cooling and the typical heat fluxes dissipated, was compiled by Ramaswamy [1999] and is reproduced in Table 1.2. The geometrical details of some of the surfaces listed in this table are shown in Figure 1.3. Mudawar and Anderson [1993] and Nakayama et al. [1984] developed special three-dimensional enhanced structures that have demonstrated heat dissipations of over 100 W/cm^2 , with FC-72 as the working fluid. Moreover, no incipience excursion was observed with these structures. Hence, the use of enhanced structures in the evaporator can push the performance envelope of the two-phase spreaders beyond that of heat pipe limits thereby making it a viable solution for cooling electronic systems.

1.2.2 Review of flow visualization studies of boiling from enhanced surfaces

Despite the importance and the vast body of research on boiling from enhanced surfaces (Bergles [1999]), the fundamental physical mechanisms involved are far from being understood. Visualization studies have been carried out in the past to ascertain nucleate boiling mechanism from structured surfaces (Cornwell et al. [1976], Nakayama et al. [1980a], Arshad and Thome [1983], Chien and Webb [1998b], and Ghiu et al. [2001]).

Table 1.2: Boiling performance of enhanced surfaces in fluorinerts (Ramaswamy, 1999)

Enhanced surface	Geometrical details	Heat flux and operational constraint	Investigators
Gewa-T	Circular cross-section channels, with the lip dimension smaller than the diameter of the channel	~ 19 W/cm ² at a superheat of ~14°C with FC-72	Marto and Lepere (1982)
Thermoexcel-E	Covered channels of square or rectangular cross section, with pores at regular intervals on the cover.	~ 12 W/cm ² at a superheat of ~20°C with FC-72	Marto and Lepere (1982)
Microstud surface	Square pin fins of 0.305 mm side and 0.508 mm height at intervals of 0.610 mm on a flat surface	30 W/cm ² at a superheat of 30°C with FC-72	Anderson and Mudawar (1989)
9-pin surface	Nine pin fins of 3.63 mm diameter spaced 0.6 mm apart in a 3x3 array.	70 W/cm ² at a superheat of 30°C with FC-87	Mudawar and Anderson (1993)
Microstud enhanced stud	multiple level enhancement - consists of rectangular studs of 0.305 x 0.389 mm cross-section and 0.508 mm high on the surface of circular pin fins of 3.63 mm diameter.	105 W/cm ² at a surface temperature of 85 °C with FC-72 (subcooling of 35 °C)	Mudawar and Anderson (1993)
Tunnel heat sink	0.8 mm diameter vertical holes in a 1mm thick copper block	90 W/cm ² at a superheat of 30°C with FC-86	Oktay (1982)
Dendritic heat sink	porous surface 1mm high consisting of random pores of 50-500 μm size.	50 W/cm ² at a superheat of 25°C with FC-86	Oktay (1982)
Microporous stud	rectangular channels, 0.25 mm wide and 0.55 high on both sides of a 1 mm thick copper block. The channels on one side are at 90o to the channels on the other.	100 W/cm ² at a superheat of 27.8°C with FC-72	Nakayama et al. (1984)

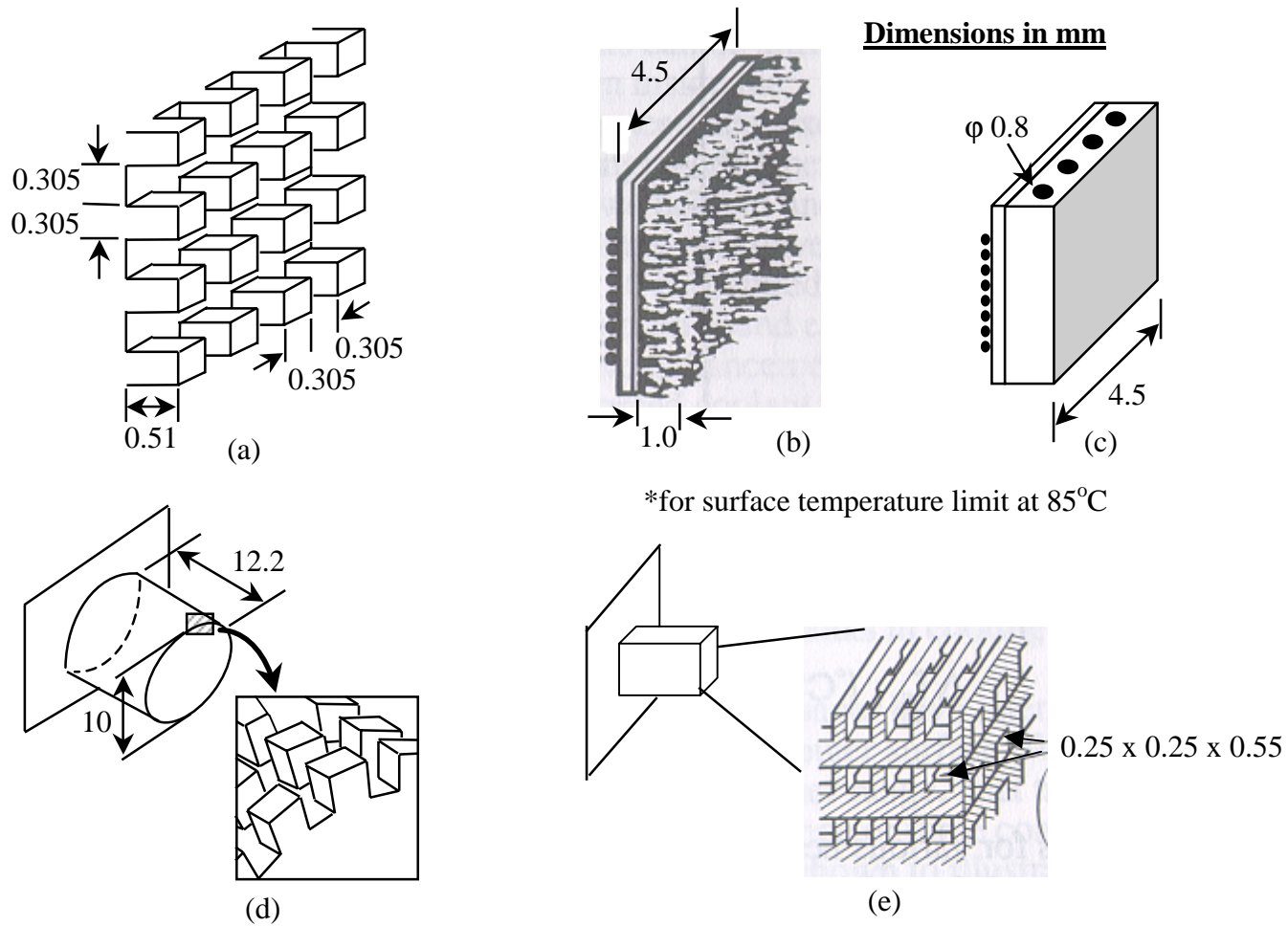


Figure 1.3: Enhanced structures for electronics cooling - (a) Anderson and Mudawar (1989), (b) and (c) Oktay (1992), (d) Mudawar and Anderson (1993), (e) Nakayama et al. (1984).

1.2.2.1 Nakayama et. al. visualization study

Nakayama et al. (1980a) were the first to perform a visualization study on the boiling nucleation process in a rectangular tunnel with pores on top. Their boiling apparatus consisted of a base block, two glass slide plates, end plates, and a 0.05 mm thick metal lid with a series of pores drilled in the center as shown in Figure 1.4. These parts formed a rectangular cross-section tunnel connected to a liquid pool of R-11 by the pores in the cover plate. Heat was provided either from a cartridge heater in the base block or through an electrically heated lid. A high-speed cine film camera recorded boiling activation. From their visual observations, they concluded the existence of an advancing liquid-vapor interface inside the tunnels (Fig. 1.5).

1.2.2.2 Arshad and Thome visualization study

Arshad and Thome (1983) carried out a visualization study of the boiling mechanism inside the tunnel with water using an experimental apparatus similar to the one used by Nakayama et al. They soldered micro-drilled cover plates to the grooved regions to form the test surfaces. Their apparatus was designed to make observations along the axis of the tunnel, and to view the nucleation process in the corners. Triangular, rectangular and circular cross-sections were tested. The ends of the tunnel were closed with thin glass plates to allow for observations. They observed in the experiments that nucleation always occurred at the corners of the grooved surface. Once the vapor reached the pore in the cover plate, a bubble immediately grew in the liquid pool at this pore. Figure 1.6 shows the schematic sketch of the activation of a

triangular groove with pore diameters of 0.15 mm and a groove height of about 1 mm. Activation of circular tunnels was found to be more difficult than the other geometries.

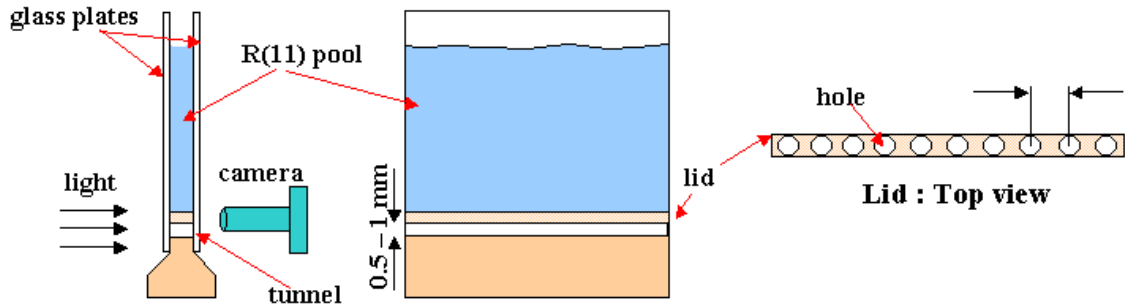


Figure 1.4: Nakayama et al. (1980a) visualization apparatus.

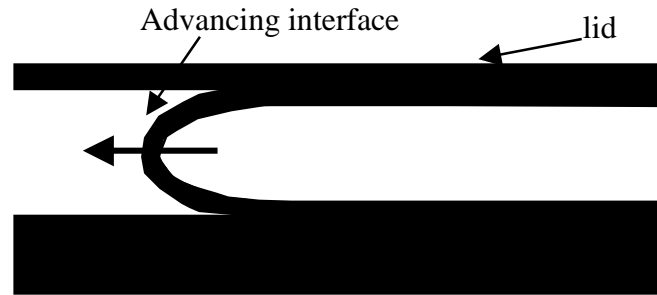


Figure 1.5: Liquid-vapor interface in the tunnel, Nakayama et al. (1980a).

1.2.2.3 Chien and Webb visualization study

Chien and Webb (1998b) conducted experiments to visualize nucleate boiling on an enhanced tubular surface having sub-surface tunnels and surface pores (Fig. 1.7). A thin foil sheet having 0.23 mm pore diameter at 1.5 mm pore pitch covered the fins and allowed for direct observation of the boiling process in the sub-surface tunnels. The experiments were conducted for saturated and sub-cooled boiling in the horizontal and

vertical orientations. Their experiments showed that a large part of the sub-surface tunnels was vapor filled except for liquid menisci in the corners, and the remaining part of the region had oscillating menisci.

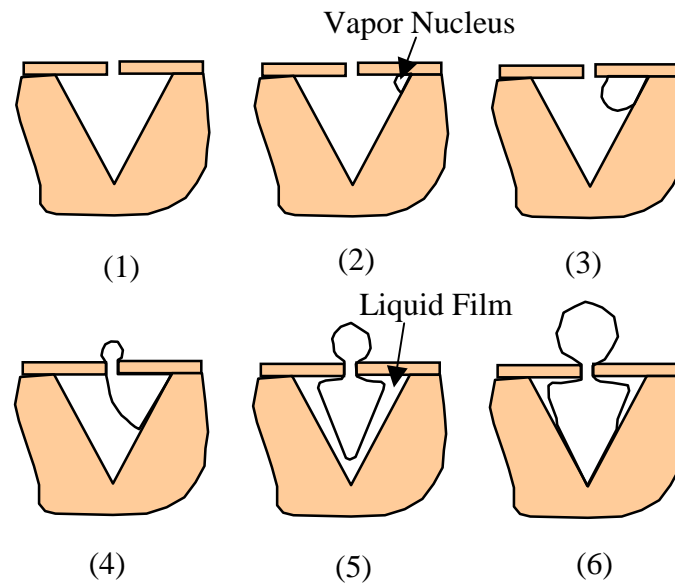


Figure 1.6: Arshad and Thome's (1983) conceptual sketches of the boiling phenomena in triangular tunnel.

1.2.2.4 Ghiu et al. visualization study

Ghiu et al. [2001] carried out visualization study of pool boiling from transparent enhanced structures (Fig. 1.8) using a high speed 1000 frames/s camera. They studied the effect of channel width and pore pitch on the boiling performance and came up with three boiling regimes, namely the “slug formation”, the “slug migration” and the “slug predominance”. Their experiments with PF5060 showed similar advancing liquid-vapor interface as noticed by Nakayama et al. [1980a].

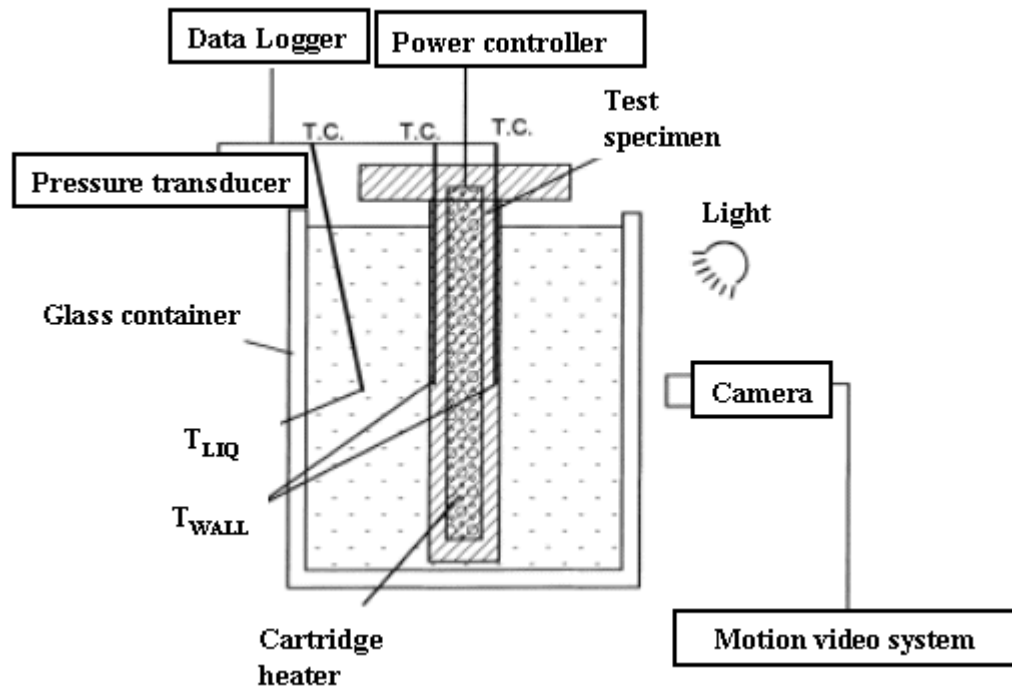


Figure 1.7: Schematic of Chien and Webb's (1998b) visualization experiments.

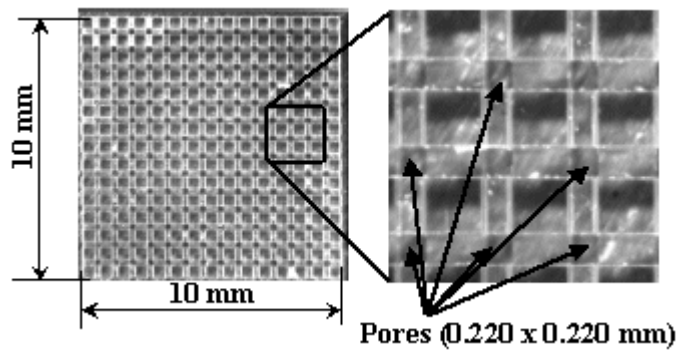


Figure 1.8: Transparent quartz enhancement structures used in Ghiu et al. (2001) visualization studies.

1.2.3 Analytical models for boiling from structured surfaces

There is sufficient evidence in literature that structured surfaces result in high heat transfer rates with very small rise in the surface temperature. A few investigators have developed semi-empirical mathematical models to capture the boiling mechanism from these surfaces and validate the enhancement observed.

1.2.3.1 Nakayama's suction-evaporation model

Nakayama et al. (1980b) were the first to propose a mechanistically based analytical model to predict boiling performance of structured enhanced surfaces. They envisioned three boiling regimes, namely the “flooded”, “suction-evaporation”, and “dried-up” modes (Fig. 1.9). In the flooded mode, the tunnel is occupied by alternating regions of liquid and vapor slugs. The suction-evaporation mode results in vapor filled tunnels except for a thin layer of liquid held along the edges. In the dried-up mode, the tunnel is completely devoid of liquid and the boiling is similar to that on a plain surface.

Nakayama et al.’s dynamic model is based on the sequence of events happening inside and outside the channels of a boiling enhancement structure during one complete cycle of bubble growth and evaporation. They divided once bubble cycle into a) Phase I: the pressure build-up phase, b) Phase II: pressure-reduction phase and c) Phase III: liquid intake phase. The authors developed detailed mathematical expressions for the heat transfer in Phase I and Phase II and also the bubble dynamics in the Phase II. The inputs required for the model are the geometry of the structure, the liquid properties and wall superheat. The model has six empirical constants in all to account for heat transfer

inside the tunnels, bubble departure, recession of liquid meniscus at the inactive pores, pressure drop across the pore and heat transfer at the external surfaces.

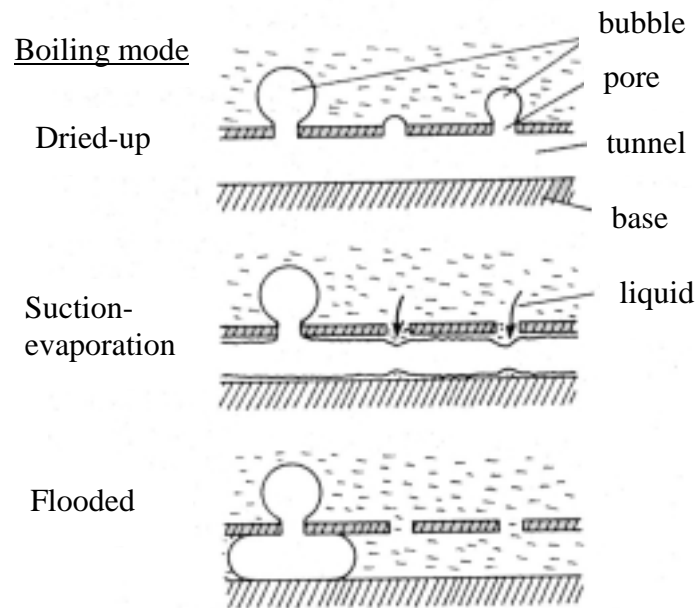


Figure 1.9: Possible modes of boiling (Nakayama et al., 1980b).

1.2.3.2 Webb and Haider model

Webb and Haider [1992] developed an analytical model for predicting the bubble dynamics and heat transfer in the flooded mode. The model was developed for a tunnel of circular cross-section for simplicity. The authors hypothesized the tunnel to be filled with vapor near the active pores and surrounded by liquid slugs. Liquid evaporates at all the liquid-vapor interfaces and the spatial variation in the thickness of this interface was taken into account. A complete bubble cycle from formation to departure is shown in Figure 1.10. Expressions were developed to predict the heat transfer inside the tunnels and at the external surfaces. The model also calculates the

frequency of bubble growth and the nucleation site density. The expression for bubble departure diameter is similar to that used by Nakayama et al. [1980b] and consists of one empirical constant.

A novel feature of their model was the prediction of the heat flux due to external convection. Haider and Webb [1997] developed a sub-model for external convection based on the model of Mikic and Rohsenow [1969] for boiling from a plain surface. The authors included a transient term to account for the convection in the wake of the departing bubble. The model assumes that the beginning of the bubble cycle is dominated by transient conduction, and the final part is dominated by micro-convection caused by the wake of the departing bubble. The model was used to predict the heat transfer for the Nakayama et al. [1980a] structure. The predictions were within $\pm 40\%$ of the experimental results. The authors also applied the model for Chien's [1996] structure and the predictions were within $\pm 30\%$.

1.2.3.3 Chien and Webb's suction-evaporation model

Chien and Webb [1998c] developed an analytical model by assuming that liquid evaporation inside tunnels results in the formation of bubbles. The initial meniscus radius was assumed to be uniform along the length of the tunnel and was computed through a correlation that accounted for the fin and pore geometry, wall superheat, liquid surface tension and viscosity. The evaporation inside the tunnels was computed by calculating the thickness of the meniscus at discrete time steps. The expression for the external heat flux was same as that developed by Haider and Webb [1997].

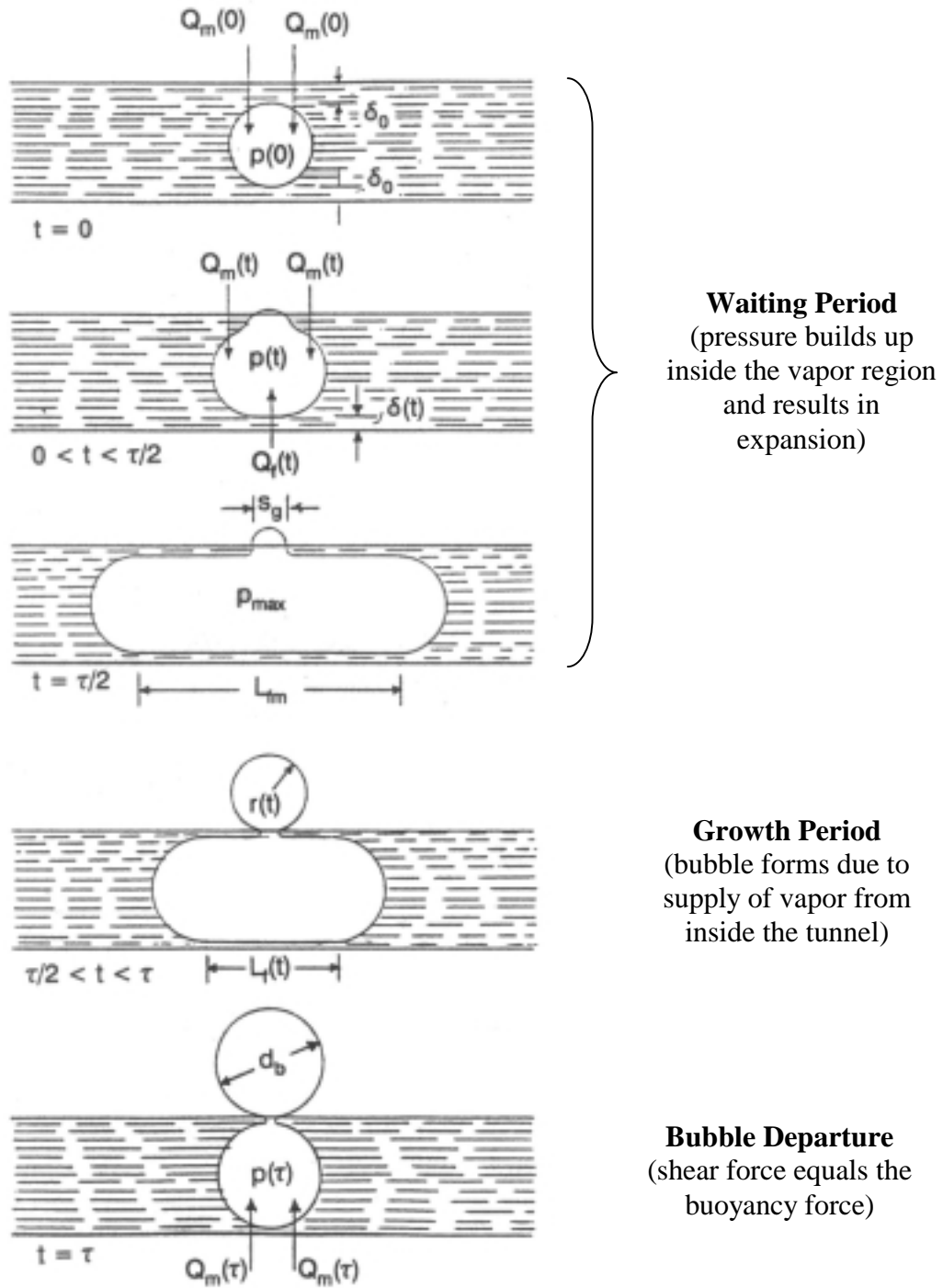


Figure 1.10: Bubble formation and departure in one cycle for the flooded mode (Webb and Haider, 1992).

The authors compared the predictive quality of the model with their boiling visualization results. The heat fluxes were predicted within $\pm 33\%$, bubble departure diameter within $\pm 20\%$ and frequency within $\pm 30\%$.

1.2.3.4 Ramaswamy et al. semi-analytical model

Ramaswamy et al. [2003] modified Chien and Webb's [1998c] suction-evaporation model for boiling from enhancement structures. The enhanced structures used in their studies were similar to the ones used by Nakayama et al. [1980a] and consisted of an array of rectangular channels cut in a pattern resulting in a highly porous block. Besides incorporating the effect of dynamic forces in the prediction of the bubble departure diameter, the tunnel heat transfer calculation was also modified to include the local variation of the liquid saturation temperature due to variation in the meniscus thickness.

The model predicts the bubble departure diameter within $\pm 10\%$. The frequency and nucleation site densities were predicted within $\pm 40\%$. The heat fluxes predicted within $\pm 50\%$ with the maximum error observed at lower wall superheats.

1.2.4 Numerical simulation of two-phase flows

Recently, computational methods have been developed to provide solutions for fluid flow problems with moving interfaces separating gas and liquid phases. Numerical approaches for solving free surface problems in the context of incompressible flows can be broadly classified as "front-tracking" and "front-

capturing”. In front tracking schemes, the algorithms place marker particles along the front and advance the positions of the particles in accordance with a set of finite difference approximations to the equations of motion. Such schemes usually go unstable and blow up as the curvature builds around a cusp, since small errors in the position produce large errors in the determination of the curvature.

Juric and Tryggvason [1998] used front tracking formulation for computations of boiling flows. The equations were discretized by a finite difference method on a regular grid and the phase boundary was explicitly tracked by a moving front. They applied this numerical method to film boiling, where vapor bubbles were generated from a thin film next to a hot wall. The authors found the resulting heat transfer rates and wall temperatures to be in good agreement with experimental observations.

Volume tracking methods fall under the classifications of front tracking schemes. In this method, fluid volumes are initialized in each computational cell from a specified geometry. Exact interface information is then discarded in favor of the discrete volume data. The volume data is traditionally retained as volume fractions, whereby mixed cells will have a volume fraction between zero and one and cells without interfaces will have a volume fraction equal to zero or unity. Interfaces are tracked in volume of fluid method by evolving fluid volumes forward in time with solutions of an advection equation. Interface geometry is inferred based on the local volume data before interfaces can be reconstructed. The reconstructed interface is then used to compute the volume fluxes necessary to integrate the volume evolution equations.

Welch and Wilson [2000] presented a method towards the simulation of flows with mass transfer due to changes of phase using volume of fluid based interface tracking method. The bulk fluid was assumed to be viscous, conducting and incompressible. This numerical method was tested on a one-dimensional problem and then used in simulations of horizontal film boiling.

1.2.4.1 Level set method

Osher and Sethian [1988] introduced a “Hamilton-Jacobi” level set formulation of the equations of motion for propagating interfaces. This formulation allows fronts to self intersect, develop singularities and change topologies. The numerical algorithm based on this approach handles topological merging and breaking naturally and does not require a functional representation of the moving front. The moving front is embedded as a particular level set in a fixed domain partial differential equation. This method tracks the motion of an interface by embedding the interface as the zero level set of the signed distance function and the motion of the interface is matched with the zero level set of the level set function,

Son and Dhir [1998] adopted a level set approach to simulate film boiling on a horizontal surface. The numerical algorithm developed by Sussman et al. [1994] for incompressible two-phase flow was modified to include the effect of liquid-vapor phase change. The modified level set method was applied to understand the mechanism of bubble release pattern with an increase in heat flux or wall superheat. They were able to show bubble release patterns from their numerical simulations to be consistent with visual observations reported in the literature and also reported the Nusselt numbers from

the analysis to be bounded by those from existing correlations. Son et al. [1999] captured the evolution of a vapor bubble at a nucleation site by dividing the computational domain into micro and macro regions. The macro-region consisted of the evolving vapor bubble and the liquid surrounding the bubble while the micro-region captured the thin liquid film that forms underneath the bubble. The film thickness at the outer edge of the micro-layer and its spatial derivative were matched with those obtained from the macro solution. The authors were able to show good agreement between experiments and numerical predictions for bubble growth history, shape of the bubble diameter and bubble diameter at departure. Level set formulation has also been employed (Son et al., [2002]) to study bubble merger normal to and along the heater surface as would occur in fully developed nucleate boiling.

1.3 Overview of the Current Study

The increase in heat fluxes at the chip level, combined with the reduction in system sizes has motivated the development of more efficient thermal management techniques for electronics. The above motivation led to the design of a flat two-phase heat spreader plate. The performance constraints of conventional heat pipes can be overcome in the two-phase spreader plate through ample supply of liquid to the evaporator, coupled with known boiling enhancement techniques and design constraints for orientation independent functioning. The current work studied the thermal performance of the novel two-phase spreader plates while addressing some of the issues involved in the practical implementation of the spreader design.

Although the enhancement in boiling performance with porous surfaces has been well documented, there is considerable lack of understanding of the boiling mechanism, and of knowledge to predict the effect of the geometric parameters and fluid properties on the performance. Analytical models help understand the mechanism of boiling and can be used as a sizing tool in practical applications. The existing models on boiling from enhancement surfaces focus on the “suction-evaporation” mode, though visualization studies clearly show the existence of liquid-vapor slugs in the channels. One of the objectives of this study was to develop a semi-analytical model that builds upon the previous investigations while accurately capturing the physics involved in enhancement boiling. Also, the recent advance in the modeling of two-phase flows was used in developing a simplified numerical method for understanding the boiling mechanism from structured surfaces.

CHAPTER 2: EXPERIMENTAL SETUP AND PROCEDURES

Temperature measurement experiments were carried out on the two-phase spreader prototypes to characterize the performance of the spreader plates. Two different prototypes of varying dimensions were developed and tested under different condenser conditions. Table 2.1 briefly summarizes the test results carried out with the two-phase spreader prototypes and compares the results obtained from the experiments with the performance of a solid metal plate subjected to similar boundary conditions.

Table 2.1 Comparison of two-phase spreader plate performance with that of a solid spreader plate for different condenser conditions

No.	Material	Length (mm)	Width (mm)	Height (mm)	Condenser Conditions	Heat Flux (W/cm ²)	Temperature (°C)	
							Thermosyphon	Solid Spreader
1	Copper	115.0	115.0	9.0	Forced air-cooled 1 m/s	42.5	76.2	107.0
2	Aluminum	86.5	86.5	4.5	Natural convection	6.3	73.4	105.0

Figure 2.1 shows a schematic representation, while Figure 2.2 shows an exploded view of the flat plate heat spreader used in the experiments. The two-phase spreader has an evaporator area in the middle and a hollow frame, called a 'pool belt', along its periphery. The spreader plate design consists of two plates and a hermetically sealed enclosure was achieved through O-ring and screws. The design included straight rectangular fins, cut out along the sides of the plate, for heat rejection to the ambient air. The gap between the fins was derived based on optimum plate spacing for maximizing natural convection heat transfer from an array of thermal plates.

The boiling enhancement microstructure used in this study is similar to the one used by Nakayama et al. [1984] in their pool boiling experiments. The optimum pore diameter and pitch of the enhancement micro channels is dependant on the heat flux (Chien and Webb, [1998a]). Ramaswamy [1999] investigated the effect of channel width in the range 90 μm – 320 μm on the heat transfer performance of two-phase thermosyphons using FC-72 as the working liquid. The studies showed an increase in heat dissipation with increase in pore size. Also, an increase in thermal performance was observed with decrease in pore pitch. These previous studies have established heat dissipation as a function of pore diameter and pore pitch, with the optimum value for the geometric parameters varying for different ranges of heat inputs.

In the current study, the geometric parameters of the enhancement structure were based on existing studies. The pore diameter and pitch were mainly chosen so as to avoid dry-out of the tunnels at low heat fluxes and do not necessarily represent an optimum value for the range of heat fluxes considered. The structure was made from a single layer of copper plate (~1mm thick). The copper layer has rectangular channels (0.31 mm wide, 0.55 mm deep) cut on either side of the plate with a 0.71 mm wall thickness between the channels. The channels intersect to form square pores of 0.31 mm size, with the pores acting as sites for bubble nucleation.

The orientation independent performance of the heat spreader is achieved by ensuring that the evaporator section of the spreader plate remains flooded under all inclinations through satisfying the design constraint

$$H_B/H_E = 2(1 + L_B/L_E) \quad (2.1)$$

The above constraint is derived by equating the minimum volume of coolant fluid required to completely fill the evaporator in the horizontal and the vertical orientations. Equation (2.1) defines the relationship between the dimensions of the evaporator and the pool belt and is derived assuming perfect separation of liquid and vapor phases. Such a situation is realized only in the cold state, that is, when the power is not supplied to the heat source. With initiation and maintenance of boiling, the level of two-phase mixture expands above the original liquid level in the cold state. It is possible to prove that the above equation also holds for the hot state, that is, when the two-phase mixture fills the evaporator section.

Denoting the volumetric fraction of the liquid phase in the evaporator as γ_E , and that in the pool belt as γ_B , the total liquid volume in the horizontal orientation is given as

$$V_{l,h} = \gamma_E H_E L_E^2 + 2\gamma_B (H_B + H_E)(L_B + L_E) L_B \quad (2.2)$$

Assuming the same volumetric fractions γ_E and γ_B for the vertical orientation, the total liquid volume is given by

$$V_{l,v} = \gamma_E H_E L_E^2 + \gamma_B H_B L_B (3L_E + 2L_B) \quad (2.3)$$

Equating $V_{l,h}$ and $V_{l,v}$ results in the design equation being reduced to the initial condition represented in equation (2.1). Design constraints similar to one described above can be derived for other planar configurations.

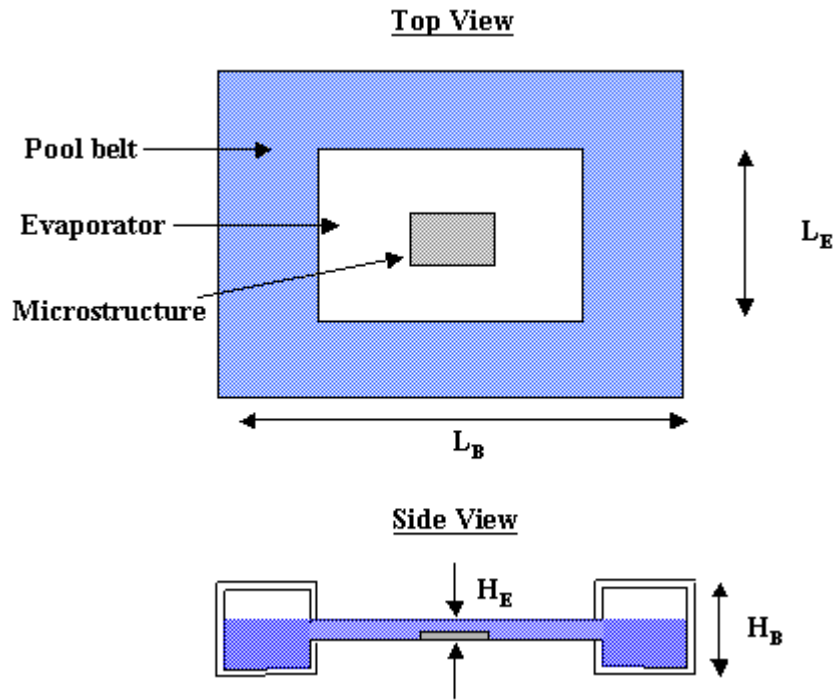


Figure 2.1: Schematic representation of the two-phase heat spreader.

2.1 Experimental Set-Up

2.1.1 Copper prototype: Forced convection

Figure 2.3 shows a schematic of the test facility used in the forced air-cooled experimentation. The forced air-cooled condition was achieved by placing the spreader plate prototype in a low speed wind tunnel. The micro-fabricated copper structure, used for enhancing boiling heat transfer, is attached at the center of the evaporator section using high thermal conductivity (38 W/mK) indium-lead solder. The heater assembly is shown in Figure 2.4. An Omega cartridge heater embedded into a square copper rod (1 cm x 1 cm) provided the heat input. The copper rod was insulated along the periphery

with styrofoam. Four copper-constantan sheathed thermocouples were embedded at the center of the copper rod starting from 4 mm below the boiling surface at intervals of 4 mm. The temperature readings from the thermocouples were employed in calculating the surface temperature at the base of the enhanced structure using a one-dimensional conduction analysis. The spreading resistance was accounted through the equation proposed by Mikic ((Bar-Cohen & Kraus [1993]) for a circular contact on a finite conducting medium. All thermal performance data reported in this work are based on power measurements estimated from the embedded thermocouple data.

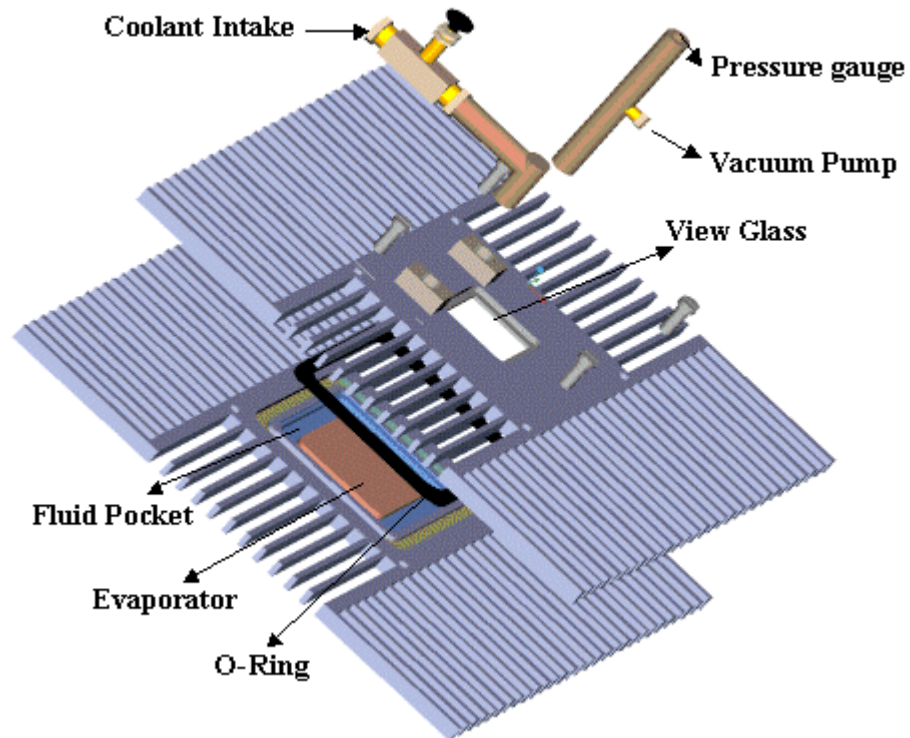


Figure 2.2: Exploded view of the two-phase spreader plate prototype employed in the experimental runs.

2.1.2 Aluminum prototype: Natural convection

A 14mm x 14mm thermal test package from NSA (FAUXWORKS die on a IPGA421K pin grid array package) was employed to simulate the die-heating conditions. The die consists of two heaters in parallel and the temperature measurement of the die was achieved with the help of thermistors. The thermistors were calibrated in an oven to obtain the temperature-resistance relation. As seen in figure 2.5b, the boiling enhancement structure is attached to the thermal test die with the help of a 500 μm thick thermal conductive adhesive with carbon fibers (ATTA SP-1). In contrast to the experiments carried out with forced convection cooling, direct cooling of the thermal test die was achieved by cutting a square hole at the base of the evaporator section of the heat spreader plate. The test package was enclosed in a plexi-glass casing and attached to the bottom of the two-phase spreader plate with the help of O-ring and screws. The underside of the package was covered with styrofoam to reduce the heat loss from the bottom of the package.

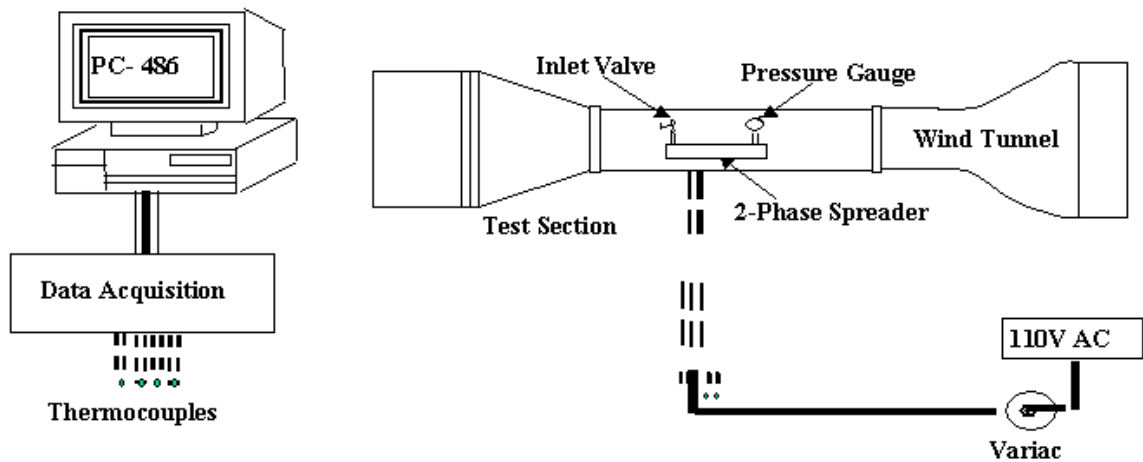


Figure 2.3: Schematic of experimental set up for forced convection experiments.

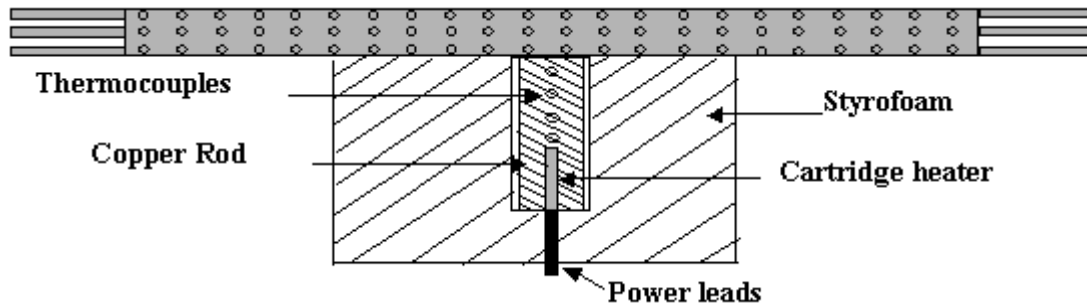


Figure 2.4: Detailed view of the heater assembly used in the forced convection experimental set-up.

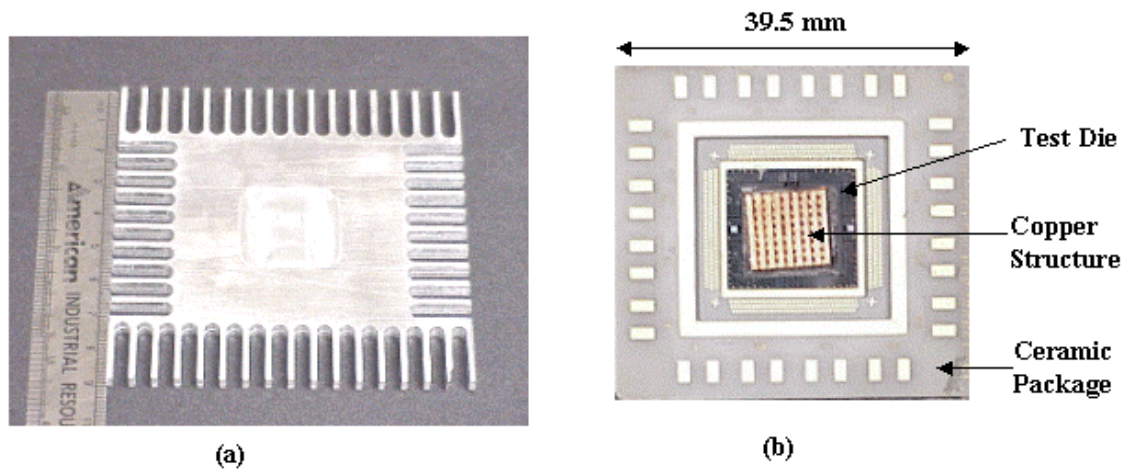


Figure 2.5: (a) 4.5 mm thick aluminum prototype used in the natural convection experiments. (b) Ceramic test package used for supplying the heat. 9 mm x 9mm porous copper structure with 310 μ m channels attached to the thermal test die enhancing boiling heat transfer.

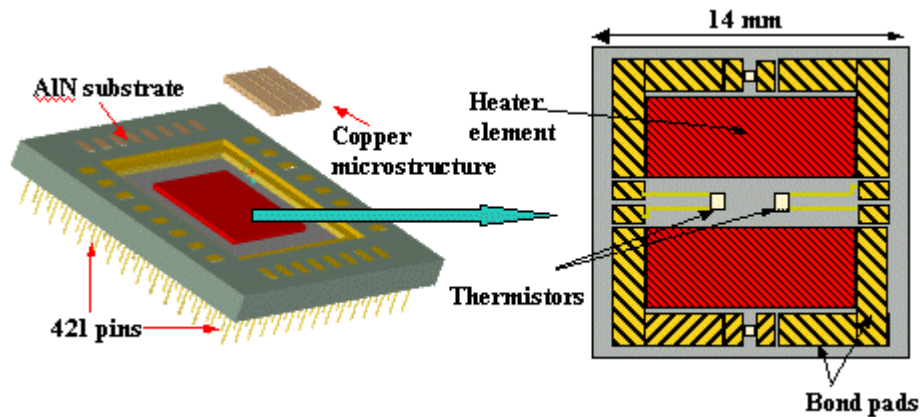


Figure 2.6: Schematic of the thermal test die used in the natural convection experiments. Die heating is realized through two 38Ω resistors in parallel.

2.2 Data Acquisition

Data acquisition consisted of temperature and voltage measurements. Transient and steady state temperature measurements were carried out using a computerized data acquisition system. The system consisted of a National Instruments SCXI-1000 chassis that could house up to four individual data acquisition cards. The thermocouple signals were fed into one such card (SCXI-1100), which was a 32-channel multiplexer/amplifier. A multifunction, analog, digital and timing I/O module (SCXI-1200) controlled this card. This module converted the multiplexed analog signal from the SCXI-1100 module to digital signal and fed it to a Pentium 200 MHz PC parallel port. A terminal block with an isothermal plate was used to interface the thermocouple ends to the input pins of the SCXI-1100 module. The isothermal block has a cold junction sensor, which acts as a reference temperature for the thermocouple signals. The isothermal block minimizes temperature gradients within the terminal connections and thus minimizes addition of extraneous voltages into the thermocouple signals.

The input voltage to the cartridge heater and the thermal test die was measured using a Fluke 87 True RMS multimeter. A precision resistor ($1\Omega \pm 0.01\Omega$) was connected in series to the heater / die to measure the line current. The voltage across the precision resistor was measured with the same multimeter.

2.3 Experimental Procedure

Before each run, the set-up was tested for leakage. Two different leakage tests were performed: (i) the system was immersed in a water bath and was observed for the emergence of any air bubbles, and (ii) the system was evacuated to 20 kPa (101 kPa = 1 atm) and allowed to stand still for approximately four hours to check if it held vacuum successfully.

The thermocouple measurements were acquired using a data acquisition system interfaced to a personal computer and controlled using LabVIEW software. A dial type pressure gauge was attached to the thermosyphon set-up to monitor the system pressure during an experimental run. During the initial start up of the system, a valve allowed a high vacuum pump to reduce the internal pressure down to low values (42 kPa). FC-72 was boiled separately in a conical flask at 100 ° C for 30 minutes to degas the liquid. The above procedure for degassing the liquid was repeated before all experimental runs. The system was subsequently filled with the liquid using flexible per-fluro-alkoxy tubing. During the filling process, at all times a standing amount of liquid was left in the tubing to prevent entry of air into the system. Once the system was filled to the required height, the vacuum pump was again used to degas the internal volume. Any discrepancy between the thermocouple measurement of the condenser wall temperature

and that predicted from the measured equilibrium pressure of the system indicated the presence of non-condensable gases. Saturation temperature for FC-72 at a given system pressure was calculated using a fourth order polynomial curve fit to the data presented in You [1990].

The actual runs were carried out in incremental power steps. All experiments were stopped when the evaporator / die temperature reached a maximum of 85 °C. After each power setting change, sufficient time was allowed for attaining steady state conditions. A deviation of less than 0.5 °C in the average temperature of the thermocouple readings attached to the top side of the thermosyphon plate in a span of 5 minutes was required to satisfy the criterion for steady state behavior. Having achieved steady state, 10 samples were taken during a subsequent 50-second period. The averaged values were used for computing the temperature gradients and subsequently the heat input to the two-phase spreader plate.

2.4 Uncertainty Analysis

The thermocouples and the data acquisition system were calibrated against a precision mercury thermometer at ice point to an uncertainty of 0.1 °C. The precision resistor used to measure the line current was accurate to $\pm 1\%$. The power dissipation from the cartridge heater / thermal test die was then computed using the current flow and the measured voltage drop across the chip. The voltage measurement uncertainty was specified by the instrument manufacturer as $\pm 0.7\%$ of the reading. Uncertainty measurements for heat flux and temperature measurement were made using the Kline and McClintok [1953] technique.

In case of the forced convection experiments, the uncertainty analysis included the uncertainties due to resolution of instruments and placement of the thermocouples. The temperature readings of the four thermocouples attached to the heater were linear. The R-squared value, a measure of the linearity of the data, was around 0.98 for all power input levels. As a result of the linear curve fit of the temperature data, from the in-line thermocouples, the uncertainty in the heat flux was $\pm 13.6\%$ at low heat fluxes. The uncertainty reduced to $\pm 5.7\%$ at high heat fluxes.

For the natural convection experiments, the heat flux was based on the 2 cm^2 surface area of the chip. At every power level, the resistances of the two thermistors were also measured. The chip surface temperature was calculated as an average of the two-thermistor temperatures. The maximum difference in the recorded temperatures of the thermistors was $0.12 \text{ }^\circ\text{C}$ before incipience and $1.24 \text{ }^\circ\text{C}$ during fully developed nucleate boiling. The uncertainty estimates included uncertainties due to measurement resolution, and calibration errors. The estimated error in the electrical heat input was $\pm 1.72\%$. The maximum uncertainty in the wall temperature based on the thermistor measurements was found to be $\pm 2.76\%$

Repeatability tests were conducted to confirm the reliability of the experimental data. For each test, at least three different runs were conducted on different days to verify the repeatability. All the test runs reported are found to be repeatable within 1.7% with respect to the temperature at the base of the enhancement structure.

CHAPTER 3: TWO-PHASE HEAT SPREADER THERMAL PERFORMANCE

The purpose of this study was to evaluate the thermal performance of the two-phase spreader prototype as a function of the operating parameters. The heat transfer performance of the spreader plate was evaluated for various condenser cooled conditions and different footprint sizes of the microstructure used for enhancing boiling heat transfer. Another aspect of the design of spreader plate that has practical significance is the liquid fill volume. Performance of the two-phase spreader with varying liquid fill ratios was investigated. Parametric studies were also carried out for enhancing the performance of the two-phase heat spreader plate. Experiments were performed to compare the performance of various working fluids. Data on the performance of the spreader plate for different coolant liquids at reduced pressures are reported along with the enhancement in heat transfer through the use of stacked multi-layer porous structures. The measured quantities were temperature, voltages and pressure and the uncertainties associated with these quantities have been presented in Chapter 2.

3.1 Baseline Study

Figure 3.1 compares the performance with and without a 15mm x 15mm x 1mm enhancement structure in the copper two-phase heat spreader for two different air speeds. The baseline study carried out at an air speed of 1m/s and a nominal power dissipation of 42.5 W/cm^2 , resulted in a maximum temperature of $86 \text{ }^\circ\text{C}$ at the wall where the enhancement structure was to be attached. Attaching the enhancement structure resulted in a $9.8 \text{ }^\circ\text{C}$ drop in temperature.

The total heat transfer from a structured surface is made up of two essential components – tunnel heat flux and sensible heat flux. The tunnel heat transfer is caused by thin film evaporation inside the micro-channels of the enhancement surface, while the external convection induced by bubble agitation accounts for the sensible heat flux. At low power levels, the channels in the enhancement structure are flooded with intermittent regions of liquid. As a result, the temperature at the evaporator is just slightly lower in the presence of the enhanced structure as the contribution from the tunnel heat transfer is considerably reduced. At low heat fluxes, the enhanced structure is similar to a porous block with larger surface area available for heat transfer to the liquid, which for these conditions is by natural convection. At higher heat fluxes, a large portion of the sub-surface channels are filled with vapor. The increase in tunnel heat transfer results in a higher frequency of bubbles being generated from the enhancement structure. The agitation caused by bubble departure along with an increase in the vaporization of liquid near the outer surface of the enhancement structure result in an increase in the sensible heat flux. As a result, the performance of the heat spreader is enhanced once boiling becomes a fundamental mode of heat transfer from the system.

Figure 3.2 plots the performance of the aluminum two-phase spreader plate at different power levels of the test die under naturally air-cooled conditions. A simple comparison of the spreader plate performance to that of a flat aluminum plate, subjected to the same condenser conditions, was achieved with the help of a conduction model. Natural convection correlations from Incropera and Dewitt [1990] were used to specify the heat transfer coefficients on the upward facing surface of the aluminum plate and

along the fin surfaces at the plate edges. The heat source condition was simulated by applying a uniform heat flux at the bottom along an area equal to the die size. The remaining area along the bottom was modeled to be adiabatic. As can be observed in Figure 3.2, drastic improvement in the junction temperature is observed once boiling becomes the dominant mode of heat transfer in the thin two-phase heat spreader plate.

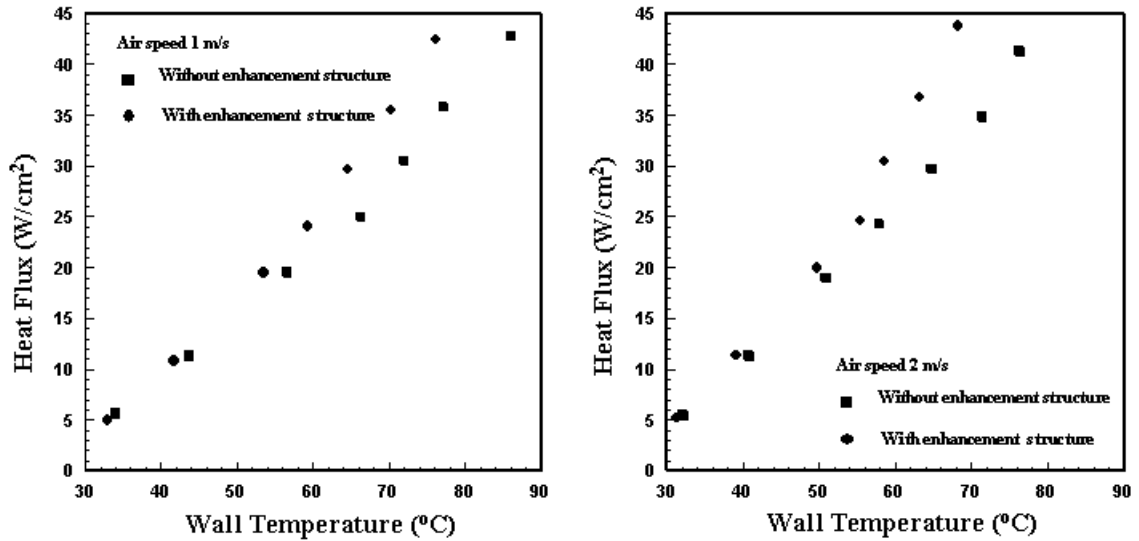


Figure 3.1: Performance enhancement on using the microstructure when compared to the base study without the enhancement structure. Inclusion of the enhancement structure in the evaporator section resulted in better heat transfer performance of the two-phase spreader.

An appropriate index of the overall thermal performance is the surface to ambient thermal resistance, defined as

$$R_{\text{tot}} = (T_{\text{wall}} - T_{\text{amb}})/Q \quad (3.1)$$

T_{wall} refers to the junction temperature, while T_{amb} denotes the ambient air temperature.

The boiling performance can be similarly defined by a boiling resistance as

$$R_{\text{bo}} = (T_{\text{wall}} - T_{\text{condenser}})/Q \quad (3.2)$$

where $T_{\text{condenser}}$ refers to the average temperature obtained from the thermocouples attached to the base of the fin structure at the periphery of the spreader plate. Figure 3.3 plots the above-defined resistance curves for the natural air-cooled two-phase spreader prototype. The sudden drop in the resistance values identifies the transition from natural convection to nucleate boiling.

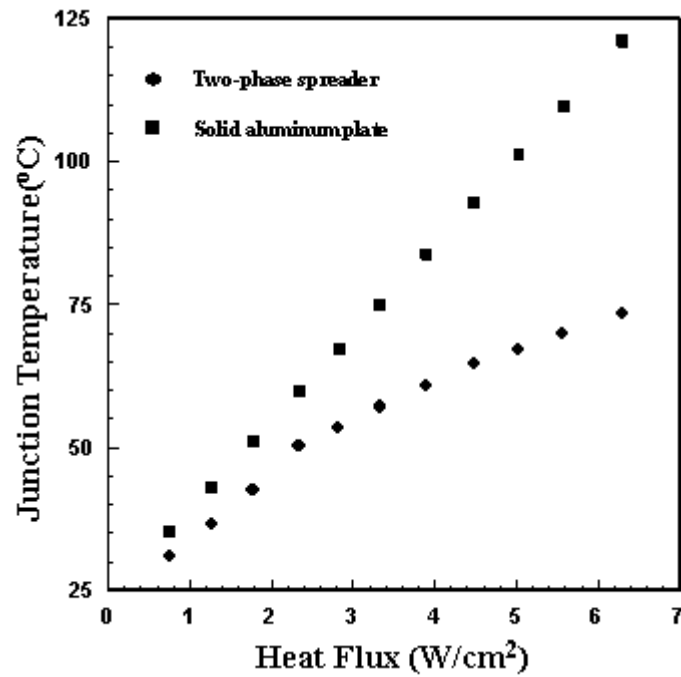


Figure 3.2: Performance evaluation of the thin two-phase spreader under natural-air cooled conditions.

The difference in the total resistance and the boiling heat transfer resistance can be ascribed to condensation resistance, which in turn is dependent on the external heat transfer rate. The external resistance plays an important role in the heat transfer performance of the two-phase spreader plate. Higher airside or condensation resistance directly impacts the rate at which the vapor condenses thereby increasing the system pressure. The increased system pressure in turn results in a corresponding increase in

the liquid saturation temperature and the junction temperature of the chip. As can be seen from Figure 3.3, the external heat transfer resistance accounts for nearly 70% of the total resistance value in the naturally air cooled study and needs to be reduced in order to achieve better thermal performance using the two-phase spreader plate.

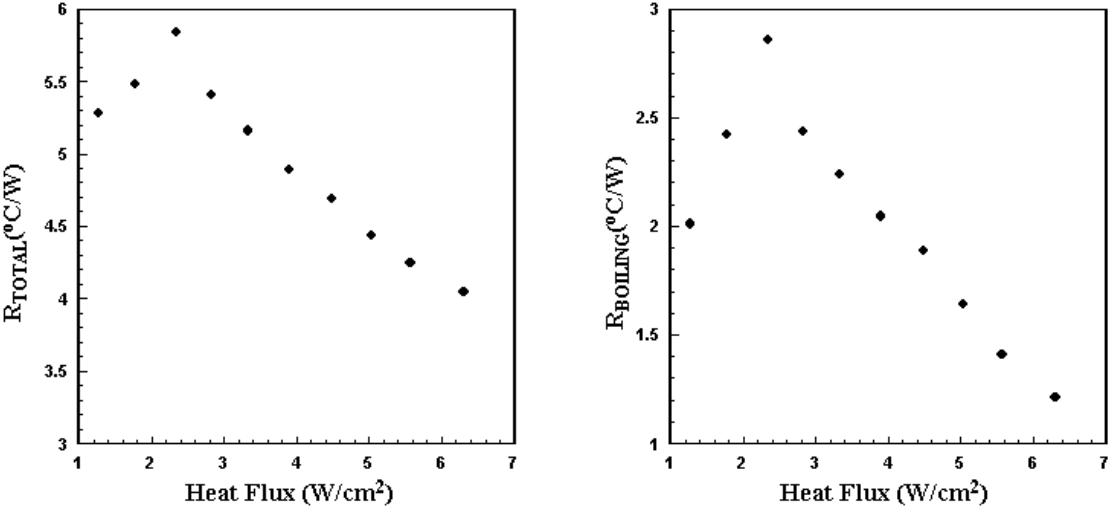


Figure 3.3. Plot of the total resistance and the boiling resistance for the naturally air-cooled flat plate two-phase heat spreader. The onset of boiling in the system results in a sudden drop in the resistances.

3.2 Effect of Condenser Cooling

Figure 3.4 displays the wall temperature as a function of heat flux for different air speeds in the wind tunnel. The performance of the heat spreader is influenced by the ability to condense the vapor in the system. Higher air speeds result in more heat being dissipated from the condenser walls. Subsequently, the bulk liquid temperature at high air speeds was lower than those attained at low air speeds, thereby enabling a marked improvement in the performance of the two-phase heat spreader. With increase in the air speed from 1 m/s to 2 m/s, for a power input of around 43 W, an 8 °C decrease in the

wall temperature from a high of 76.2 °C was achieved. The initial performance at low power levels, for different air speeds, was nearly the same with the heat being removed from the evaporator to the condenser by natural convection. A discernable change in performance was observed once boiling set in the system.

The temperature of the structure, monitored as a function of time, revealed a monotonic increase with increase in power dissipation levels after start-up. Once the surface temperature exceeded the saturation temperature, boiling initiated from the enhanced surface. No incipience excursion or a sudden drop in the surface temperature due to transition from natural convection to boiling was observed in any of the runs. Visual observation showed discontinuous vapor bubble columns generated randomly from the enhanced structure. Very few channels in the microstructure were seen to generate a column of bubbles in a steady fashion. The wall superheat required to initiate the Onset of Continuous Boiling (OCB), as visually observed, was ~15 °C irrespective of the air velocity used for cooling the condenser. The high superheat values required to initiate boiling can be attributed to the vacuum conditions under which the experiments were carried out. Lower pressures result in lower vapor densities and larger bubbles. This in turn increases the minimum superheat required for nucleation and delays the onset of continuous boiling.

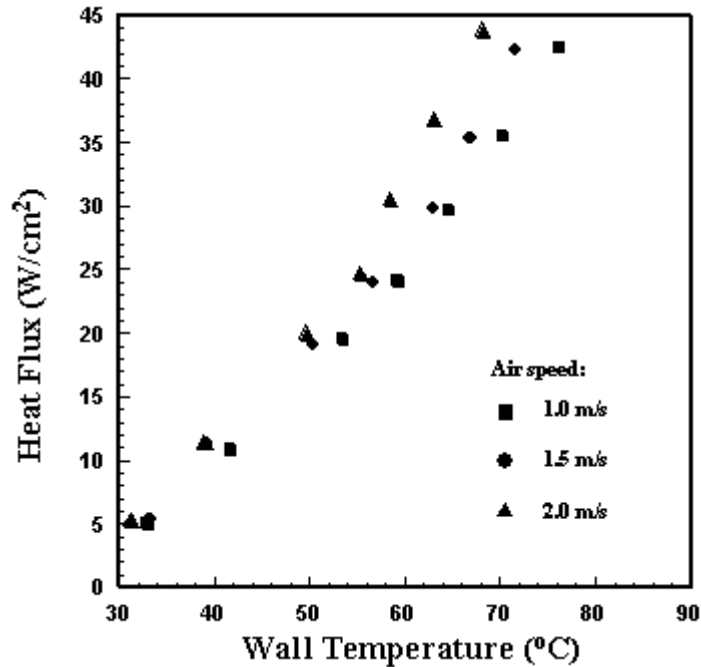


Figure 3.4: Variation of heat spreader wall temperature with respect to the total heat dissipated for different airflow rates employed to cool the condenser. The performance of the two-phase spreader plate was found to be dependent on the external convection resistance.

3.3 Effect of Enhancement Structure Size

Keeping the pitch and the pore size constant, the size of the enhancement structure was increased from a square of 15 mm to 25 mm. This resulted in increasing the total number of pores from 225 to 375. Figure 3.5 plots the performance of the two-phase heat spreader using two different enhancement structures at an air speed of 2 m/sec. The wall temperature values obtained in both cases were almost the same. No significant improvement in the performance of the spreader plate was achieved by increasing the number of pores in the microstructure. A similar trend was also noted at other air speeds. Visual observations carried out during the experiments showed that

despite an increase in the number of possible nucleation sites for boiling with the larger microstructure, not all pores were seen to be active during boiling.

In order to obtain a better understanding into why some sites remained inactive, a conduction model was carried out on a quarter geometry of the spreader plate (Figure 3.6a) with applied convective heat transfer boundary conditions on the evaporator section and condenser walls of the heat spreader to simulate the boiling and condensation process. Figure 3.6b shows the temperature variation long the evaporator section of the heat spreader for an input heat flux of 22 W/cm^2 . The spreading along the copper plate causes a large temperature variation across the evaporator section of the heat spreader resulting in almost a $11 \text{ }^\circ\text{C}$ drop in temperature from the center to the edge of the heat spreader evaporator. As a result, the channels along the edge of the $25 \text{ mm} \times 25 \text{ mm}$ enhancement structure are no longer active, resulting in inactive pores along the wider base area enhancement structure.

3.4 Effect of Liquid Fill Ratio

The effect of variation of liquid fill volume on the two-phase spreader performance was also studied. The enclosure was filled to a maximum height of 9.2 mm , which was considered as full fill. All other fill ratios were referenced to this level. A total of 9 ml of FC-72 was required to completely flood the evaporator and the condenser sections of the spreader plate. Tests were carried out for 100%, 55% and 22% fill ratios. The 22% fill ratio resulted in the enhanced surface just about being immersed in the inert coolant. The remaining volume was occupied by FC-72 vapor.

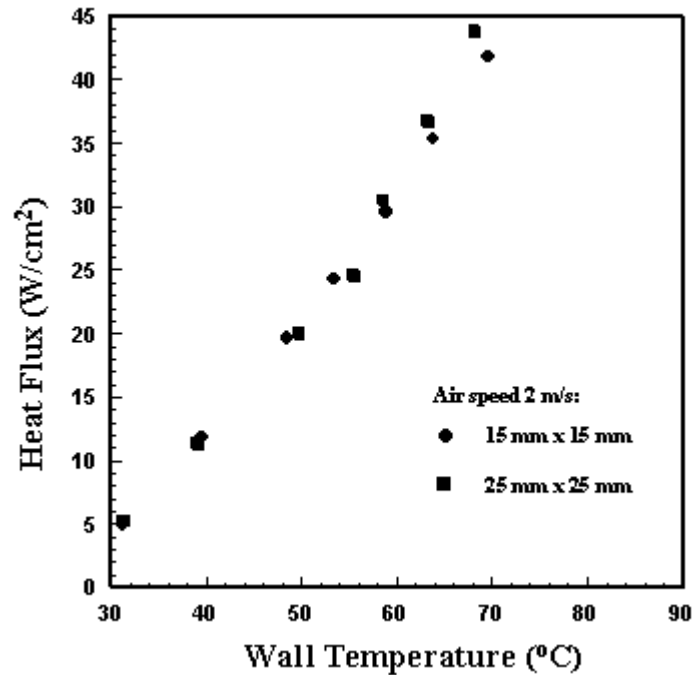


Figure 3.5: Boiling performance plot for two different microstructure base area sizes. The larger enhancement structure with more nucleation sites did not result in significant improvement in the heat transfer performance.

The performance of the system, as seen from the plot in Figure 3.7, is fairly insensitive to the liquid fill volume as long as the structure is completely submerged in the liquid. The 22% fill ratio case shows a slight degradation in performance at higher heat fluxes (20-40 W/cm²). At these high heat fluxes, considerable evaporation causes the liquid level to drop below the top surface of the enhanced structure. It was observed that a fill ratio, which ensures that the boiling structure is just about submerged at the highest heat flux, would result in a compact two-phase heat spreader without any degradation in the boiling performance. Ramaswamy et al [1998] noticed a similar trend in their study on the performance of a compact two-chamber two-phase thermosyphon.

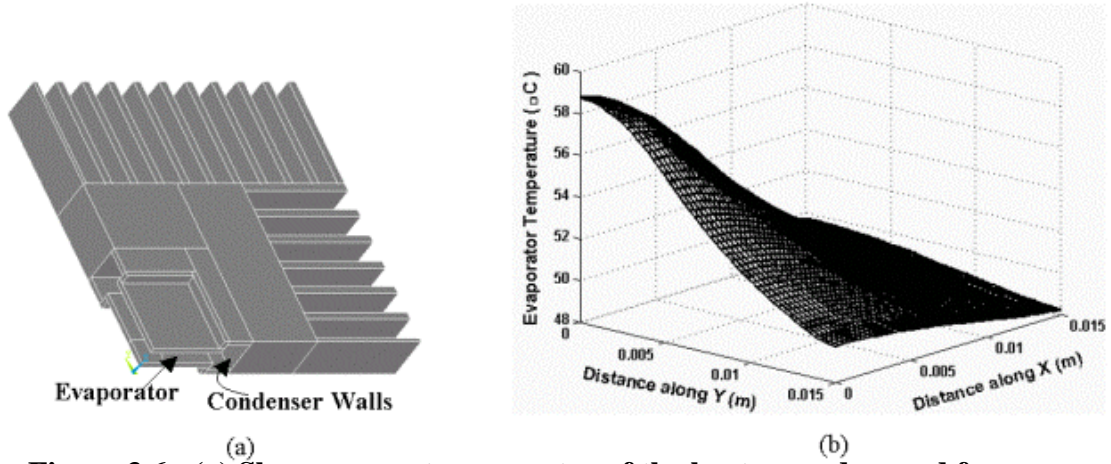


Figure 3.6: (a) Shows a quarter geometry of the heat spreader used for modeling the temperature profile variation along the evaporator. (b) Temperature gradient as a result of spreading along the evaporator section causes the channels along the edges to remain inactive.

3.5 Effect of Starting System Pressure

Low temperature operation of the two-phase heat spreaders can be achieved by either using coolant liquids with low boiling points, or by artificially lowering the boiling point through the creation of saturated liquid and vapor state in the heat spreader at low pressures. Analytical models that take into account the effect of temperature gradient and surface tension effects on bubble nucleation have been derived in the past (Dhir et al., [1999]). A simplistic model for an estimate of superheat required for the

onset of nucleation, derived from the Clausius-Clapeyron equation, $\Delta P \approx \frac{\Delta T \rho_v h_{lv}}{T_s}$ and

the equation of static equilibrium, $\Delta P = \frac{2\sigma}{r_e}$ is given as,

$$\Delta T_{\text{sup}} = \frac{1.6\sigma T_s}{R_c \rho_v h_{lv}} \quad (3.3)$$

where, the effective cavity size R_c is a function of surface characteristics and was postulated by Hsu [1962] to be $0.8 r_c$. Equation (3.3) implies that the superheat required for nucleation is much larger for reduced pressures since the vapor density is lower. Figure 3.8 plots the variation of heat transfer coefficient with respect to the heat flux for different starting system pressures. The heat transfer coefficient is defined as:

$$h = \frac{Q}{A_{ex}\Delta T_{sup}} \quad (3.4)$$

where Q is the heat dissipation, A_{ex} the external surface area of a solid block of the same dimensions as the enhanced structure and T_{sup} the wall superheat. The expected increase in wall superheat, as predicted by equation (3.3) for reduced system pressure results in lower heat transfer coefficient values. However, this observed deterioration in performance at low starting system pressures gets rectified at higher power dissipation levels. At higher heat fluxes, the rapid vaporization of the coolant liquid due to excessive boiling increases the system pressure, decreases the wall superheat and results in a corresponding increase in the heat transfer coefficient values.

The advantage of operating at reduced system pressures can be observed in Figure 3.9a where the decrease in the saturation temperature at lower pressures results in lower wall temperatures. Nucleate boiling from the enhanced structure was visually observed at $40.1\text{ }^{\circ}\text{C}$, $53.2\text{ }^{\circ}\text{C}$ and $61.8\text{ }^{\circ}\text{C}$ for corresponding starting pressures of 34.1 kPa , 42.6 kPa and 60.5 kPa . A discernable shift in the spreader plate performance is observed with the change in heat removal mechanism from natural convection to the nucleate boiling regime.

The heat transfer coefficient for the single-layer enhancement structure, at a starting pressure of 34.1 kPa , is shown in Fig. 3.10. The heat transfer coefficient

increases monotonically at low wall superheats before slowing down to sharply reduce at higher wall superheats. At high wall superheats, the bubbles start merging, preventing liquid from reaching the boiling surface. This reduces the convective heat transfer component, thereby resulting in the observed decrease in the heat transfer coefficient.

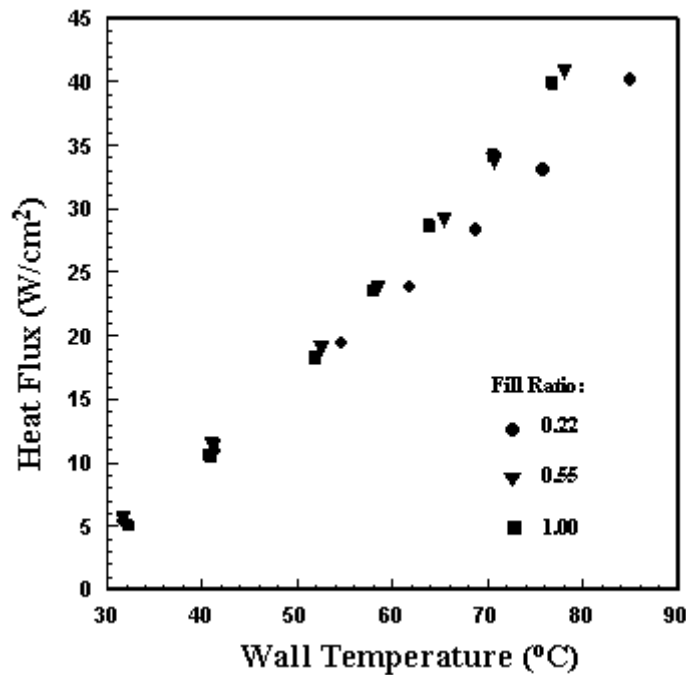


Figure 3.7: Performance evaluation of the heat spreader for different fill ratios of FC-72. Fill ratios resulting in flooding of the evaporator section show similar heat transfer performance.

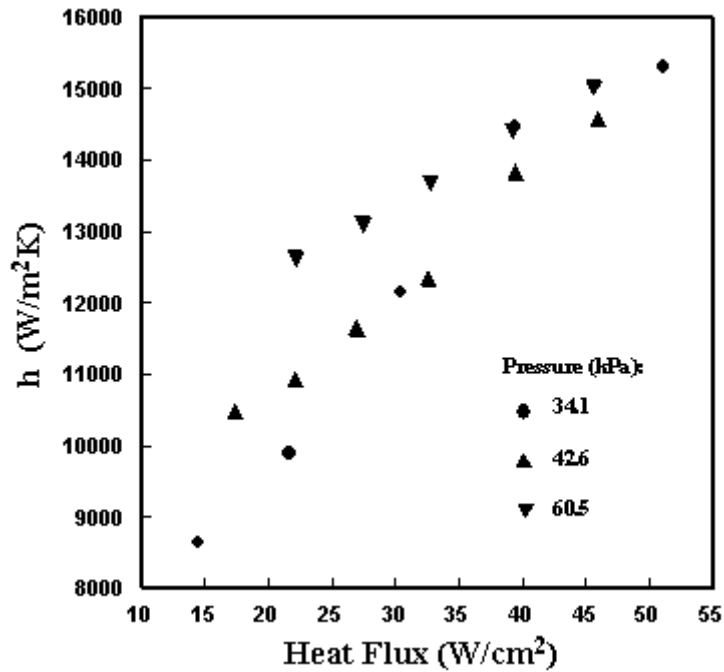


Figure 3.8: Variation of h with q'' of PF5060 for different starting system pressures.

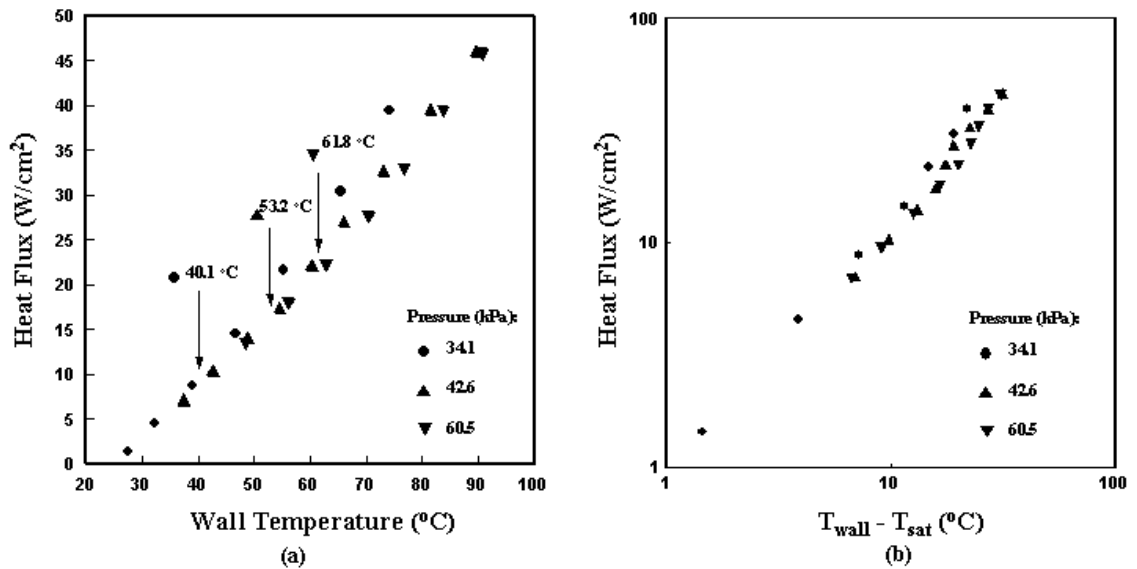


Figure 3.9: Heat flux versus wall temperature of PF5060 for 34.1, 42.6 and 60.6 kPa. (a) Decrease in system pressure results in lower wall temperature. (b) Boiling plots at different starting pressure collapse to a single curve

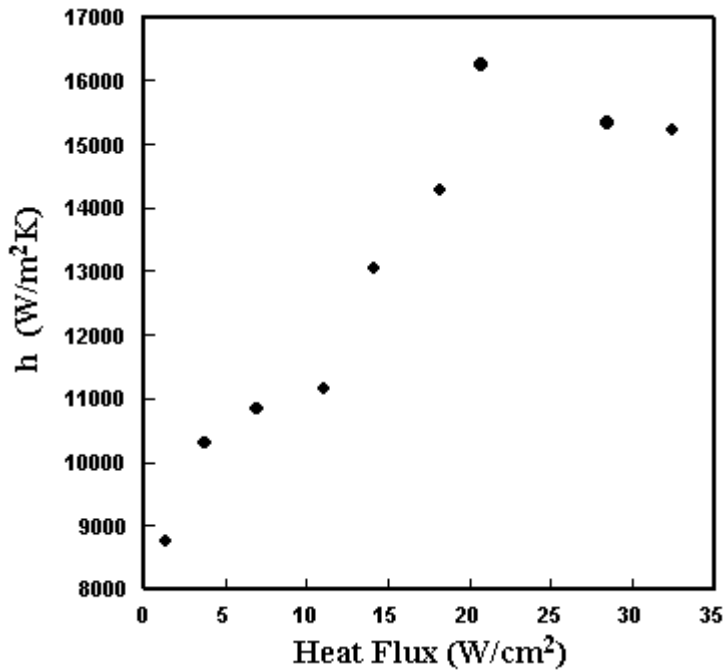


Figure 3.10: Heat transfer coefficient as a function of wall superheat for a system pressure of 34.1 (kPa).

3.6 Effect of Coolant Fluid

Figure 3.11 shows the thermal performance of the copper heat spreader for three different Fluorinert liquids. Table 3.1 lists the thermal properties of these fluids used. These tests were carried out with the starting system pressure almost equal to the saturation pressure at room temperature. The performance of the two-phase spreader plate for different coolant liquids is almost the same at low heat fluxes where the heat transfer mechanism is primarily through natural convection. At high heat fluxes, the performance of the spreader plate is seen to depend on the nucleate boiling heat transfer mechanism. Among the Fluorinert liquids studied, the onset of nucleate boiling was seen to be fastest with FC-87 and slowest with FC-84. Higher power levels initially

resulted in vigorous boiling of the liquid. The system pressure increased, causing a corresponding increase in the saturation temperature of the liquid. This increase in saturation temperature subsequently moderated the boiling process in the evaporator section of the heat spreader. Liquids with lower boiling points resulted in lower wall temperatures due to their early transition to the nucleate boiling regime. As observed in Figure 3.11a, a 10°C difference in wall temperature between FC-87 and FC-84 was observed for a heat input of around 30 W/cm². The properties of the three Fluorinert liquids are comparable at the same saturation temperature and show similar boiling performance as seen in Fig. 3.11b.

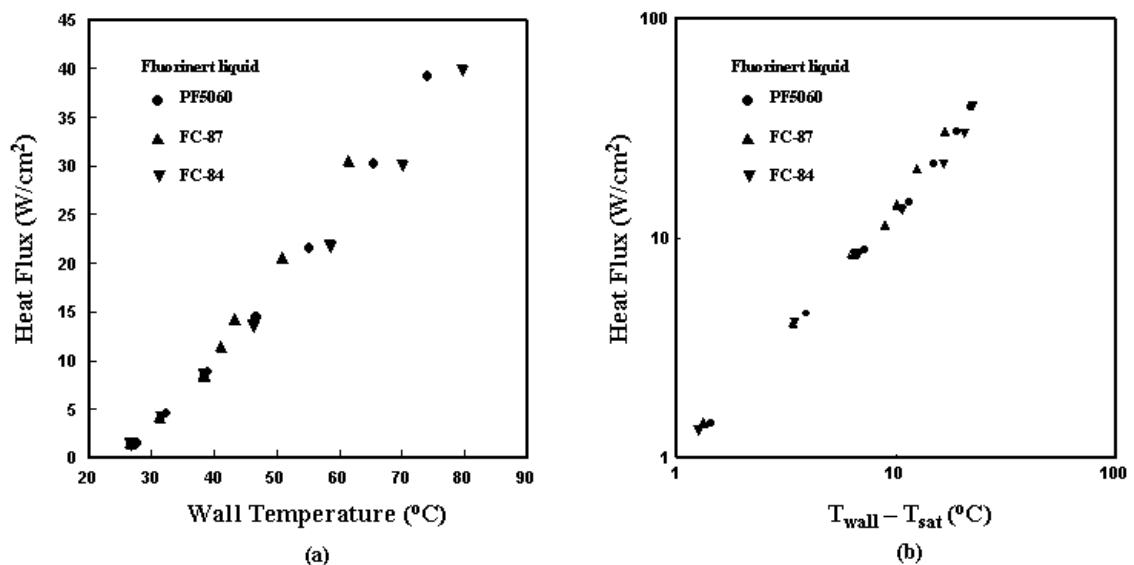


Figure 3.11: Thermal performance for three different Fluorinert liquids with the starting system pressure almost equal to the saturation pressure at room temperature.

3.7 Effect of Stack Height

The effect of varying the number of layers on the thermal performance of the spreader was studied by stacking two or more layers to form porous three-dimensional

structures. The individual layers were initially oxidized in a high temperature oven. The top and bottom surfaces of each plate were then polished, leaving the channels selectively oxidized. The structures were then dip coated with solder (63Pb-37Sn). Since the channels were oxidized, the solder did not fill the pores. A uniform layer of solder was coated only on the top and bottom surfaces. The required number of layers was then stacked and the solder reflowed at 200 °C to form the three-dimensional structure.

Table 3.1: Transport properties of various liquid coolants (Danielson et al., [1987])

Property	Perflourinated Liquid Designation			
	FC-87	PF5060	FC-84	Water
Boiling point, °C	30	56	83	100
Specific heat, J/kg K	1088	1088	1130	4184
Thermal conductivity, W/m K	5.5×10^{-2}	5.45×10^{-2}	5.35×10^{-2}	6.8×10^{-1}
Surface tension, N/m	8.9×10^{-3}	8.5×10^{-3}	7.7×10^{-3}	5.9×10^{-2}
Dynamic viscosity, kg/m sec	4.2×10^{-4}	4.5×10^{-4}	4.2×10^{-4}	2.7×10^{-4}

Figure 3.12 shows the observed decrease in wall temperature with heat flux, obtained through stacking of two and three layer structures in the evaporator section of the spreader plate. The curves show an improvement in the heat dissipation with additional layers (increase in stack height). For a three-layer stack, the enhancement is significant at low wall temperatures (30 % at 35 °C), reducing at intermediate wall

temperatures (16 % at 55 °C) and once again rising at higher wall temperatures (23 % at 75 °C).

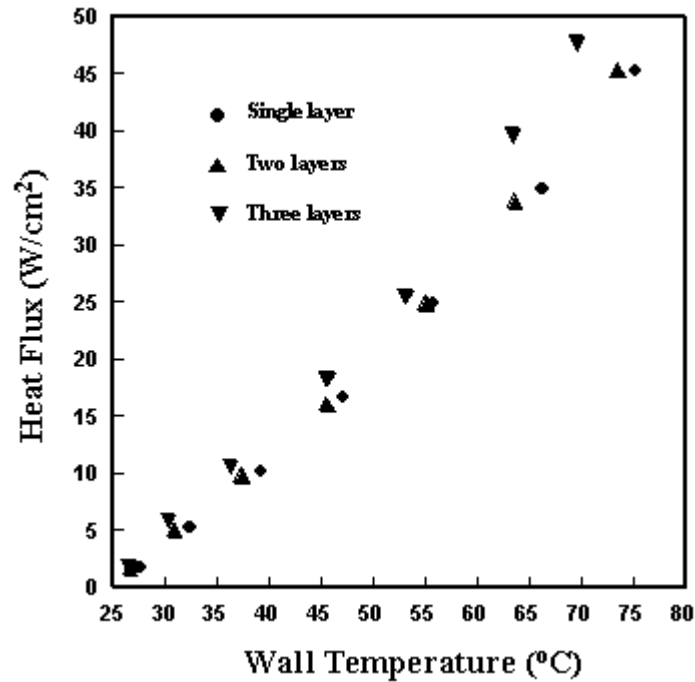


Figure 3.12: Effect of varying stack height on boiling heat transfer of PF5060.

The effect of stack height on the heat dissipation can be captured through a one-dimensional fin-model. The energy equation for one-dimensional steady state heat transfer through a fin of uniform cross-sectional area is given as:

$$\frac{d^2T}{dz^2} - \frac{hP_s}{kA_c}(T - T_\infty) = 0 \quad (3.5)$$

The boundary condition for the above problem is shown in Figure 3.13. The heat transfer coefficient (h) is a function of the local temperature $T(z)$ and is obtained from the experiments on a single layer structure.

Figure 3.14 shows the heat flux as a function of the heat spreader wall temperature, as captured by the conduction model and compares its performance to that obtained experimentally using the two-layer and three-layer structure. Though the model captures the trends at low to moderate heat fluxes, large errors (17 % at 70 °C) are observed at high heat fluxes where nucleate boiling becomes the fundamental model of heat transfer from the enhancement surfaces. The possible reason for this discrepancy is a phenomenological difference between boiling from the sub-surface layers and that from the top layer. For a multi-layer structure, the top surface of only the top layer contributes to boiling. For all the other layers, only the sides contribute to boiling.

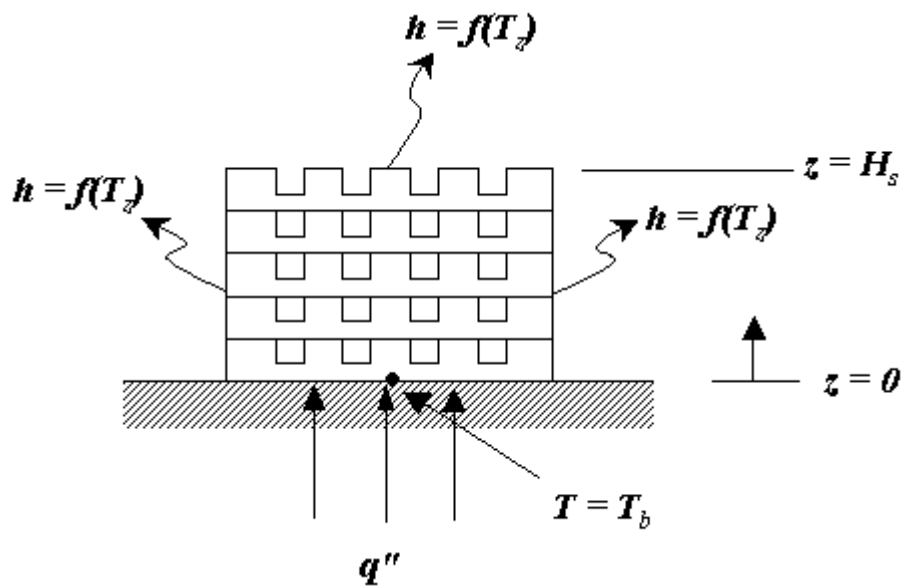


Figure 3.13: Boundary conditions on the enhanced structure for numerical analysis.

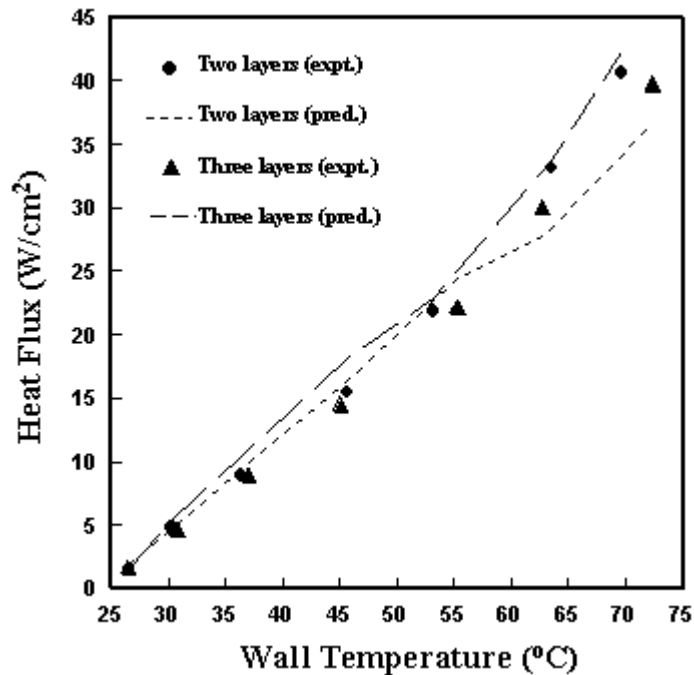


Figure 3.14: Comparison of conduction model predictions of stacked structures with experimental results obtained with PF5060.

3.8 Orientation Study

Figure 3.15 shows the performance of the two-phase spreader plate for various inclination angles. A zero-degree inclination corresponds to the two-phase spreader being parallel to the horizontal plane and a ninety-degree orientation results in the spreader plate being perpendicular to the horizontal plane. At low heat fluxes, the performance of the spreader plate was found to be relatively independent of the inclination angle. At higher heat fluxes, the ninety-degree orientation resulted in relatively poor heat transfer performance. In order to better understand the deterioration in performance at high heat fluxes, visualization study of the evaporator section of the heat spreader was carried out using a high-speed camera.

The flow visualization set-up consisted of a high speed CCD camera (Model - Phantom) capable of frame rates up to 1600 frames/sec with a split field. A zoom lens (Navitar 6000 – 6.5X par focal zoom) was used to magnify the area of interest and work at close distances to the boiling enhancement structure. The lens is capable of a variable magnification of 1 – 6.5 times the original size of the object. A 150 W fiber optic light guide was used for illuminating the structure.

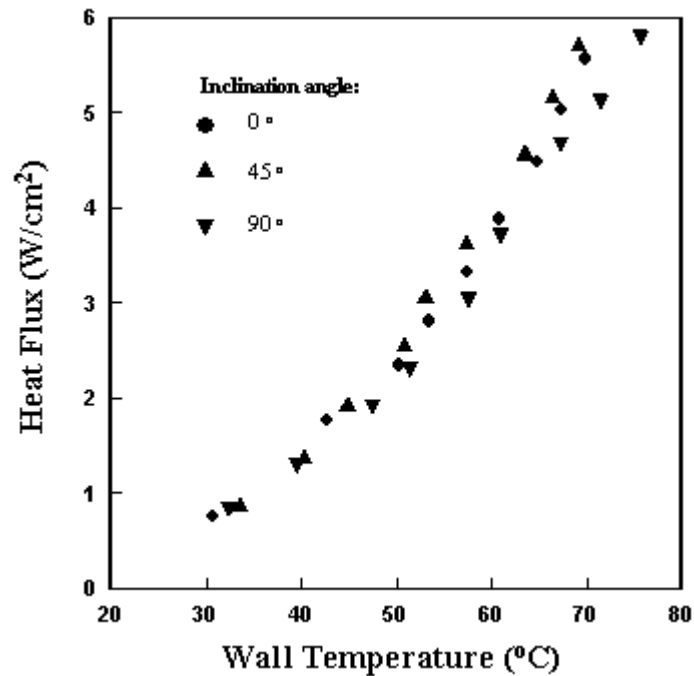


Figure 3.15: Plot of two-phase spreader performance at various orientations. Slight deterioration in performance observed at high heat fluxes for 90° inclination.

Figure 3.16 shows snapshots of steady state boiling from the enhancement structure in the evaporator section of the two-phase spreader plate for different power levels. As seen from the figure, increase in heat flux results in slow transition from natural convection to nucleate boiling with vigorous generation of bubbles at higher

heat fluxes. Even though the geometry constraint ensures that the enhancement structure remains flooded initially, excessive evaporation at high heat fluxes results in partial dry out of the porous boiling structure (Figure 3.16f). This could probably explain the observed decrease in performance in the vertical orientation where gravitational forces prevent the easy return of the liquid from the condenser to the evaporator. Similar dry out conditions is to be expected for other inclination angles, though their occurrence is likely to be at relatively higher heat fluxes in comparison to the vertical orientation. In the present study, no such partial dry-out was observed for the range of heat fluxes considered.

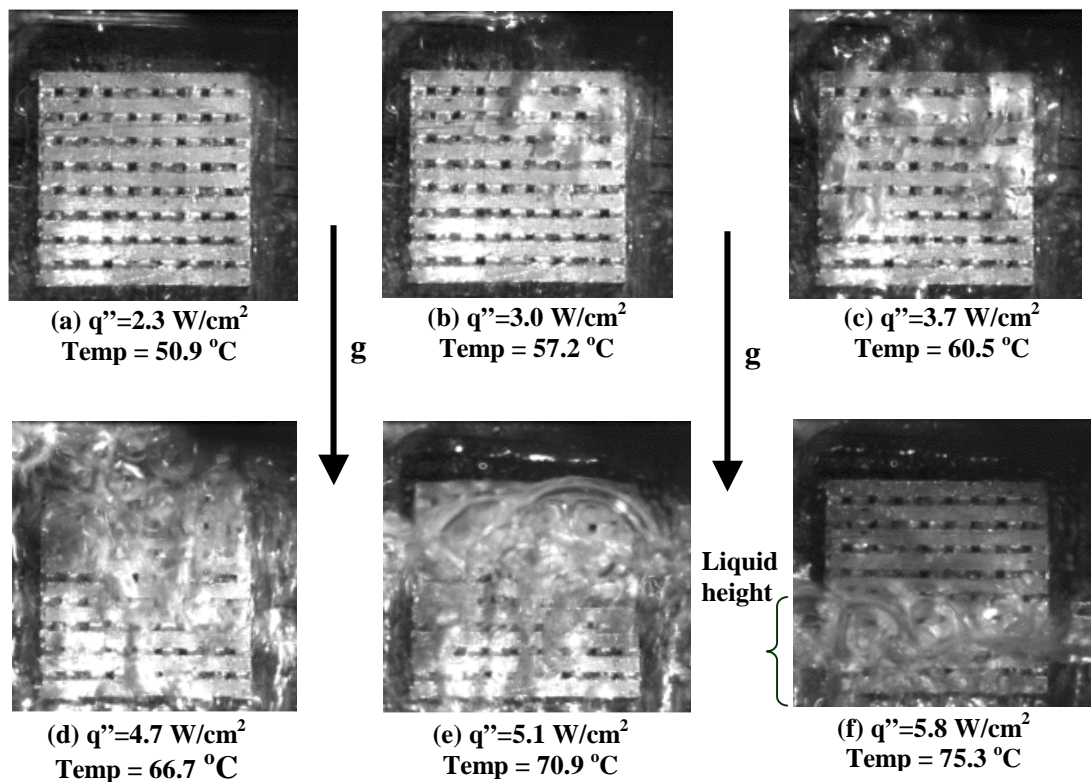


Figure 3.16: Snapshots of steady state boiling from the enhancement structure in the evaporator section of the two-phase heat spreader at 90° inclination. Rapid evaporation at high heat fluxes result in partial dry out of the enhancement structure.

3.9 Summary and Conclusions

The primary conclusions of the study on system parameters are listed below.

- a) The boiling enhancement structure was found to result in a significant decrease in the wall temperature values compared to the case where the porous structure is not employed in the evaporator section of the spreader plate.
- b) The performance of the heat spreader to a large extent depends on the ability to cool the condenser section. Higher air speeds resulted in a marked decrease in the wall temperature values for the same power levels.
- c) The liquid fill volume has negligible effect on the boiling performance of the heat spreader, as long as the enhancement structure remains immersed in the liquid.
- d) The performance of the two-phase heat spreaders was found to depend on the liquid coolant used in the phase change process.
- e) The decrease in saturation temperature at low pressures provides the benefit of lower wall temperatures.
- f) Significant improvement in heat transfer performance (15% - 30%) can be achieved by stacking multiple layers to form three-dimensional porous enhancement structures.
- g) The two-phase heat spreaders performance was found to be relatively independent of the orientation at low heat fluxes. Slight deterioration in performance was observed at high heat fluxes due to partial dry out of the enhancement structure.

CHAPTER 4: SEMI-ANALYTICAL MODEL FOR BOILING FROM ENHANCED STRUCTURES

Nucleate boiling from structured surfaces result in high heat transfer rates with very small rise in the surface temperature. This knowledge has been used extensively to improve the performance of heat exchangers and process equipment, through the use of enhanced tubes for promoting boiling / condensation heat transfer process.

Nakayama et al. [1980b] came up with three possible modes of boiling mechanism from structured surfaces, namely the “flooded” mode, the “suction-evaporation mode” and the “dried-up mode” (Fig. 1.9). Based on the above observations of boiling mechanism modes, Webb & Haider [1992], Chien and Webb [1998c] and Ramaswamy et al. [2003], have proposed mechanistically based analytical models to predict boiling performances of structured enhanced surfaces. Webb & Haider’s model is based on the “flooded” mode regime and assumes alternate zones of liquid and vapor slugs in the sub-surface tunnels, while Chien’s and Ramaswamy’s model focus on the “suction-evaporation” mode of boiling from enhanced surfaces.

Both Chien’s and Ramaswamy’s model require the specification of the Hamaker constant for calculating the liquid saturation temperature. Chien’s model assumes the Hamaker constant value for R-113 to be 2.0×10^{-12} J while Ramaswamy’s model uses a value of 1×10^{-13} J for FC-72. Ramaswamy et al [2003] note that their model is highly sensitive to the value of the Hamaker constant used, thereby requiring its accurate evaluation. Dasgupta et al. [1993] carried out experiments to determine the equilibrium disjoining pressure from thin evaporating menisci and found that the Hamaker constant is a function of the liquid surface combination and the wall superheat value. For an

octane/silicon system, the Hamaker constant was measured to be in the range $3.0 - 0.69 \times 10^{-21}$ J for wall superheats in the range $0.000045 - 0.002$ °C. More generally, the Hamaker constant for two macroscopic phases interacting across a medium can be derived using the Lifshitz theory of Van der Waals forces (Israelachvili, [1991]). The above theory, when used in calculating the Hamaker constant for CCl_4 /copper system, results in a value of 1.18×10^{-19} J. Substituting a value of 10^{-19} J for the Hamaker constant in Chien's / Ramaswamy's model results in very large discrepancies between the predicted results and the experimental data available in the literature for boiling from enhanced surfaces. Moreover, both Chien's and Ramaswamy's models are based on thin film evaporation across the meniscii along the corners of the enhancement feature and fail to account for observed boiling enhancement from circular sub-surface tunnels where no such meniscii exist.

Visualization experiments performed by Nakayama et al. [1980a] and Arshad and Thome [1983] show the existence of an advancing liquid vapor interface in the re-entrant cavities of the enhancement structure. More recently, Ghiu et al [2001] carried out visualization studies on transparent enhancement structures similar to those used by Nakayama et al. [1980a]. Their experiments confirmed the presence of alternating liquid-vapor slug regions in the sub-surface tunnels of the enhancement structure.

Webb & Haider's [1992] analytical model of sub-surface tunnels filled with vapor near the active pores and surrounded by liquid slugs most accurately captures the boiling mechanism from structured surfaces observed in the visualization experiments. The current study builds on Haider's work to develop a unified boiling model for

predicting the bubble dynamics from enhanced structures and compares with experimental results reported in the literature.

4.1 Semi-Analytical Model

The semi-analytical model developed captures the boiling of highly wetting liquids from structured surfaces with subsurface tunnels having circular cross section. The model can be suitably modified for predicting the performance of tunnels with any cross sectional type by reducing the geometry to an equivalent circular channel. The model envisions the existence of a spherical bubble inside the sub-surface tunnel at the start of a bubble departure cycle (Fig. 4.1a). Evaporation on the liquid-vapor interface across the two menisci and the intermediate thin liquid film causes the vapor plug to expand within the tunnel (Fig. 4.1b). The vapor expansion occurs in the tunnel till the pressure is greater than the surface tension force on the pore ($4\sigma/D_p$) (Fig. 4.1c). At this point, bubble growth occurs outside the tunnel (Fig. 4.1d) till the detaching forces overcome the forces that keep the bubble attached to the enhanced surface.

The departure diameter is obtained based on a balance of the static and dynamic forces acting on a bubble. Bubble frequency is defined as the inverse of the total time for one bubble cycle and is calculated based on the time taken for a bubble to reach its departure diameter. The heat dissipated through evaporation inside the tunnels (Q_t) is combined with the enhanced convection on external surfaces (Q_{ex}) for arriving at the total heat flux. The nucleation site density (n_s) or the total number of bubbles formed per unit area is required for computing the total heat flux and is obtained through an empirical correlation.

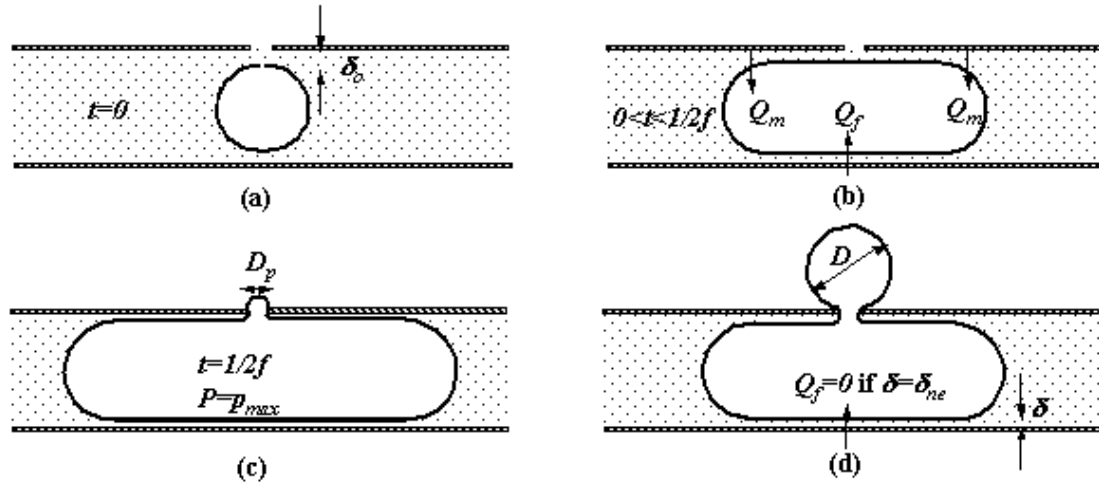


Figure 4.1: Envisioned bubble formation and departure in the “flooded” mode regime.

4.1.1 Modeling bubble departure diameter

Most existing models for bubble departure from structured surfaces consider only the static forces acting during bubble growth. Nakayama et al. [1980b] developed an empirical correlation for bubble departure through the balance of buoyancy and surface tension forces. Webb & Haider [1992] replaced the empirical constant in Nakayama’s model by introducing the contact angle θ in the formulation. More recently, Ramaswamy et al. [2003] accounted for the effect of dynamic forces in their bubble departure model.

The mechanism of bubble growth for structured surfaces involves evaporation of the liquid menisci inside the sub-surface tunnels of the enhancement structure. The flow of vapor from the tunnels, during the growth of bubble on the surface of the enhancement structure, results in a momentum flux force that has been neglected in previous models. The present model for bubble departure assumes the departing

bubbles to be spherical in shape and attached to the surface pore during the bubble growth. The departure diameter is predicted by including the effect of momentum flux force along with other static and dynamic forces, namely unsteady growth, buoyancy, surface tension, bubble inertia and liquid inertia. The momentum flux force is given by:

$$F_{mom} = \frac{\rho_v \dot{V}_b^2}{\left(\frac{\pi}{4}\right) D_p^2} \quad (4.1)$$

where \dot{V}_b is the rate of change of the truncated bubble volume with time and is given as

$$\dot{V}_b = \frac{2\pi\dot{R}}{3} \left(\frac{3D_b^2}{4} + \frac{3D_b^3 - 2D_b D_p^2}{4\sqrt{D_b^2 - D_p^2}} + \frac{D_b D_p^2}{8\sqrt{D_b^2 - D_p^2}} \right) \quad (4.2)$$

The bubble growth from structured surfaces is typically inertia controlled. Chien and Webb [1998c] modified the growth equation of Mikic et al. [1969] to calculate the growth rate as

$$\dot{R} = C_{tg} \sqrt{\left(\frac{\pi}{7} \frac{h_{fg} \rho_v \Delta T_{sup}}{\rho_l T_{sat}} \right) \left(\frac{D_b - D_p}{D_b + D_p} \right)} \quad (4.3)$$

where the constant C_{tg} was evaluated as 0.0296 based on a curve fit of the bubble growth data.

The expressions used for the remaining forces (unsteady growth, buoyancy, surface tension, bubble inertia and liquid inertia) in the force balance study are similar to those derived in Ramaswamy et al [2003] and have been repeated for the sake of completeness.

(a) Unsteady growth force: The expression for an inertia driven growth force developed by Zeng et al. [16] is given as

$$F_{ug} = 10\rho_l\pi\dot{R}^2R^2 \quad (4.4)$$

As the bubble departure diameter is not known a priori, calculation of the growth force becomes iterative.

(b) Buoyancy force: The buoyancy force on a bubble is given as

$$F_B = (\rho_l - \rho_v)gV_b \quad (4.5)$$

where V_b is the truncated bubble volume at departure and is given as

$$V_b = \frac{\pi}{3} \left(\frac{D_b^3}{4} + \frac{D_b^2}{4} \sqrt{D_b^2 - D_p^2} + \frac{D_p^2}{8} \sqrt{D_b^2 - D_p^2} \right) \quad (4.6)$$

(c) Surface tension force: The surface tension force is given as

$$F_{st} = \sigma\pi D_p \sin \theta \quad (4.7)$$

where the contact angle θ is evaluated as

$$\theta = \sin^{-1} \left(\frac{D_p}{D_b} \right) \quad (4.8)$$

(d) Bubble inertia force: The expression for bubble inertia force, as used by Sharma [1998]

$$F_{bi} = m \frac{dv_g}{dt} + v_g \frac{dm}{dR} \frac{dR}{dt} \quad (4.9)$$

reduces to

$$F_{bi} = \rho_v \frac{\pi}{3} \dot{R}^2 \left\{ \frac{3D_b^2}{4} + \frac{1}{4} \left(\frac{3D_b^3 - 2D_b D_p^2}{\sqrt{D_b^2 - D_p^2}} + \frac{D_b D_p^2}{2\sqrt{D_b^2 - D_p^2}} \right) \right\} \quad (4.10)$$

for a linear bubble growth rate with the velocity at the bubble center given by $v_g = dR/dt$.

(e) Lift force: The departing bubble has a tendency to drag the next bubble growing at the same pore. The lift force due to wake of the departing bubble is modeled as

$$F_L = 2.4\pi\rho_l(D_b\dot{R})^2 \quad (4.11)$$

The buoyancy force, lift force and the momentum flux force tends to pull the bubble off the pore, while the growth force, the surface tension force and the bubble inertia force keep it attached. The bubble departure diameter is obtained by solving the force balance equation

$$F_{ug} + F_{st} + F_{bi} = F_b + F_{mom} + F_L \quad (4.12)$$

4.1.2 Modeling tunnel heat transfer

The tunnel heat flux during one bubble cycle of frequency f is calculated based on the liquid evaporation from the thin film (Q''_f) and the two menisci at each end of a vapor plug (Q''_m) in the tunnel. Evaporation from the thin film occurs till the non-evaporating film thickness is reached wherein the inter-molecular forces between the solid tunnel wall and the liquid in the thin film creates an energy barrier that hinders evaporation. The non-evaporating thickness is calculated by

$$\delta_{ne} = \left(\frac{C_h T_{sat}}{\rho_l h_{fg} \Delta T_{sup}} \right)^{1/3} \quad (4.13)$$

Since all the heat transferred to the vapor zone is latent, the tunnel heat flux (Q_t'') equals the latent heat of the vapor contained in a bubble and is given by

$$Q_t'' = n_s \int_0^{1/f} (2Q_m'' + Q_f'') dt = \frac{\pi}{6} \rho_v h_{fg} D_b^3 n_s \quad (4.14)$$

4.1.3 Modeling bubble frequency

The bubble frequency f is obtained by solving eq. 4.14 through modeling of thin film (Q_f'') and meniscus (Q_m'') heat transfer rates. Q_m'' is obtained through calculation of the radial heat conduction and is given by (Fig. 4.2)

$$\begin{aligned} Q_m'' &= 2\pi k_l (T_w - T_{sat}) \int_0^{r_t - \delta} \frac{dx}{\ln \left(\frac{r_t}{\sqrt{(r_t - \delta)^2 - x^2}} \right)} \\ &= 4\pi r_t k_l (T_w - T_{sat}) \sqrt{\frac{r_t}{2\delta}} \tan^{-1} \left(\sqrt{\frac{r_t}{2\delta}} \right) \quad (\text{for } \delta \ll r_t) \end{aligned} \quad (4.15)$$

The instantaneous conduction heat transfer through the thin-film region is modeled by solving the radial conduction equation across the cylindrical thin film and equals

$$Q_f'' = \frac{2\pi r_t k_l (T_w - T_{sat}) L}{\delta} \quad (4.16)$$

where L is the instantaneous length of the thin-film region. The time dependent thin-film thickness is modeled by equating the latent heat required to evaporate a differential cylindrical liquid volume of thickness $d\delta$ during time dt to the thin-film heat

transfer. Substituting for Q_f'' from eq. 4.16, the differential form of the interfacial thickness is derived to be

$$\delta d\delta = \frac{-k_l(T_w - T_{sat})dt}{\rho h_{fg}} \quad (4.17)$$

Integrating the above equation from the start of the cycle ($t=0, \delta=\delta_0$), the interfacial thickness is obtained as

$$\delta = \sqrt{\delta_0^2 - \frac{2k_l(T_w - T_{sat})t}{\rho h_{fg}}} \quad (4.18)$$

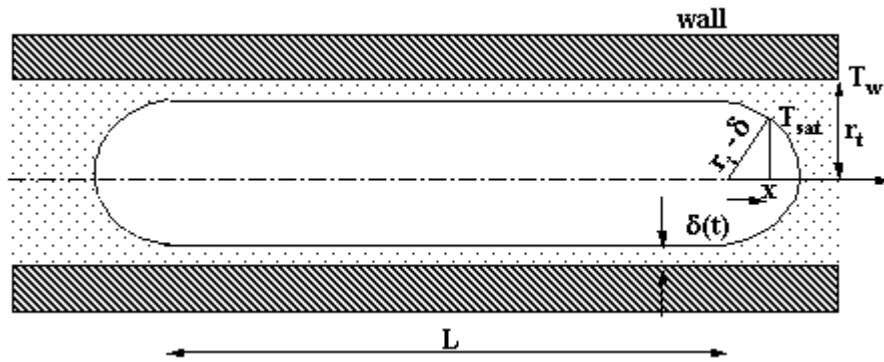


Figure 4.2: Geometry of vapor plug inside the tunnel used for computing Q_m' and Q_f'' .

Based on existing literature on boiling experiments from micro-structures, Webb & Haider [1992] assumed the existence of liquid-vapor menisci oscillating back and forth inside the enhanced surface tunnels and proposed the following relationship for the driving pressure difference (Δp) during the expansion phase,

$$\Delta p = (p_{sat,max} - p_{sat,min}) \sin(\pi ft) \quad (4.19)$$

The pressure in the vapor plug attains a maximum when the vapor embryo just protrudes from the surface pore

$$p_{sat,max} = p_{sat} + \frac{4\sigma}{D_p} \quad (4.20)$$

and the minimum pressure in the vapor plug occurs when the bubble growing at the top of the tunnel assumes the departure diameter

$$p_{sat,min} = p_{sat} + \frac{4\sigma}{D_b} \quad (4.21)$$

The streamwise momentum equation for the oscillatory motion of the liquid slug in the tunnel reduces to

$$\frac{\partial u}{\partial t} = \frac{-\Delta p_{max} \sin(\pi f t)}{\rho x_m} + \frac{\nu}{r} \frac{\partial}{\partial r} \left(r \frac{\partial u}{\partial r} \right) \quad (4.22)$$

where x_m represents the mean length of the liquid slug inside the tunnel. Haider [1994] showed the assumption of inviscid flow inside the enhanced surface tunnels results in negligible error in the tunnel heat transfer prediction. Neglecting the viscous term in the momentum equation (Eq. 4.22) results in the solution of the velocity to be

$$u = \left(\frac{\Delta p_{max}}{\pi f \rho x_m} \right) \cos(\pi f t) \quad (4.23)$$

The maximum expansion length of the vapor zone displaced during half of the cycle is given by

$$\begin{aligned} L_{max} &= \frac{16}{D_p^2} \int_0^{1/2f} dt \int_0^{D_p/2} u r dr \\ &= \frac{2\Delta p_{max}}{\pi^2 f^2 \rho x_m} \end{aligned} \quad (4.24)$$

The instantaneous length of the thin-film region during the expansion phase is modeled using

$$\begin{aligned}\frac{dL}{dt} &= 2u \\ \Rightarrow L &= L_{\max} \sin(\pi ft)\end{aligned}\quad (4.25)$$

The pressure drop across the slug during the contraction phase is modeled as

$$\Delta p = \Delta p_{\max} \cos(\pi ft) \quad (4.26)$$

with the solution of the slug velocity in the contraction phase given by

$$u = -\left(\frac{\Delta p_{\max}}{\pi f \rho x_m}\right) \sin(\pi ft) \quad (4.27)$$

Application of the above velocity field results in the length of the thin-film region in the contraction phase as

$$L = L_{\max} (1 + \cos(\pi ft)) \quad (4.28)$$

The increase in the mass of the vapor as it expands from the minimum vapor pressure (p_{\min}) to the maximum vapor pressure (p_{\max}) is given by

$$m_{\max} - m_{\min} = \frac{1}{h_{fg}} \int_0^{1/2f} (2Q_m'' + Q_f'') dt \quad (4.29)$$

Assuming the heat transfer rate during the expansion and contraction phase of the vapor plug to be the same with small variations in the vapor density, eq. 4.29 reduces to

$$m_{\max} - m_{\min} = \rho_v (V_{\max} - V_{\min}) = \frac{\pi}{12} \rho_v D_b^3 \quad (4.30)$$

The minimum (V_{\min}) and maximum (V_{\max}) volume of the vapor plug is obtained from a geometrical analysis of the system to be

$$V_{\min} = \frac{4}{3} \pi (r_i - \delta_o)^3 \quad (4.31a)$$

$$V_{\max} = \pi(r_t - \delta)^2 L_{\max} + \frac{4}{3} \pi(r_t - \delta)^3 + \frac{2}{3} \pi \left(\frac{D_p}{2} \right)^3 \quad (4.31b)$$

Substituting eq. 4.31 in eq. 4.30 results in

$$L_{\max} = \frac{D_b^3}{12(r_t - \delta)^2} - \frac{4}{3(r_t - \delta)^2} \left\{ (\delta_o^3 - \delta^3) - 3r_t(\delta_o^2 - \delta^2) + 3r_t^2(\delta_o - \delta) - \frac{D_p^3}{16} \right\} \quad (4.32)$$

4.1.4 Modeling initial film thickness

The initial film thickness is modeled using lubrication theory, as described by Haider [1994], and assumes the motion of vapor plug in the expansion phase would result in a thin liquid film along the tunnel walls. The liquid film thickness, δ_o , lubricated by the two menisci, each receding with velocity u_o in the circular tunnel of radius r_t is given by

$$\frac{\delta_o}{r_t} = 1.3375 Ca^{2/3} \quad (4.33)$$

where $Ca (= \mu u_o / \sigma)$ is the capillary number. The growth of the vapor region at the beginning of the expansion phase is heat diffusion controlled. Thus, the initial velocity u_o at the beginning of the expansion phase is obtained by equating the initial heat transfer to the plug to the latent heat corresponding to the vapor generation rate, resulting in (Haider, [1994])

$$u_o = \frac{1}{2} \left(\frac{dL}{dt} \right)_{t=0} = \frac{4k_l(T_w - T_{sat})}{\rho_v h_{fg} r_t} \sqrt{\frac{r_t}{2\delta_o}} \tan^{-1} \sqrt{\frac{r_t}{2\delta_o}} \quad (4.34)$$

The initial film thickness δ_0 is obtained by solving eq. 4.33 and eq. 4.34 iteratively till convergence.

4.1.5 Modeling external heat transfer

Haider and Webb [1997] developed a sub-model for external convection based on the model of Mikic and Rohsenow [1969] for boiling from a plain surface. Haider's model included a transient term to account for the convection in the wake of the departing bubble. The model assumes that the beginning of the bubble cycle is dominated by transient conduction, and the final part is dominated by micro-convection caused by the wake of the departing bubble and expresses the external heat flux as

$$Q_{ex}'' = 2\sqrt{\pi k_l \rho_l c_p f D_b^2 n_s \Delta T_{sup}} \left\{ 1 + \left(\frac{0.66\pi c}{Pr^{1/6}} \right)^2 \right\}^{1/2} \quad (4.35)$$

where the empirical constant of $c=6.42$, was curve fitted from the Chien and Webb [1998c] and Nakayama et al. [1980b] bubble formation data. Ramaswamy et al [2003] found a constant value for the empirical constant c resulted in significant over-prediction of the external heat flux at high wall superheats and replaced with a third order polynomial function of the wall superheat given by

$$c = a_0 + a_1(\Delta T_{sup}) + a_2(\Delta T_{sup})^2 + a_3(\Delta T_{sup})^3 \quad (4.36)$$

where the constants are $a_0=6.58$, $a_1=-1.1612 \text{ } ^\circ\text{C}$, $a_2=0.0782 \text{ } ^\circ\text{C}^2$ and $a_3=-0.0018 \text{ } ^\circ\text{C}^3$. The error is using eq. 4.35 and eq. 4.36 in predicting the data listed in Haider and Webb [1997] and Ramaswamy et al. [2002] was found within $\pm 40\%$ for all data points (Ramaswamy, [1999]).

4.1.6 Modeling nucleation site density

The nucleation site density in the present model is predicted through a correlation with the empirical constants backed out from the nucleation site density data reported in literature. The liquid-vapor plug dynamics inside the tunnel of structured surfaces that govern the nucleation site density depends on the geometric parameters and the wall superheat. The geometric factors that determine the total number of bubble generated are the pore diameter (D_p), tunnel radius (r_t) and the total surface pore density (N_s). The nucleation density correlation is obtained by curve fitting the FC-72 (Ramaswamy et al. [2002]) and R-123 (Chien and Webb, [1998]) experimental data resulting in

$$n_s = C(\Delta T)^{x_1}(N_s)^{x_2}(r_t)^{x_3}(D_p)^{x_4} \quad (4.37)$$

where the constants are

$$C = 1246.38, \quad x_1 = 0.912, \quad x_2 = 0.435, \quad x_3 = 0.762, \quad x_4 = -0.545$$

Figure 4.3 shows the prediction of the nucleation density, using the correlation in Eq. 4.37, to be within $\pm 30\%$ of the data reported in literature.

4.1.7 Prediction procedure

Based on the equations outlined, the steps in predicting the parameters of boiling from structured surfaces are as follows:

- (1) Calculate the bubble departure diameter (D) using Eqs. (4.1), (4.4), (4.5), (4.7), (4.10), (4.11) and (4.12).
- (2) Solve Eqs. (4.33) and (4.34) iteratively to get the initial film thickness (δ_0)

(3) Calculate the bubble frequency by solving Eq. 4.14, which can be expanded as

$$\int_0^{1/2f} (2Q_m + Q_f)_{\text{exp}} dt + \int_{1/2f}^{1/f} (2Q_m + Q_f)_{\text{con}} dt = \frac{\pi}{6} \rho_v h_{fg} D^3 \quad (4.38)$$

The first and second terms in Eq. (4.38) represent the latent heat transfer during the expansion and contraction phase respectively. The film heat transfer (Q_f) becomes zero on reaching the non-evaporating thickness (δ_{ne}).

(4) Calculate the nucleation site density by using Eq. (4.37).

(5) The total heat flux, which is the sum of the tunnel heat flux (Q_t) and the external heat flux (Q_{ex}), is obtained from Eqs. (4.14) and (4.35).

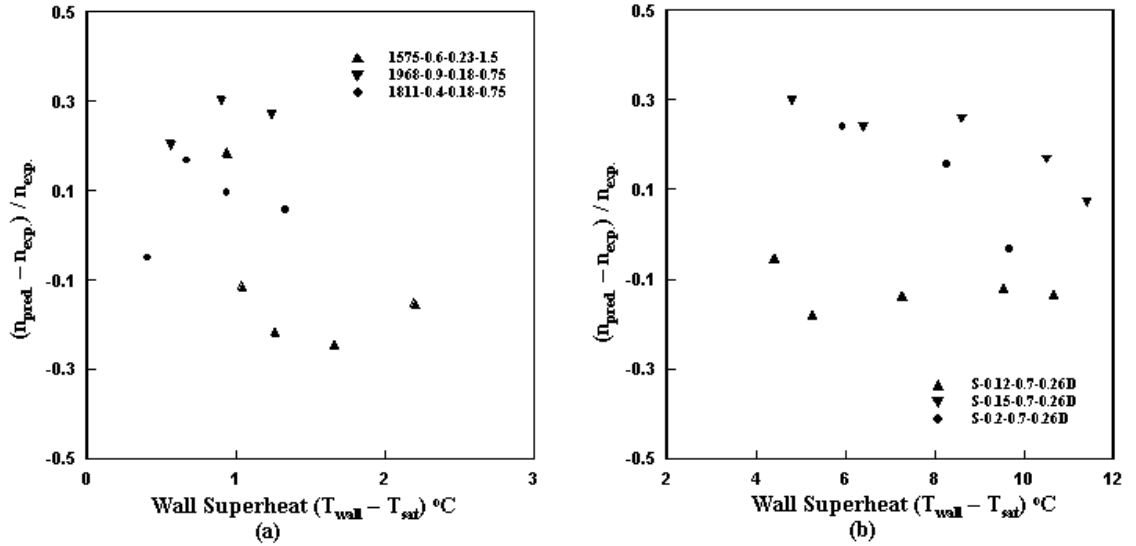


Figure 4.3: Comparison of experimental nucleation site density with those predicted using correlation in Eq. 4.37.

4.2 Results of Semi-Analytical Model

The semi-analytical model described in the previous section was used to predict the bubble departure diameter, bubble frequency, nucleation site density and the total

heat flux dissipated for boiling from enhanced surfaces and compared with experimental data reported in the literature. Table 4.1 briefly summarizes the geometric details of the various studies used in the validation of the semi-analytical model. The nomenclature used in identifying the studies is similar to those used by the investigators in reporting their results (Fig. 4.4), with H_t referring to the sub-surface tunnel height, D_p denoting the pore diameter and P_p representing the pore pitch. For example, Chien's structure 1968-0.9-0.18-0.75 refers to an enhancement structure with 1968 fins/m, 0.9 mm tunnel height, 0.18 mm pore diameter and 0.75 mm pore pitch. Similarly, Ramaswamy's structure S-0.2-1.0-0.26W refers to a structured surface in Silicon with 0.2 mm pore diameter, 1.0 mm pore pitch and 0.26 mm tunnel height. The last letter identifies the method used for making the enhancement structures, in this case 'W' signifying wet-etch process.

4.2.1 Prediction of departure diameter

A comparison of the predicted and experimental values for bubble departure diameter is shown in Fig. 4.5. The results show very good agreement between the predicted and experimental values with the absolute error being within $\pm 20\%$. The present model does not capture the observed decrease in departure diameter (Nakayama et al. [1980a], Chien and Webb [1998d]) with increase in wall superheat in the range 1-3 °C. Zuber [1963] suggested that for very low wall superheats, the bubble departure is a function of the buoyancy and surface tension forces only. Therefore, an increase in wall temperature causes a reduction in surface tension forces resulting in a decrease in the departure diameter. The present model does not account for temperature dependent

surface tension effects and hence fails to predict the trends in bubble departure variation at low wall superheats. However, as the wall superheat is increased further, dynamic forces start dominating the bubble growth and the variation in surface tension force with temperature becomes negligible.

Table 4.1: Geometrical details for the parametric studies in literature

Investigators (Nomenclature)	Fluid	Tunnel pitch (mm)	Tunnel height (mm)	Pore diameter (mm)	Pore pitch (mm)
	Water	0.5 - 0.6	0.5 - 0.62	0.08 - 0.2	0.6 - 0.72
Nakayama et al. (1980a) (Fins/m- H_f - d_p - P_p)	R - 11	0.55	0.4	0.04 - 0.15	0.7
	Liquid nitrogen	0.4	0.4 - 0.56	0.03 - 0.2	0.72
Chien (1996) (Fins/m- H_f - d_p - P_p)	R-11, R- 123 and R-22	0.5 - 0.72	0.5 - 1.5	0.12 - 0.28	0.75 - 0.3
Ramaswamy et al. (1999) (Material- d_p - P_p - H_f)	FC-72	0.5 - 1.0	0.26 - 0.55	0.09 - 0.32	0.5 - 1.0

4.2.2 Prediction of frequency

A comparison of the predicted values for frequency and experimentally observed values is shown in Fig. 4.6. The trends in variation of frequency with wall superheat are captured fairly accurately. The error in the prediction lies within a range of $\pm 35\%$. The model predicts the frequency to increase monotonically with increase in wall superheat values. However, the experimental values of Ramaswamy et al [2002] show a reduction in the frequency at intermediate wall superheats. This was explained

through the induced sweeping motion caused by the liquid return to the evaporator in their experimental set-up. The current model does not account for this phenomena resulting in large prediction errors at high wall superheats.

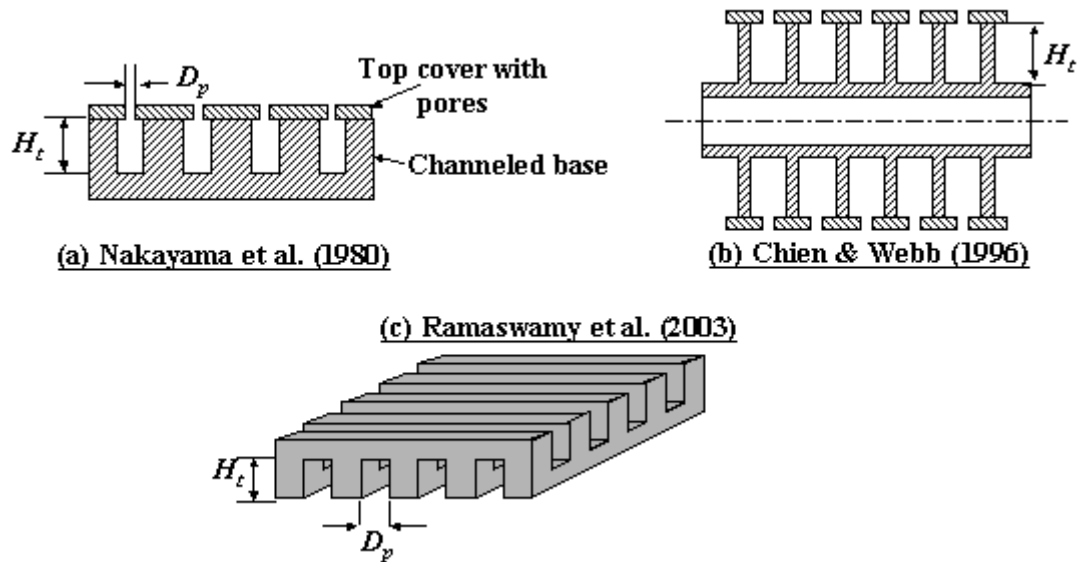


Figure 4.4: Schematic of the enhancement structures reported in literature used for validating the semi-analytical model. The geometric parameters of the structures are summarized in table 4.1.

4.2.3 Prediction of heat flux

A comparison of the predicted values to experimental results for structures used in Chien and Webb [1998d] and Nakayama et al. [1980a] is shown in Fig. 4.7a. The model predicts the heat flux variation with wall temperature within $\pm 40\%$. Fig 4.7b shows the predicted heat transfer coefficient values follow the trend observed in experiments. The heat transfer coefficient varies with heat flux to the power of 0.46, which implies that the heat flux varies with wall superheat to the power of 1.8. The exponent is higher than the value of 1.24 predicted for natural convection boiling but is

less than Rohsenow’s prediction for nucleate boiling where the heat flux varies to the cube of wall superheat.

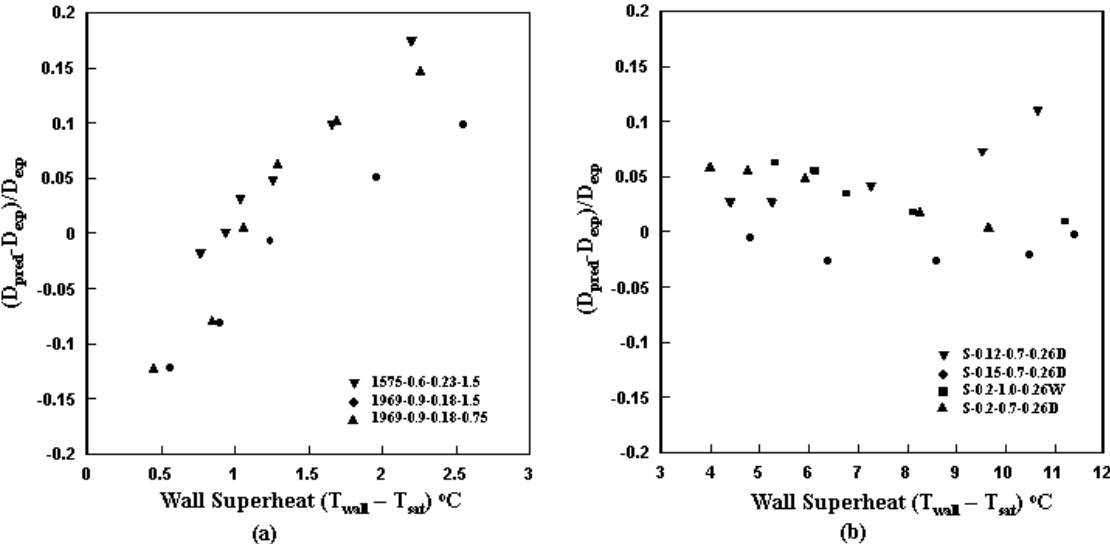


Figure 4.5: Comparison of bubble departure diameter – prediction vs. experiments.

Figures 4.8a and 4.8b compare the model prediction with the experimental data obtained using Ramaswamy et al.’s [2002] boiling enhancement structures with a pore size of 150 μm and 200 μm respectively. The results show that the prediction for these structures was fairly accurate. The maximum error in prediction for the 150 μm and 200 μm structure was within $\pm 30\%$. The prediction error increases with increase in wall superheat. The present model was developed primarily for the isolated bubble regime and becomes invalid when bubbles departing the surface coalesce vertically or laterally, accounting for the observed discrepancies at higher heat fluxes.

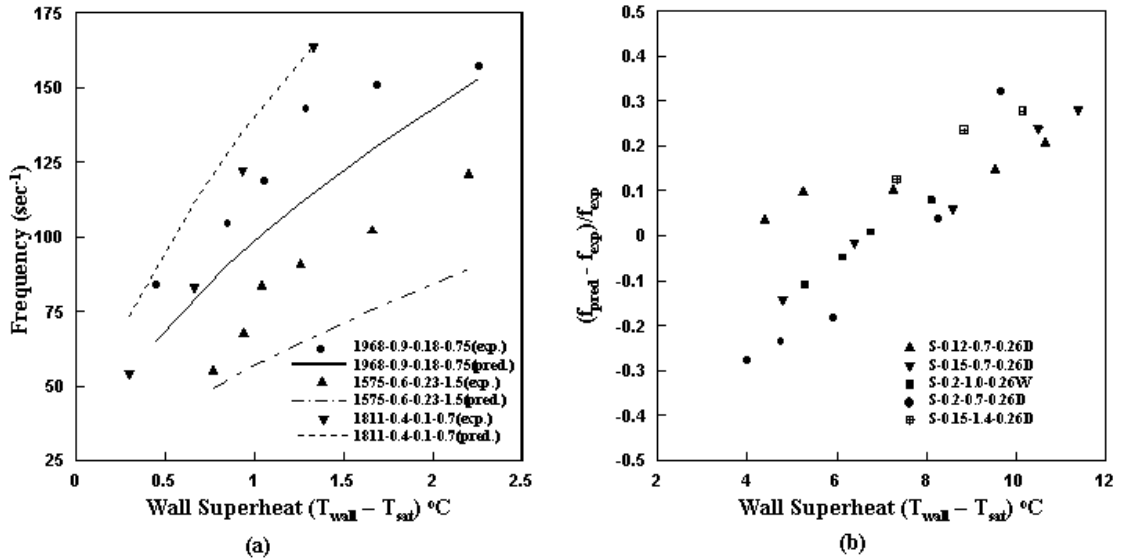


Figure 4.6: Comparison of frequency – prediction vs. experiments.

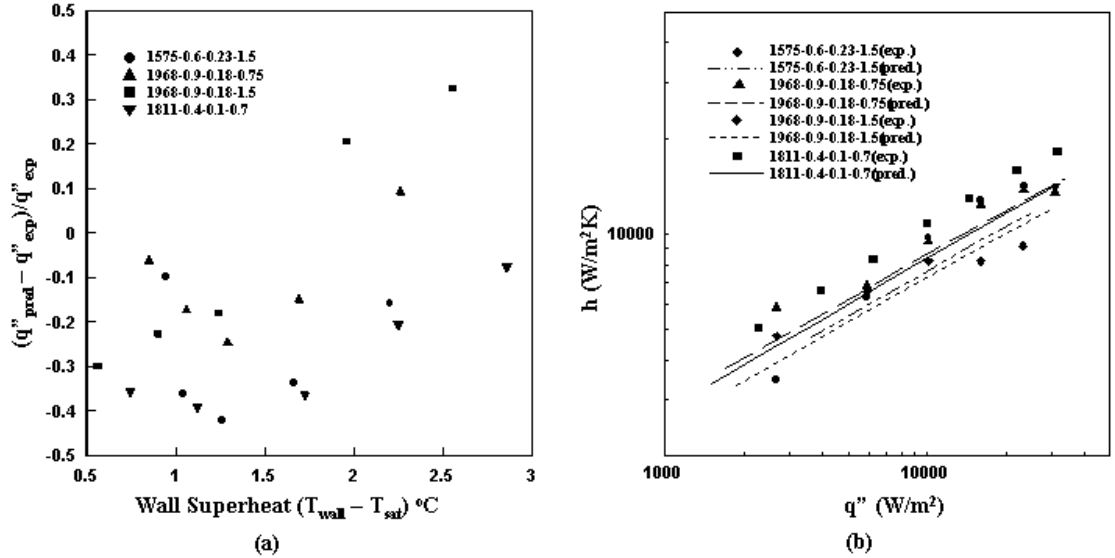


Figure 4.7: Comparison of prediction vs. experiments for Chien's and Nakayama's structures (a) heat flux (b) heat transfer coefficient.

4.2.4 Performance prediction of two-phase heat spreaders

The thermal performance of the two-phase spreaders was predicted using the above-developed semi-analytical model for boiling from enhanced surfaces. The semi-analytical model requires as input the liquid saturation temperature (T_{sat}), along with the geometry of the enhanced surface and the fluid properties. At steady state, the condenser walls of the spreader plate are assumed to be at T_{sat} . The saturation temperature is resolved iteratively through a conduction model of the external condenser wall with peripheral fins, by satisfying the energy balance for a given heat input and external boundary conditions. Experiments were carried out without any liquid in the spreader plate and the data was used in arriving at the convection heat transfer coefficients used in the model. The liquid saturation temperature thus obtained is used as an input to the semi-analytical model to predict the wall temperature (T_{wall}). Figure 4.9 shows a schematic of the algorithm used. Figure 4.10 compares the prediction from the spreader model with the data obtained from the forced convection experiments using the copper spreader plate. The model captures the trends in thermal performance of the two-phase spreader plate with the maximum error in prediction being 30%.

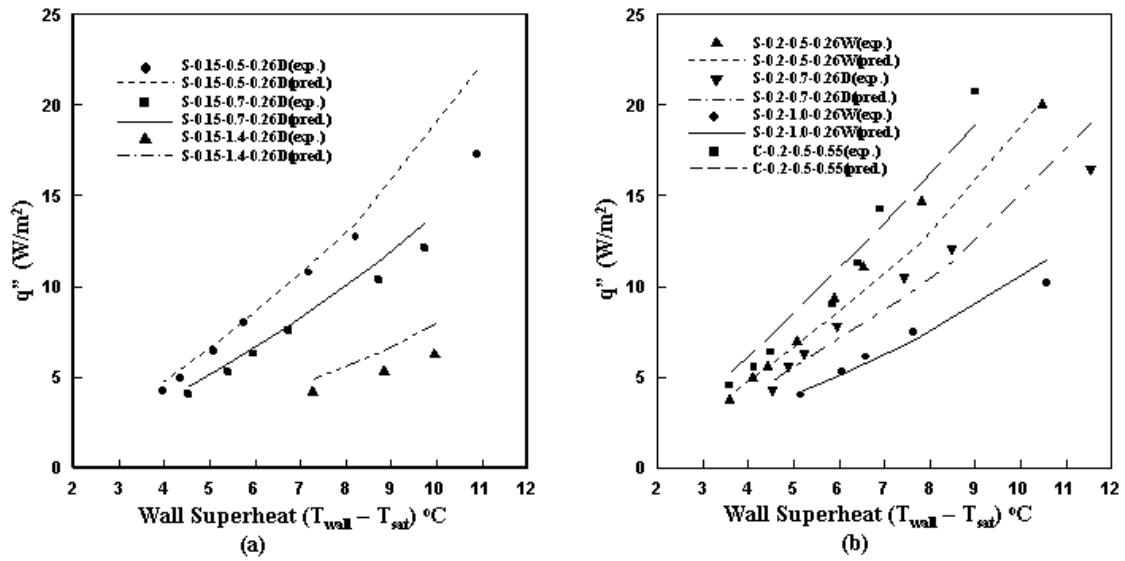


Figure 4.8: Comparison of heat flux variation with wall temperature for Ramaswamy's structures of pore size (a) $D_p=150 \mu\text{m}$ and (b) $D_p=200 \mu\text{m}$.

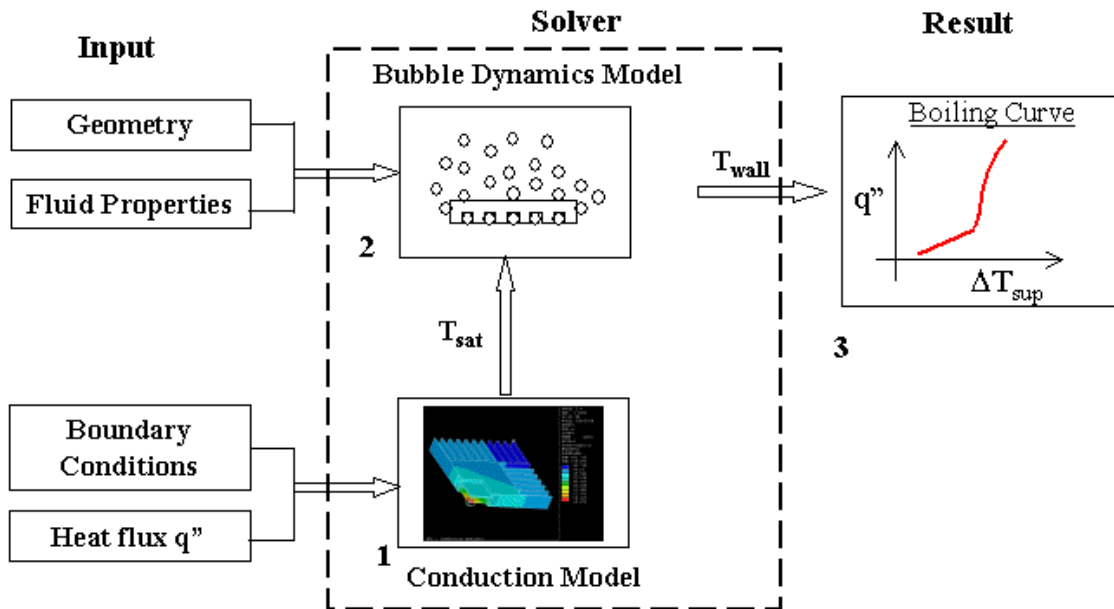


Figure 4.9: Algorithm for the two-phase spreader thermal performance model based on the semi-analytical model for enhanced boiling.

4.3 Summary and Conclusions

A semi-analytical model that predicts the bubble dynamics for boiling from structured surfaces with subsurface tunnels has been developed and validated against existing experimental data. The salient improvements over existing models and conclusions based on the predictions are,

- (1) Previously existing models of ‘suction-evaporation’ mode of boiling from enhanced surfaces have been developed on erroneous Hamaker constant values that are nearly 6-8 orders of magnitude higher than actual values. These models are very sensitive to the Hamaker constant and fail to predict correctly the observed bubble dynamics on using the correct value.
- (2) A modified model for ‘flooded’ mode boiling regime was developed with the inclusion of dynamic forces in the prediction of bubble departure diameter. The bubble departure predictions were within $\pm 20\%$. The error in frequency predictions was within $\pm 35\%$.
- (3) A correlation for nucleation site density was developed based on wall superheat and structure geometry properties.
- (4) The heat flux predictions were found to be within $\pm 30\%$ with the model capturing the trends fairly well for wall superheats less than $12\text{ }^{\circ}\text{C}$.
- (5) The boiling model was subsequently used in predicting the thermal performance of a novel two-phase heat spreader that employs enhancement structures in the evaporator section of the spreader plate.

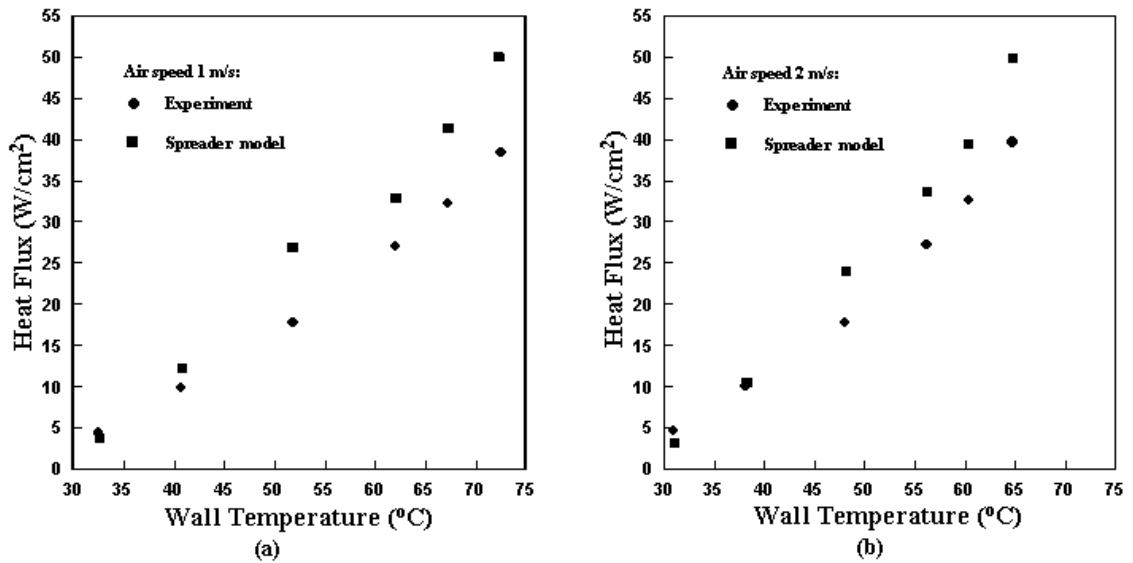


Figure 4.10: Thermal performance predictions of the forced air-cooled two-phase heat spreader (a) Air velocity of 1 m/s (b) Air velocity of 2 m/s.

The main objective of developing a semi-analytical model is to carry out optimization of the enhanced structure geometry. Experimental studies on the effect of enhanced geometry dimensions on the boiling performance (Chien and Webb [1998a], Ramasamy [1999]) show an increase in heat transfer with increase in pore diameter or pore density. An increase in pore diameter results in more liquid in the subsurface tunnels while an increase in the pore density causes greater bubble agitation and increased external heat flux. The above model can be used in arriving at an optimum design value of the pore diameter and pitch for maximum heat dissipation.

CHAPTER 5: NUMERICAL SIMULATION OF BOILING FROM ENHANCED STRUCTURES

Over the last two decades, computational methods have been developed for solving fluid flow problems with moving interfaces separating gas and liquid phases. Deshpande [1989] carried out numerical simulation of the bubble growth and collapse in a thermal ink jet print head through the volume of fluid method. Oguz and Prosperetti [1990] used the boundary integral method to study the cause of noise due to raindrops by computing the air and water flow with stiff surface tension effects. Boulton-Stone and Blake [1993] also used the boundary integral method to analyze the problem of rise and bursting of an air-bubble in water. Other examples of methods used to solve problems involving air bubbles in a free surface include boundary integral methods (Lundgren and Mansour, [1991]), front tracking methods (Unverdi and Tryggvason, [1992]), volume-of-fluid methods (Brackbill et al., [1992], Puckett et al. [1997]) and level-set methods (Sussman et al., [1994], [1998]).

The purpose of this study was to develop a numerical method for computing the bubble growth from an enhanced structure pore. The different phases are captured by the level set formulation with the velocity field computed using an approximate projection formulation (Almgren et al., [1996]) for variable density problems (Bell and Marcus, [1992]).

5.1 Projection Method

The design of an incompressible flow algorithm that maintains solution accuracy and simulation robustness in the presence of density variations presents challenges,

especially if the variations are discontinuous and topologically complex as those encountered during bubble growth in free liquid. The use of projection method with level set technique allows for the use of higher order upwinded methods for differencing the non-linear convective terms, thus providing a robust treatment of the convective terms at high Reynolds number.

Projection method is based on a discrete form of Hodge decomposition, which states that a vector field can be decomposed into the gradient of a scalar potential and a divergence free component, subject to some type of boundary condition. Chorin ([1968], 1969) developed a practical numerical method based on discrete form of the Hodge decomposition and the formulation is summarized below.

The continuity and momentum equations for the incompressible Navier-Stokes equations are given as

$$\nabla \cdot \vec{U} = 0 \quad (5.1)$$

$$\begin{aligned} \frac{\partial \vec{U}}{\partial t} + \vec{U} \cdot \nabla \vec{U} = & -\frac{\nabla p}{\rho(\phi)} + \frac{1}{\rho(\phi)} \nabla \cdot (2\mu(\phi)D) \\ & - \frac{1}{\rho(\phi)} \gamma \kappa(\phi) \nabla H(\phi) + \vec{F} \end{aligned} \quad (5.2)$$

where ϕ is the levelset function and D the deformation tensor.

The momentum equation becomes

$$\frac{\partial \vec{U}}{\partial t} + \frac{\nabla p}{\rho(\phi)} = V(\vec{U}, \phi) \quad (5.3)$$

where

$$\begin{aligned} V(\vec{U}, \phi) = & -\vec{U} \cdot \nabla \vec{U} + \frac{1}{\rho(\phi)} \nabla \cdot (2\mu(\phi)D) \\ & - \frac{1}{\rho(\phi)} \gamma \kappa(\phi) \nabla H(\phi) + \vec{F} \end{aligned} \quad (5.4)$$

Divergence of Eq (5.3) coupled with $\frac{\partial(\nabla \cdot \vec{U})}{\partial t} = 0$ results in an equation for

pressure,

$$\nabla \cdot \frac{\nabla p}{\rho(\phi)} = \nabla \cdot V(\vec{U}, \phi) \quad (5.5)$$

Eq. (5.5) is solved for pressure and used to update \vec{U} through

$$\frac{\partial \vec{U}}{\partial t} = V(\vec{U}, \phi) - \frac{\nabla p}{\rho(\phi)} \quad (5.6)$$

Defining the projection operator P as $\frac{\partial \vec{U}}{\partial t} \equiv P(V)$, one obtains

$$\frac{\nabla p}{\rho(\phi)} = (I - P)(V) \quad (5.7)$$

In the current numerical study, the algorithm used to advance the solution from time t^n to t^{n+1} ($t^n + \Delta t$) follows the general approach used by Almgren et al. [1996]. A uniform mesh spacing was used with the widths Δx and Δy indexed by i and j respectively. At the beginning of the time step, the numerical solution, except for pressure, represents the flow at time t^n at cell centers. The solution for pressure,

$p_{i+1/2, j+1/2}^{n-1/2}$, represents the pressure at the previous half time step, $t^{n-1/2}$, on cell corners.

The numerical method is a second order projection method (Bell et al., [1989]) with the overall approach being that of a fractional step scheme. In the first step (predictor step), values of U , denoted by $U^{n+1/2}$ ($u^{n+1/2}$, $v^{n+1/2}$), are computed. The velocity values do not necessarily satisfy the divergence constraint at t^{n+1} . In the second step (projection

step), the divergence constraint is imposed on the velocity via a node-based projection

resulting in $U_{i,j}^{n+1}$ and $p_{i+\frac{1}{2},j+\frac{1}{2}}^{n+\frac{1}{2}}$.

5.1.1 Predictor step

The predictor step is used to construct the advective update terms by first extrapolating the normal velocities to cell faces at $t^{n+\frac{1}{2}}$ using a second order Taylor series expansion in space and time. The time derivative is replaced using Eq. 5.2 and results in

$$\begin{aligned} \bar{U}_{i+1/2,j}^{n+1/2,L} = \bar{U}_{i,j}^n &+ \left(\frac{\Delta x}{2} - \frac{u_{i,j}^n \Delta t}{2} \right) \left(\frac{\Delta_x \bar{U}_{i,j}^n}{\Delta x} \right) - \frac{\Delta t}{2} \left(\frac{v \partial \hat{U}}{\partial y} \right)_{i,j} \\ &+ \frac{\Delta t}{2} \left(-\frac{G p_{i,j}^{n-1/2}}{\rho_{i,j}^n} + \frac{L_{i,j}^n}{\rho_{i,j}^n} - \frac{M_{i,j}^n}{\rho_{i,j}^n} + \bar{F} \right) \end{aligned} \quad (5.8a)$$

$$\begin{aligned} \bar{U}_{i+1/2,j}^{n+1/2,R} = \bar{U}_{i+1,j}^n &- \left(\frac{\Delta x}{2} + \frac{u_{i+1,j}^n \Delta t}{2} \right) \left(\frac{\Delta_x \bar{U}_{i+1,j}^n}{\Delta x} \right) - \frac{\Delta t}{2} \left(\frac{v \partial \hat{U}}{\partial y} \right)_{i+1,j} \\ &+ \frac{\Delta t}{2} \left(-\frac{G p_{i+1,j}^{n-1/2}}{\rho_{i+1,j}^n} + \frac{L_{i+1,j}^n}{\rho_{i+1,j}^n} - \frac{M_{i+1,j}^n}{\rho_{i+1,j}^n} + \bar{F} \right) \end{aligned} \quad (5.8b)$$

where G is the discretization of the gradient operator. The transverse derivative terms $\frac{v \partial \hat{U}}{\partial y}$ are handled using upwind discretization as follows

$$\begin{aligned} \left. \frac{\partial \hat{U}}{\partial y} \right|_{i,j} &= \frac{\bar{U}_{i,j} - \bar{U}_{i,j-1}}{\Delta y} + \frac{1}{2} \left(1 - \frac{\Delta t v_{i,j}}{\Delta y} \right) \frac{(\Delta_y \bar{U})_{i,j} - (\Delta_y \bar{U})_{i,j-1}}{\Delta y} \text{ if } v_{i,j} \geq 0 \\ \left. \frac{\partial \hat{U}}{\partial y} \right|_{i,j} &= \frac{\bar{U}_{i,j+1} - \bar{U}_{i,j}}{\Delta y} - \frac{1}{2} \left(1 + \frac{\Delta t v_{i,j}}{\Delta y} \right) \frac{(\Delta_y \bar{U})_{i,j+1} - (\Delta_y \bar{U})_{i,j}}{\Delta y} \text{ if } v_{i,j} \leq 0 \end{aligned} \quad (5.9)$$

The normal velocity at each face is then determined by an upwinding procedure based on the states predicted from the cell centers on either side, as described in detail by Almgren et al. [1996],

$$\hat{U}_{i+1/2,j} = \begin{cases} \hat{U}^{L,n+1/2} & \text{if } \hat{U}^{L,n+1/2} > 0 \text{ and } \hat{U}^{L,n+1/2} + \hat{U}^{R,n+1/2} > 0 \\ 0 & \text{if } \hat{U}^{L,n+1/2} \leq 0, \hat{U}^{R,n+1/2} \geq 0 \text{ or } \hat{U}^{L,n+1/2} + \hat{U}^{R,n+1/2} = 0 \\ \hat{U}^{R,n+1/2} & \text{if } \hat{U}^{R,n+1/2} < 0 \text{ and } \hat{U}^{L,n+1/2} + \hat{U}^{R,n+1/2} < 0 \end{cases} \quad (5.10)$$

The normal velocities on cell faces are now centered in time and second order accurate, but do not, in general, satisfy the divergence constraint. The MAC projection (Lai et al., [1993]) is applied to enforce the divergence constraint. The equation

$$D^{MAC} \left(\frac{1}{\rho} G^{MAC} p^{MAC} \right) = D^{MAC} (\vec{U}^{n+1/2}) - \left(S + \frac{\Delta t}{2} \frac{\partial S^n}{\partial t} \right) \quad (5.11)$$

is solved for p^{MAC} , where

$$D^{MAC} (\vec{U}^{n+1/2}) = \frac{u_{i+1/2,j}^{n+1/2} - u_{i-1/2,j}^{n+1/2}}{\Delta x} + \frac{v_{i,j+1/2}^{n+1/2} - v_{i,j-1/2}^{n+1/2}}{\Delta y} \quad (5.12)$$

and $G^{MAC} = -(D^{MAC})^T$ so that

$$\left(G_x^{MAC} p^{MAC} \right)_{i+1/2,j} = \frac{p_{i+1,j}^{MAC} - p_{i,j}^{MAC}}{\Delta x} \quad (5.13)$$

S refers to the source term in the mass conservation equation. Once p^{MAC} is obtained, the velocities are updated by

$$u_{i+1/2,j}^{ADV} = u_{i+1/2,j}^{n+1/2} - \frac{1}{\rho_{i+1/2,j}^n} \left(G_x^{MAC} p^{MAC} \right)_{i+1/2,j} \quad (5.14a)$$

$$v_{i,j+1/2}^{ADV} = v_{i,j+1/2}^{n+1/2} - \frac{1}{\rho_{i,j+1/2}^n} \left(G_y^{MAC} p^{MAC} \right)_{i,j+1/2} \quad (5.14b)$$

The time centered values $U^{n+1/2}$ at each face are determined by upwinding, as follows:

$$\bar{U}_{i+1/2,j}^{n+1/2} = \begin{cases} \bar{U}_{i+1/2,j}^{n+1/2,L} & \text{if } u_{i+1/2,j}^{ADV} > 0 \\ \bar{U}_{i+1/2,j}^{n+1/2,R} & \text{if } u_{i+1/2,j}^{ADV} < 0 \\ 1/2(\bar{U}_{i+1/2,j}^{n+1/2,L} + \bar{U}_{i+1/2,j}^{n+1/2,R}) & \text{if } u_{i+1/2,j}^{ADV} = 0 \end{cases} \quad (5.15)$$

Similar procedure is adopted for other faces. An approximation for the non-linear convective term $[\bar{U} \cdot \nabla \bar{U}]^{n+1/2}$ is defined by

$$\begin{aligned} [\bar{U} \cdot \nabla \bar{U}]_{i,j}^{n+1/2} &= \frac{1}{\Delta x} (\bar{U}_{i+1/2,j}^{n+1/2} u_{i+1/2,j}^{ADV} - \bar{U}_{i-1/2,j}^{n+1/2} u_{i-1/2,j}^{ADV}) \\ &+ \frac{1}{\Delta y} (\bar{U}_{i,j+1/2}^{n+1/2} v_{i,j+1/2}^{ADV} - \bar{U}_{i,j-1/2}^{n+1/2} v_{i,j-1/2}^{ADV}) \end{aligned} \quad (5.16)$$

On obtaining the convective terms, a viscous solve is performed to compute U^* based on

$$\frac{\bar{U}^* - \bar{U}^n}{\Delta t} = -[\bar{U} \cdot \nabla \bar{U}]^{n+1/2} - \frac{Gp^{n-1/2}}{\rho^{n+1/2}} + \frac{L^* + L^n}{2\rho^{n+1/2}} - \frac{M^{n+1/2}}{\rho^{n+1/2}} + \vec{F} \quad (5.17)$$

where L is the discrete approximation to viscous stresses with L^n based on velocities at n and L^* based on the intermediate field. This makes this step semi-implicit. M is the surface tension body force term and G is the gradient operator. Eq 5.17 when discretized gives a coupled parabolic solve for U^* .

5.1.2 Projection step

In the projection step, a vector field decomposition is applied to $(\bar{U}^* - \bar{U}^n) / \Delta t$ to obtain an update to the velocity field $(\bar{U}^{n+1} - \bar{U}^n) / \Delta t$, and an update for the pressure. The projection results in

$$\frac{1}{\rho^{n+1/2}} \nabla p^{n+1/2} = \frac{1}{\rho^{n+1/2}} \nabla p^{n+1/2} + (\mathbf{I} - \wp) \left(\frac{\vec{U}^* - \vec{U}^n}{\Delta t} \right) \quad (5.18)$$

where \wp represents the projection operator. Eq. 5.18 is similar to Eq. 5.7 with the vector field projected being an approximation to U_t . The projection is solved for p by evaluating

$$L_\rho^{n+1/2} p = D \left(\frac{\vec{U}^* - \vec{U}^n}{\Delta t} \right) - \frac{S^{n+1} - S^n}{\Delta t} \quad (5.19)$$

where D is the discrete nodal approximation to the divergence operator and $L_\rho^{n+1/2} p$ is a second order accurate nodal approximation to $\nabla \cdot \left(\frac{1}{\rho^{n+1/2}} \nabla p \right)$. The

updates for velocity and pressure are subsequently obtained from

$$\frac{\vec{U}^{n+1} - \vec{U}^{n+1}}{\Delta t} = \frac{\vec{U}^* - \vec{U}^{n+1}}{\Delta t} - \frac{1}{\rho^{n+1/2}} \bar{G} p \quad (5.20a)$$

$$p^{n+1/2} = p^{n-1/2} + p \quad (5.20b)$$

The problem specification requires values for U at time $t^0 = 0$ and values for the pressure p at time $t^{-1/2}$ for solving Eq. 5.17. The value of $p^{-1/2}$ is obtained iteratively with the initial velocity field projected to ensure that the divergence constraint is satisfied at $t=0$. In the first iteration, $p^{-1/2}$ is taken to be zero. At the end of each iteration, $p^{-1/2}$ is defined to be equal to the pressure update, $p^{1/2}$, with the velocity update, U^l , discarded and the iterations are carried out till convergence.

5.1.3 Validation of flow solver

The lid-driven cavity has been used extensively for validation of flow solvers in literature. The flow develops inside a closed square cavity, $\Omega=[0,1] \times [0,1]$, with the top boundary moving at a constant speed. The boundary conditions employed were,

$$U(0,y) = U(1,y) = U(x,0) = 0; u(x,1) = 1 \text{ m/s}; v(x,1) = 0$$

with homogeneous Neumann boundary condition for pressure. Figure 5.1 shows the velocity profiles obtained using a 16 x 16 grid. Figure 5.2 plots the normalized horizontal and vertical components of velocity along geometric centerlines. The velocity predictions are nearly identical and correspond reasonably with results from Ghia et al. [1982] at the Reynolds number of $Re = 400$. Table 5.1 contains a convergence study of L^2 error, where the error is measured as

$$\|E\|_2 = \frac{1}{h_x h_y} \sum \sqrt{\sum (x - x_{actual})^2} \quad (5.21)$$

The error analysis was carried out with respect to the velocity field obtained from a fine grid of 200 x 200 that was assumed to be exact. Table 5.1 shows that relative change in velocity prediction reduces exponentially with mesh refinement and second and higher order accuracy is achieved for both u and v velocities.

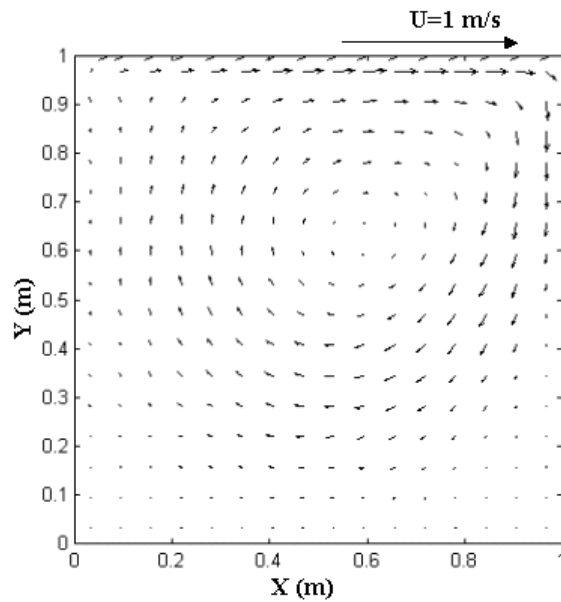


Figure 5.1: Velocity vectors obtained for a $Re=400$ lid-driven cavity flow on a 16×16 grid.

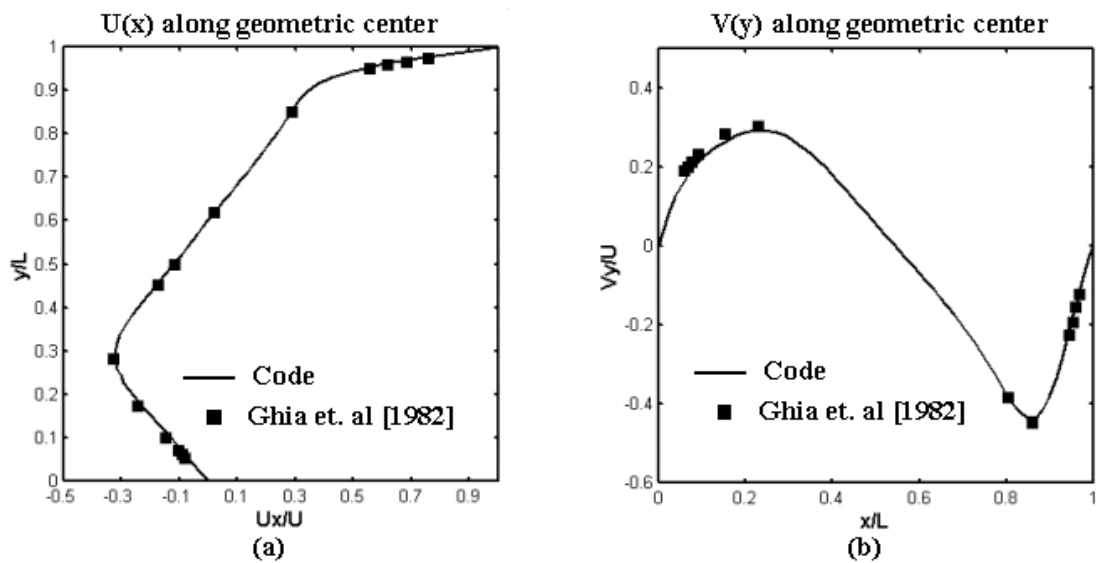


Figure 5.2: 2D cavity velocity profile comparison with Ghia et al. [1982] for $Re = 400$. (a) X component of velocity as a function of y through center. (b) Y component of velocity as a function of x through center.

Table 5.1: Convergence study for lid-driven cavity flow

Grid	U Velocity		V Velocity	
	Error	Order	Error	Order
16 x 16	2.3 E-03	N/A	2.6 E-03	N/A
32 x 32	4.4 E-04	2.38	4.4 E-04	2.54
64 x 64	4.9 E-05	3.17	5.4 E-04	3.04

5.2 Level Set Formulation

An interface Γ enclosing Ω^c in a given region Ω can be represented by a function ϕ defined over the complete region with different values inside and outside Ω^c (Fig. 5.3). In the level set formulation introduced by Osher and Sethian [1988], the interface is represented as the zero level set of ϕ with the boundary defined as

$$\Gamma = \{\bar{x} \in \Omega \mid \phi(\bar{x}, t) = 0\} \quad (5.22)$$

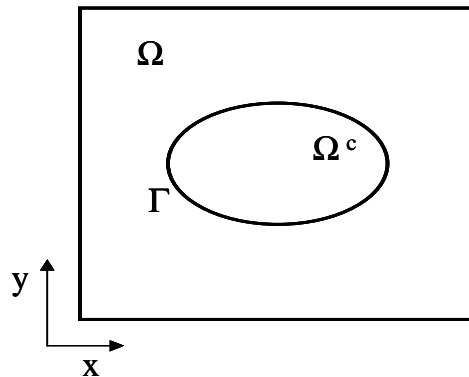


Figure 5.3: Interface Γ enclosing Ω^c in a region Ω . Interface Γ is represented by zero level set.

The level set function at any given point is taken as the signed shortest distance from the interface with opposite signs inside and outside the enclosed region Ω^c . The level set evolution for a velocity field $\vec{u}(\vec{x}, t)$ is governed by

$$\frac{\partial \phi}{\partial t} + \vec{u} \cdot \nabla \phi = 0 \quad (5.23)$$

The above equation accurately moves the zero level set according to the velocity field $\vec{u}(\vec{x}, t)$ even through merging and breaking of the fluid mass. With this definition, the level set function is continuous across interface but can develop faceted structure across sharp corners. Maintaining the level set function as a smooth distance function ensures that the interface has a thickness fixed in time.

Even though ϕ is initialized as signed distance from the front, under the evolution of the advection equation 5.23, it does not necessarily remain one. This problem is overcome by solving the following partial differential equation (Sussman et al. [1994])

$$\frac{\partial \phi}{\partial t} = \text{sign}(\phi_0)(1 - |\nabla \phi|) \quad (5.24)$$

with initial conditions $\phi(x, 0) = \phi_0(x)$ where

$$\text{sign}(\phi) = \begin{cases} -1 & \text{if } \phi < 0 \\ 0 & \text{if } \phi = 0 \\ 1 & \text{if } \phi > 0 \end{cases} \quad (5.25)$$

The above equation ensures that a given level set function is reinitialized to a distance function without changing its zero level set. Though equation 5.24 ensures that the zero level set remains unchanged during re-initialization, numerical discretization of Eq. 5.24 does not preserve this property in general, resulting in a change in the position

of the zero level set of ϕ . This poses a problem for applications involving incompressible flow with stiff surface tension effects found at small length scales. In such cases, the time-step for the advection computation would be quite small. As a result, the re-distance scheme would be called often, even though the interface has not advected very far and an inaccurate re-distancing algorithm could obscure the actual flow.

Sussman et al. [1998] have constructed a highly accurate method to prevent the straying of zero level set during re-distancing. The method employs a constraint in each cell of the computational domain to preserve the initial volume occupied by each phase. Spatial discretization was done with third order essentially non-oscillatory (ENO) schemes developed for hyperbolic conservation laws in conjunction with third order Runge-Kutta time stepping.

5.2.1 Level set validation

The levelset advection and redistancing formulation was tested for “Zalesak’s problem” (Zalesak [1979]), which involves rotation of a notched disk in a constant vorticity velocity field. The initial data is a slotted circle centered at (50,75) in a 100 x 100 domain size with a radius of 15, a width of 5 and a slot length of 25. The constant vorticity field is given by

$$u_o = (\pi/314) (50-y); v_o = (\pi/314) (x-50);$$

Figure 5.4 plots a zoomed image of the 200 x 200 grid results after one full revolution, overlaid with the expected solution. Very good agreement between the

predicted results and the actual solution is seen. Though the sharp corners of the notch become diffuse, fluctuation of the total area enclosed by the disk is less than 0.5 %.

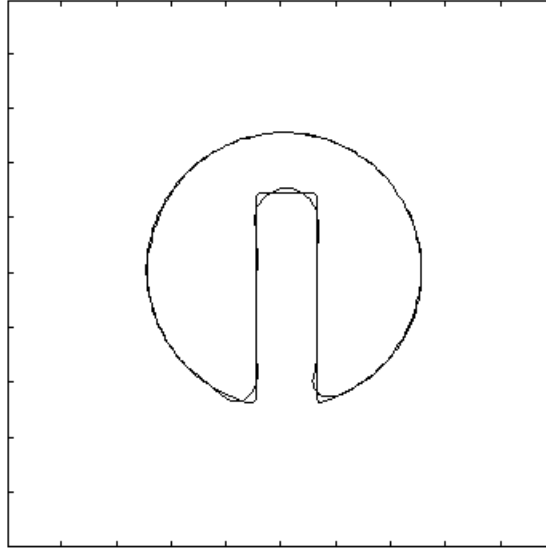


Figure 5.4: Zoomed comparison of a notched disc (Zalesak’s problem) that has been rotated one revolution about the center of the domain.

5.3 Numerical Analysis

The bubble growth from a surface pore of an enhanced surface was studied based on a second-order accurate projection method coupled with levelset formulation with the computational domain ($x_{max} = 1.0$ mm, $y_{max} = 1.5$ mm) chosen as shown in Fig. 5.5. The bubble diameter at the beginning of the computation ($t=0$) was assumed to be equal to the pore diameter. This corresponds to the situation where the vapor pressure matches the surface tension force on the pore (Fig. 4.1c). The flows were taken to be two-dimensional and laminar and the fluid properties including density, viscosity and

thermal conductivity were assumed to be constant in each phase. The thermo-physical properties were smoothed using level set function as

$$\lambda = (1 - H(\phi))\lambda_l + H(\phi)\lambda_g \quad (5.26)$$

where λ stands for density and viscosity with subscripts l and g referring to liquid and vapor respectively. $H(\phi)$ is the smoothed heaviside function and is given as

$$H(\phi) = \begin{cases} 0 & \text{if } \phi < \varepsilon \\ \frac{1}{2} \left[1 + \frac{\phi}{\varepsilon} + \frac{1}{\pi} \sin\left(\frac{\pi\phi}{\varepsilon}\right) \right] & \text{if } |\phi| < \varepsilon \\ 1 & \text{if } \phi > \varepsilon \end{cases} \quad (5.27)$$

With the above definition of the heaviside function, the interface was given a constant artificial thickness of 2ε for smooth transition. The interface thickness parameter, ε , was fixed as 1.5 times the mesh size.

The boundary conditions used in this study were as follows (Fig. 5.5)

At the wall ($y = 0$): $u = v = 0$;

At the symmetry planes: $u = v_x = 0$;

At the top of computational domain (free surface): $u_y = v_y = 0$;

The time step, Δt , is determined by restrictions due to CFL condition, gravity, viscosity and surface tension (Sussman et al. [1994]; Brackbill and Kothe [1992]) and is computed as

$$\Delta t^{n+1} = \frac{1}{2} \min \left[\frac{2\Delta x}{|\nabla p_{i,j} - F_{i,j}|}, \frac{\Delta x}{|u_{i,j}^n|}, \frac{\Delta y}{|v_{i,j}^n|}, \sqrt{\frac{(\rho_l + \rho_v)\Delta x^3}{8\pi\sigma}}, \frac{3\rho\Delta x^2}{14\mu} \right] \quad (5.28)$$

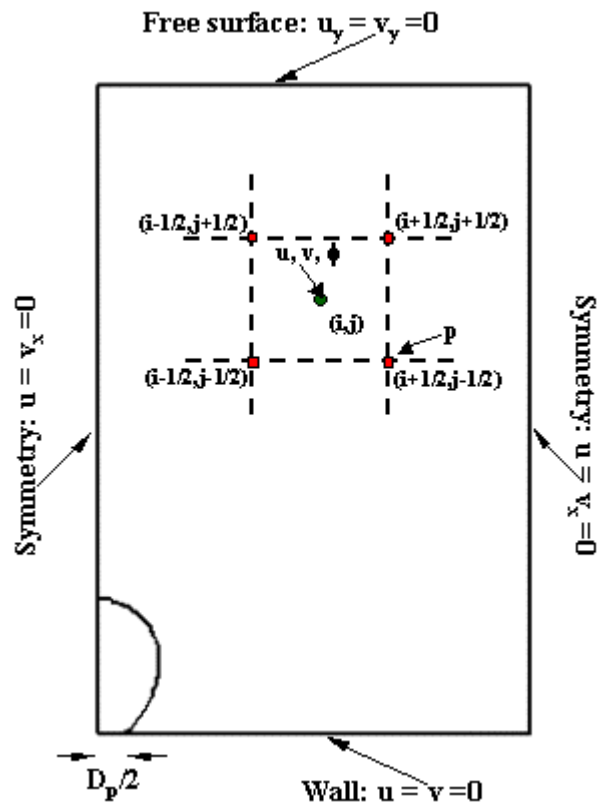


Figure 5.5: Computational grid with boundary conditions.

Son et al. [1999] simulated the growth and departure of a bubble from a horizontal surface by capturing the liquid-vapor interface using level set. The formulation was modified to include the influence of phase change at the liquid-vapor interface. Cooper and Lloyd [1969] confirmed experimentally the existence of micro layer underneath a bubble through the observation of fluctuations in the heater surface temperature. Though the existence of micro layer is well established, investigators have shown the contribution of micro layer in nucleate boiling heat transfer to be insignificant (Judd and Hwang, [1976]; Del Valle and Kenning, [1985]; Paul et al.,

[1992]). Hence, the effect of micro layer evaporation has been neglected for bubble growth in the current study.

The bubble growth mechanism from structured surface is different from that on a plain surface. The bubble growth from structured surfaces is inertia controlled with the vapor mainly supplied from the sub-surface tunnels. For inertia controlled growth, Mikic and Rosenhow [1969] assumed the growth of the bubble is controlled by the increasing vapor pressure of the vapor inside the bubble, and balanced by the inertia resistance and surface tension on the liquid-vapor interface. For a two-dimensional cylindrical bubble, the growth is given by

$$\left(\frac{dR}{dt}\right)^2 = \frac{b}{\rho_l} \left(P_v - P_s - \frac{\sigma}{R}\right) \quad (5.28)$$

where R is the instantaneous bubble diameter. The constant b was evaluated to be $\pi/7$ for a spherical bubble growing attached to a surface. The above constant is assumed to hold good for the growth of a cylindrical bubble (2D) for lack of additional data. Using the Clausius-Clapeyron equation to relate the pressure difference ($P_v - P_s$) to the corresponding temperature difference, Chien and Webb [1998] modified Eq. 5.28 to

$$\left(\frac{dR}{dt}\right) = \left(\frac{\pi h_{fg} \rho_v \Delta T_{ws}}{7 \rho_l T_s}\right)^{1/2} C_{tg} \left(\frac{D - D_p}{D + D_p}\right)^{1/2} \quad (5.29)$$

where C_{tg} was defined as a dimensionless empirical constant, which represents the slope of vapor superheat vs. a reference wall temperature (refer to Eq. 4.3).

The bubble departure diameter prediction in the semi-analytical model (Sec. 4.1.1) assumes the bubble remains attached to the surface pore during growth (Fig. 5.5).

The instantaneous rate of change in bubble area (2D) is given by

$$\frac{dA}{dt} = \left\{ \pi D + \frac{DD_p}{\sqrt{D^2 - D_p^2}} - D \sin^{-1} \left(\frac{D_p}{D} \right) \right\} \left(\frac{dR}{dt} \right) \quad (5.30)$$

The supply of vapor from the sub-surface tunnels is captured through a source term in the mass conservation equation (Eq. 5.1) for the region immediately adjoining the pore cavity with the formulation of the source term given by

$$S = \frac{dA/dt}{\Delta y D_p} \quad (5.31)$$

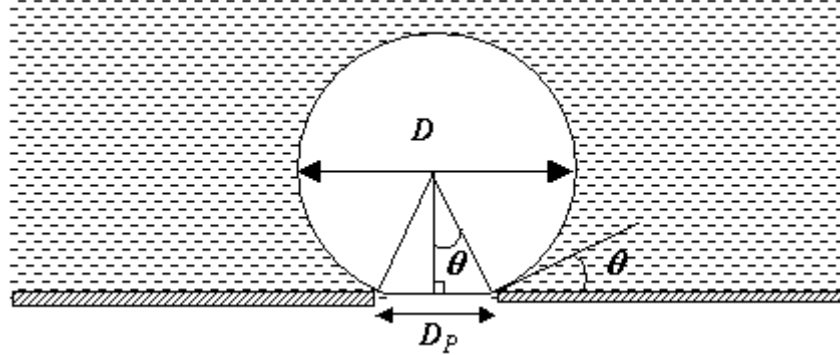


Figure 5.6: Envisioned bubble growth from a surface pore of an enhanced structure.

5.4 Solution Algorithm

The numerical procedure is summarized as:

- 1) Compute the source term for the mass conservation equation by evaluating Eq. 5.31. The vapor mass at the end of each iteration is used for computing the

radius of an equivalent cylindrical-arc surface that remains attached to the pore (Fig. 5.6). Subsequently, Eqs. 5.29 and 5.30 are evaluated to obtain the source term.

- 2) Predict the edge-based velocities using predictor-corrector scheme. Compute face centered velocities by extrapolation from cell centers and decide between the two states at each face by upwinding using U^{ADV}
- 3) Advect level set function with the edge velocities obtained from step 1 to get $\phi^{n+1}_{i,j}$. Level set function at $n+1/2$ level can be approximated by

$$\phi_{i,j}^{n+1/2} = \frac{1}{2}(\phi_{i,j}^{n+1} + \phi_{i,j}^n) \quad (5.32)$$

- 4) Solve the semi-implicit viscous equation (Eq. 5.17) for the intermediate velocity U^* .
- 5) Solve for the approximate projection of U_i (Eq. 5.19) resulting in updates for the velocity and pressure (Eq. 5.20).
- 6) Repeat steps 1-5 till bubble departs.

5.5 Numerical Simulation Results

The nucleate boiling computations were carried out for a liquid vapor density of 1000:1 with the viscosity of the liquid and the vapor assumed to be 10^{-5} Ns/m². The latent heat of vaporization (h_{fg}) was assumed to be 100 KJ/kg. To select an appropriate mesh size, convergence for grid resolutions was tested with mesh points of 50 x 75 and 100 x 150. The bubble shape at departure for the two grids showed insignificant

difference. Therefore, all computations are performed on a 50 x 75 grid to save on computational time without loss of accuracy.

Figure 5.7 shows the bubble growth pattern during one cycle for a wall superheat (ΔT) of 3 K. Since boiling from structured surfaces is a cyclic process, the computations should be carried out over several cycles to establish the flow field within the liquid. Unfortunately, the physics of vapor / liquid flow through the pore openings into the sub-surface tunnels is not clearly understood. Hence in the current study, solutions are carried out with the fluid at rest at the start of the computations and the computation is stopped once the bubble detaches from the surface. Visualization studies by Chien [1996] and Ramaswamy [1999] found the departing bubble from structured surfaces to be attached to the surface pore till detachment. To satisfy the above condition, a constraint is imposed for evaluation of the level set function at the wall,

$$\begin{aligned} \phi &< 0 \text{ for } x < \frac{D_p}{2} \\ &= 0 \text{ for } x = \frac{D_p}{2} \end{aligned} \quad (5.33)$$

It is seen from Figure 5.7 that during the early period of bubble growth, the influx of vapor from the sub-surface tunnels causes the vapor-liquid interface to expand radially outwards. However, the geometric constraint (Eq. 5.33) restricts the horizontal movement of the bubble base. The non-uniform bubble motion induces a clockwise vortex in the liquid layer. When liquid vortex becomes stronger with increase in bubble diameter, the bubble moves inwards resulting in necking and subsequent departure. The small vapor portion left after the bubble departure gets sucked into the sub-surface tunnel and serves as a nucleus for the next bubble.

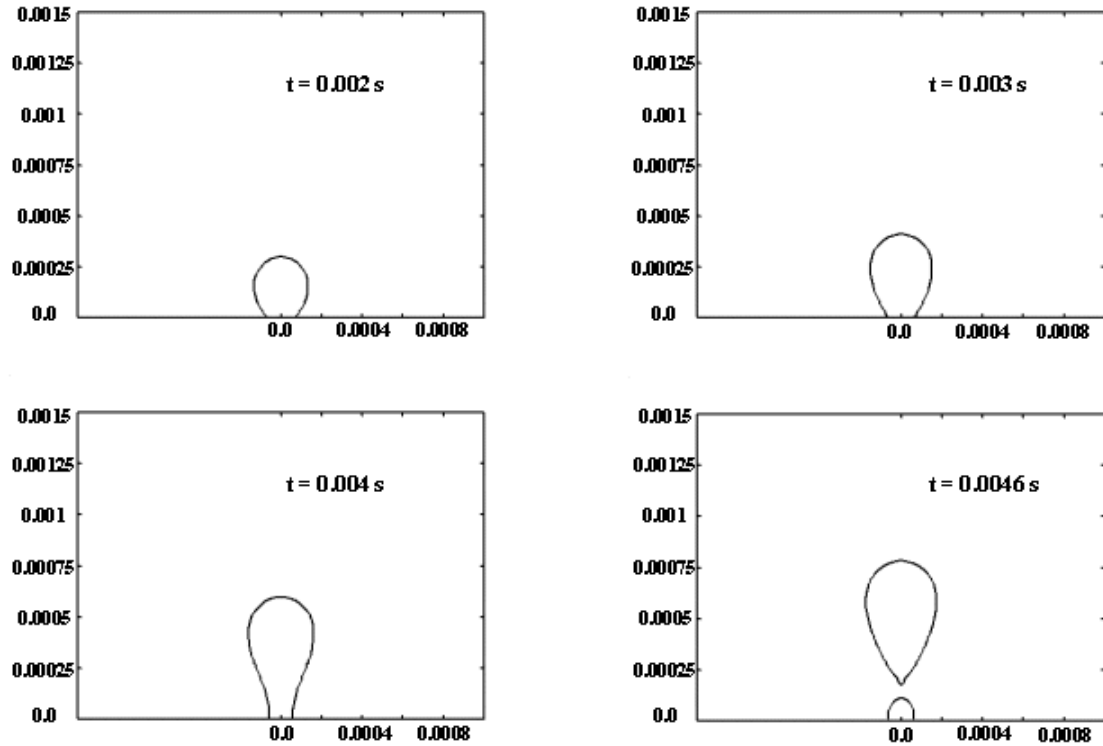


Figure 5.7: Bubble growth from a pore size of 120 μm for $\Delta T = 3 \text{ K}$.

The flow field in and around a bubble during its growth from a 120 μm pore cavity with a wall superheat (ΔT) of 5 K is shown in Figure 5.8. During the early period of bubble growth (a), the liquid around the bubble is pushed out with a circulatory flow pattern being established in the liquid. Figure 5.8 (b) shows the flow pattern around the bubble shortly before detachment. The liquid flow is radially inward in the lower portion of the bubble while the liquid is being pushed outwards in the upper portion of the bubble. The departure process occurs rapidly with the dominance of buoyancy over surface tension force as the bubble base shrinks resulting in bubble detachment.

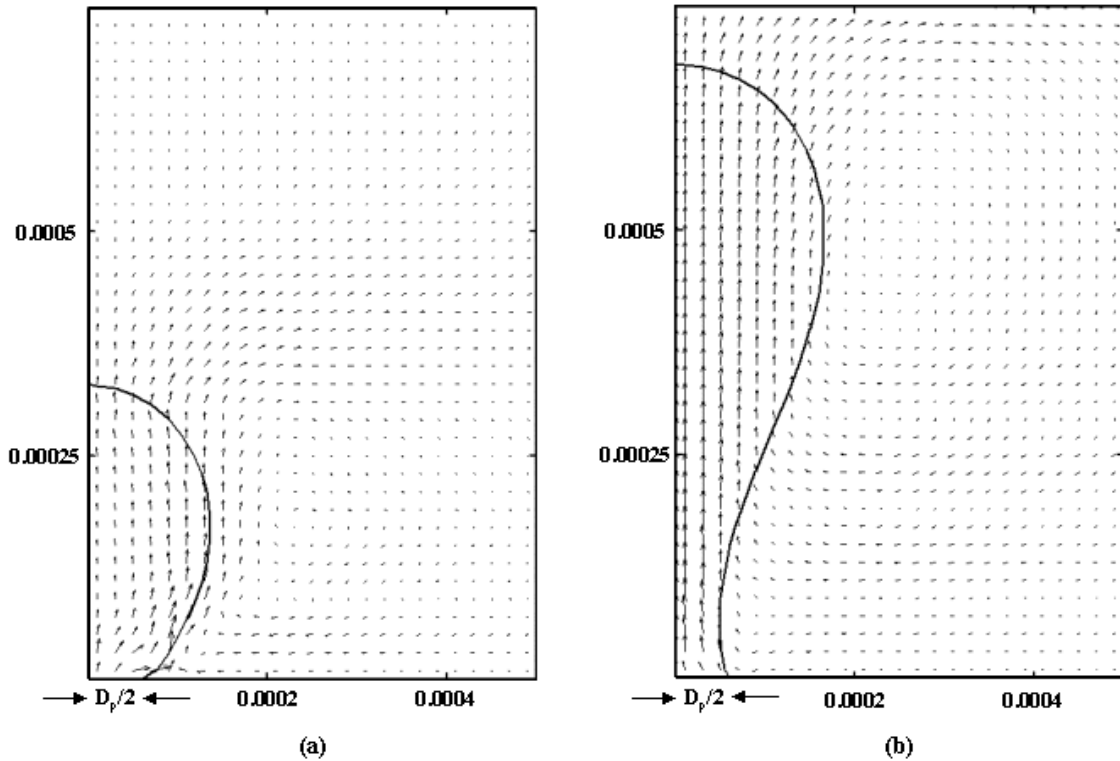


Figure 5.8: Flow patterns during bubble growth for $\Delta T = 5$ K and $D_p = 120$ μm at (a) $t = 0.016$ s and (b) $t = 0.032$ s.

Figure 5.9 shows the bubble growth at different wall super heats after $t = 0.02$ s. Production of vapor in the sub-surface tunnels increases with increase in wall superheat. As a result, the growth period decreases from 46 ms to 32 ms when ΔT is increased from 3 K to 7 K. Figure 5.10 plots the variation of bubble diameter with time for different wall superheat values. The bubble departure diameter increases with wall superheat and matches with the trends seen in experiments (Chien and Webb [1998d], Ramaswamy et al. [2002]).

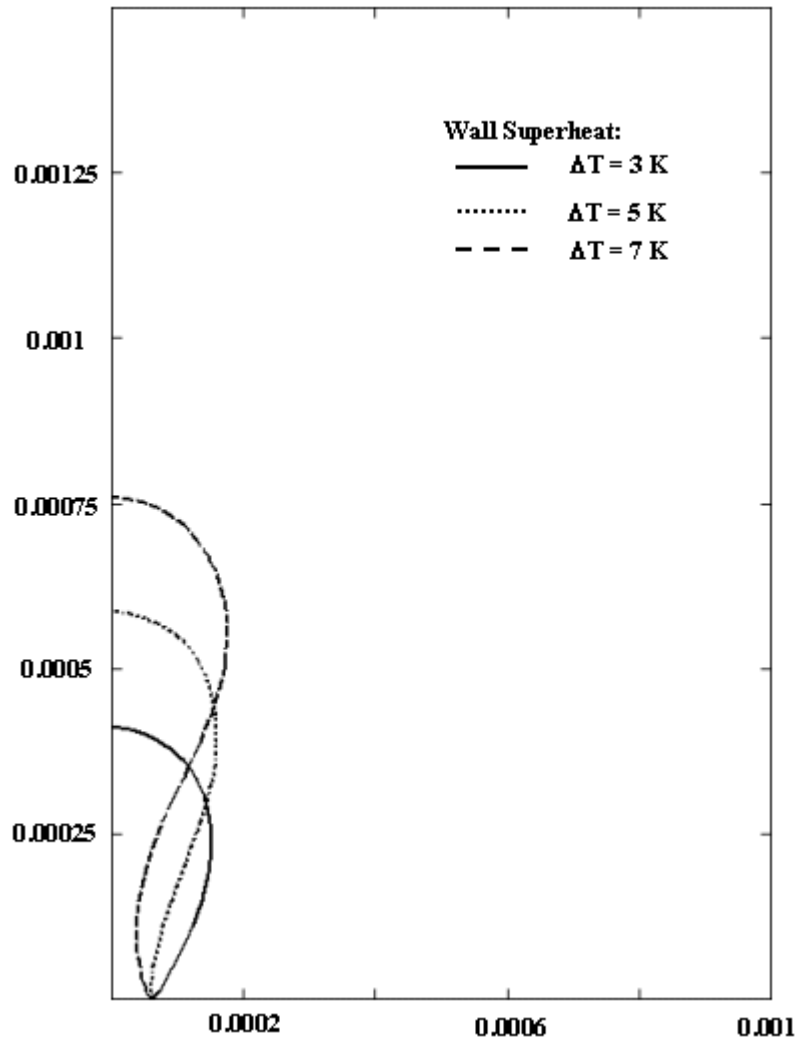


Fig. 5.9: Bubble shape from a 120 μm pore cavity at $t = 0.03$ s for different wall superheat values.

5.6 Summary and Conclusions

- a) Level set formulation, based on second order projection method, was used for simulating two-dimensional boiling from enhanced surfaces. The numerical algorithm handles breaking and merging of interfaces for large density ratio (1000:1) flows without much loss in computational accuracy.

- b) The growth and departure of a bubble from a surface pore occurs through the formation of a neck near the wall. This contradicts the assumption in the semi-analytical model (Chapter 4) with regards to the departing bubble being spherical (cylindrical in 2D) at all times.
- c) Increase in wall superheat results in an increase in the departure diameter and a corresponding decrease in the bubble growth period.

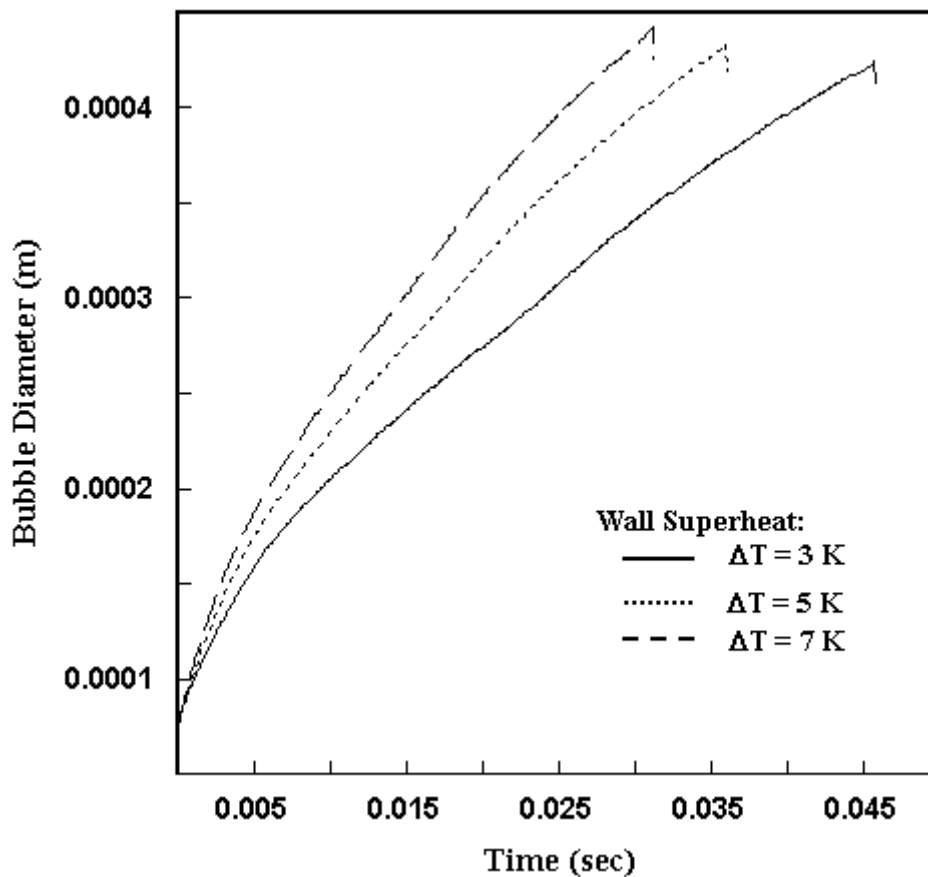


Figure 5.10: Plot of bubble diameter variation with time for growth from a 120 μm cavity at different wall superheats.

CHAPTER 6: SUMMARY, CONCLUSIONS AND RECOMMENDATIONS FOR FUTURE WORK

6.1 Summary

A selected review of cooling solutions for space-constrained applications was presented in Chapter 1. Based on existing literature, liquid-vapor phase change heat transfer was identified as an attractive option for high heat flux cooling applications. A novel two-phase heat spreader with boiling enhancement structures in the evaporator section was fabricated (Chapter 2) and evaluated for different condenser cooling conditions (Chapter 3). A design constraint that ensured flooding of the evaporator under all inclinations resulted in an orientation independent heat spreader. A semi-analytical model was developed based on measured quantities from flow visualization studies reported in the literature (Chapter 4). The semi-analytical model was in turn used in a system level model to predict the spreader plate performance. Also, an effort was made to understand the boiling heat transfer process from structured surfaces through numerical simulation of the phase change process using level set formulation (Chapter 5).

6.2 Conclusions

A novel orientation independent two-phase heat spreader for cooling systems in thin space enclosures was developed. Some of the conclusions arrived from the current study were:

- (a) The three-dimensional structure in the evaporator section of the heat spreader resulted in a 20% increase in thermal performance, when compared to the performance of the spreader plate without the enhancement structure for a forced convection cooling of 1 m/s. The observed enhancement in performance increases to 25% at an air speed of 2 m/s, indicating the dependency of the spreader plate performance on the condenser cooling conditions.
- (b) Lower wall temperatures at the heat spreader can be achieved by either using liquids with lower boiling points or by reducing the starting system pressure. Liquids with lower boiling points or steeper boiling curves result in faster onset of nucleate boiling causing a corresponding lowering of the wall temperature. Similarly, the decrease in saturation temperature at low pressures provides the benefit of lower wall temperatures.
- (c) Significant improvement in heat transfer performance (15 % - 30 %) is achieved by stacking multiple layers to form three dimensional porous enhancement structures. However, an increase in the height results in a fin efficiency effect due to the finite thermal conductivity of the structure material, and the increase in the heat transfer was not proportional to the increase in the surface area.
- (d) Orientation independent performance of the two-phase spreader can be achieved by ensuring that the evaporator section of the spreader plate remains flooded at all orientations. Design constraints on the height of the evaporator and the condenser section of the spreader plate ensure a flooded evaporator at all inclinations in the cold case condition. But this does not remain true with the application of heat flux. Slight deterioration in performance was observed at

high heat fluxes with the 90° orientation due to partial dry out of the enhancement structure.

- (e) A semi-analytical model for boiling from structured surfaces predicts the bubble departure diameter within $\pm 20\%$ and the error in frequency prediction was within $\pm 35\%$. The heat fluxes were predicted within $\pm 30\%$. The maximum error in the heat flux predictions was at the lower wall superheats. The external heat transfer is a function of the nucleation site density, frequency and bubble departure diameter. Individual errors in these three parameters results in a cumulative error for the external heat transfer prediction, which in turn affected the prediction for the total heat flux. The enhanced boiling model was subsequently used in predicting the performance of the forced air-cooled two-phase spreader plate.
- (f) Numerical simulation of bubble growth from structured surface was carried out without any approximation to the bubble shape using level set method. Contribution to the bubble growth through vapor generation from the sub-surface tunnels was accounted through a source term in the mass conservation equations and the contribution from external heat flux was neglected. Simulations show a decrease in the bubble growth period with increase in the wall superheat.

6.3 Recommendations for Future Work

The current study was carried out for a set of parameters that affect the two-phase spreader plate performance. However, further studies are required to complement

the current results and further enhance the understanding of the effect of various parameters. The recommendations for future work are listed below:

- (a) A comprehensive flow visualization study using transparent structured surfaces is required for understanding the evaporation process inside the channels. The frequency and external heat flux prediction depend on the accurate prediction of the tunnel heat transfer. Hence, this component of the model has to be refined the most to result in better prediction of all the other boiling parameters.
- (b) A more accurate description of the bubble growth can be achieved through axisymmetric or three-dimensional computations that also account for the external heat flux by capturing the influence of phase change at the liquid-vapor interface.
- (c) The numerical simulation study focused on the bubble growth on the enhanced surface through the use of correlation for vapor generation in the sub-surface channels. A more appropriate study (Fig. 6.1) beginning with a vapor plug in the channels and studying its growth will provide more insight to the boiling mechanism from structured surfaces. This requires suitable modification of the projection formulation to account for solid surfaces in the computational domain.

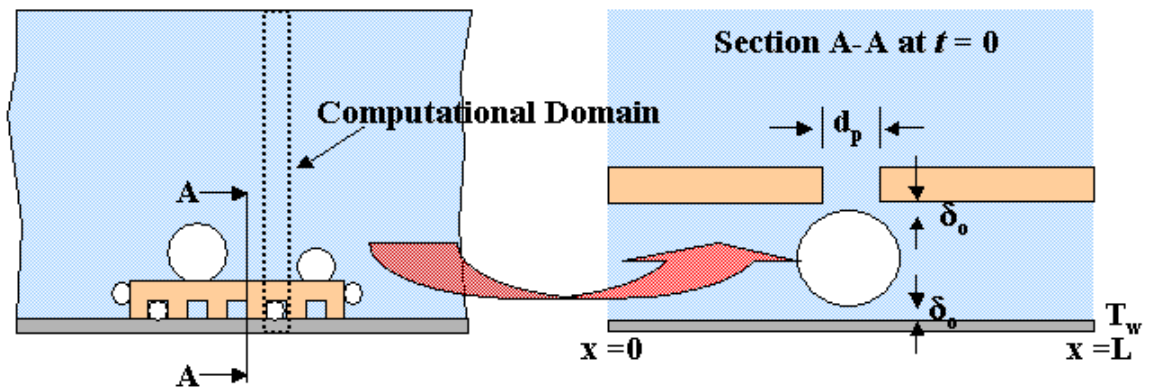


Figure 6.1: Schematic of possible computational domain for numerical simulation of bubble growth from enhanced surface.

REFERENCES

- Almgren, A. S., Bell, J. B., and Szymczak, W. G., "A Numerical Method for the Incompressible Navier-Stokes Equations Based on an Approximate Projection", *SIAM J. Sci. Comput.*, Vol. 17, pp. 358-369, 1996.
- Arshad, J. and Thome, J. R., "Enhanced Boiling Surfaces: Heat Transfer Mechanism Mixture Boiling", *Proceedings of ASME-JSME Therm. Eng. Joint Conf.*, vol. 1, pp. 191-197, 1983.
- Bar-Cohen, A. and Kraus, A.D. (Eds.), *Advances in thermal Modeling of Electronic Components and Systems*, ASME Press, NY/IEEE Press, NY, pp. 76-77, 1993.
- Basiulis, A., Tanzer, H. and McCabe, S., "Thermal Management of High Power PWBs through the Use of Heat Pipe Substrates", *6th Annual International Electronic Packaging Conference*, pp. 501-515, San Diego, CA, 1986.
- Behr, W and Luy, J.F., "High-Power Operation Mode of Pulsed IMPATT Diodes" *IEEE Electron Device Letters*, Vol. 11, pp. 206-209, 1990.
- Bell, J. B., Colella, P., and Glaz, H. M., "A Second-Order Projection Method for the Incompressible Navier-Stokes Equations", *J. Comput. Phys.*, Vol. 85, pp. 257-283, 1989.
- Bell, J. B., and Marcus, D. L., "A Second Order Projection Method for Variable Density Flows", *J. Comput. Phys.*, Vol. 101, pp. 334-348, 1992
- Benson, D.A., Mitchell, R.T., Tuck, M.R., Adkins, D.R. and Palmer, D.W., "Micro-Machined Heat Pipes in Silicon MCM Substrates", *IEEE Multi-Chip Module Conference*, pp. 127-129, Santa Cruz, CA, Feb. 1996.
- Bergles, A. E., "Enhanced Heat Transfer: Endless Frontier, or Mature and Routine?", *Enhanced Heat Transfer*, vol. 6, pp. 79-88, 1999.
- Brackbill, J. U., Kothe, D. B., and Zemach, C., "A Continuum Method for Modeling Surface Tension", *J. Comput. Phys.*, Vol. 100, pp. 335-353, 1992.

Boulton-Stone, J. M., and Blake, J. R., "Gas Bubble Bursting at a Free Surface", *J. Fluid Mech.*, Vol. 254, pp. 437-466, 1993.

Brackbill, J. U., Kothe, D. B., and Zemach, C., (1992), "A Continuum Method for Modeling Surface Tension," *J. of Computational Physics*, Vol. 100, pp. 335-354.

Cao, Y., Faghri, A. and Mahefkey, E.T., "Micro / Miniature Heat Pipes and Operating Limitations", *Heat Pipes and Capillary Pumped Loops*, ASME HTD-Vol. 236, pp. 55-62, 1993.

Chien, L.-H., Mechanism and Analysis of Nucleate Boiling on Structured Surfaces, Ph. D. Thesis, *The Pennsylvania State University*, University Park, PA, 1996.

Chien, L.-H. and Webb, R. L., "A Parametric Study of Nucleate Boiling on Structured Surfaces, Part II: Effect of Pore Diameter and Pore Pitch", *J. Heat Transfer*, Vol. 120, pp. 1049-1054, 1998a.

Chien, L. H. and Webb, R. L., "Visualization Experiments of Pool Boiling on Enhanced Surfaces", *Experimental Thermal and Fluid Science*, vol. 16, pp. 332-341, 1998b.

Chien, L-H., and Webb, R. L., "A Nucleate Boiling Model for Structured Enhanced Surfaces", *Int. J. Heat Mass Transfer*, vol. 41, pp. 2183-2195, 1998c.

Chien, L. H. and Webb, R. L., "Measurement of Bubble Dynamics on an Enhanced Boiling Surface", *Experimental Thermal and Fluid Science*, vol. 16, pp. 177-186, 1998d.

Cornwell, K., Nair, B. G. and Patten, T. D., "Observation of Boiling in Porous Media", *Int. J. Heat Mass Transfer*, vol. 19, pp. 236-238, 1976.

Chorin, A. J., "Numerical Simulation of the Navier-Stokes Equations", *Math. Comp.*, Vol. 22, pp. 745-762, 1968.

Chorin, A. J., "On the Convergence of Discrete Approximations to the Navier-Stokes Equations", *Math. Comp.*, Vol. 23, pp. 341-353, 1969.

Cooper, M. G., and Lloyd, A. J. P., "The Microlayer in Nucleate Boiling", *Int. J. Heat Mass Transfer*, Vol. 12, pp. 895-913, 1969.

Cornwell, K., Nair, B. G. and Patten, T. D., "Observation of Boiling in Porous Media", *Int. J. Heat Mass Transfer*, vol. 19, pp. 236-238, 1976.

Danielson, R. D., Tousignant, L. and Bar-Cohen, A., "Saturated pool Boiling Characteristics of Commercially Available Perfluorinated Liquids", *Proc. ASME/JSME Thermal Eng. Joint Conf.*, Vol.3, pp. 419-430, 1987

Dasgupta, S., Schonberg, J.A., and Wayner, P.C., "Investigation of an Evaporating Extended Menisci Based on the Augmented Young-Laplace Equation", *J. Heat Transfer*, vol. 115, pp. 201-208, 1993

Deshpande, N. V., "Fluid Mechanics of Bubble Growth and Collapse in a Thermal Ink Jet Printer", *SPSE/SPIES Electronic Imaging Devices and Systems Symposium*, January, 1989.

Del-Valle, M., and Kenning, D. B. R., "Subcooled Flow Boiling at high Heat Flux", *Int. J. Heat Mass Transfer*, Vol. 28, pp. 1907-1920, 1985.

Dhir, V. K., Kandlikar, S. G. and Shoji, M., *Handbook of Phase Change: Boiling and Condensation*, Taylor and Francis, NY, 1999.

Eisele, H. and Haddad, G.I., "GaAs TUNNETT Diodes on Diamond Heat Sinks for 100 GHz and Above", *Microwave Theory and Techniques*, Vol. 43, pp. 210-213, 1995.

Fabis, P.M. and Windischmann, E, "Thermal Management Enhancement of GaAs Devices using CVD Diamond Heat Spreaders in a Plastic Package Environment", *Journal of Electronic Packaging*, Vol. 122, pp. 92-97, 2000.

Ghia, V., Ghia, K. N., and Shin, C. T., "High-Re Solutions for Incompressible Flow using the Navier-Stokes equations and a Multigrid method", *J. Comput. Phys.*, Vol. 48, pp. 387-411, 1982.

Ghiu, C.-D., Joshi, Y., and Nakayama, W., "Visualization of Pool Boiling from Transparent Enhanced Structures", *Proceedings of 35th National Heat Transfer Conference*, Vol. 1, pp.697-704, Anaheim, CA, 2001.

Ha, J.M. and Peterson, G.P., "The Heat Transport Capacity of Micro Heat Pipes", *J. Heat Transfer*, Vol. 120, pp. 1064-1071, 1998.

Haider, S.I., "A Theoretical and Experimental Study of Nucleate Pool Boiling Enhancement on Structured Surfaces", Ph.D. Thesis, *The Pennsylvania State University*, University Park, PA, 1994.

Haider, I. And Webb, R. L., "A Transient Micro-Convection Model of Nucleate Pool Boiling on Plain Surfaces", *Int. J. Heat Mass Transfer*, vol 40, pp. 3675-3688, 1997.

Hammel, E.; Holzer, H.; Hanreich, G. and Nicolics, J., "Silicon Substrates with Microwhisiker Structure-An Innovative Heat Spreader Technology for Power Electronics Application", *Proceedings of the SPIE - The International Society for Optical Engineering*, Vol. 3906, pp. 474-479, 1999.

Hopkins, R.; Faghri, A. and Khrustalev, D., "Flat Miniature Heat Pipes with Micro Capillary Grooves", *Journal of Heat Transfer*, Vol. 121, pp. 102-109, 1999.

Hsu, Y. Y., "On the Size Range of Active Nucleation Cavities on a Heating Surface", *Journal of Heat Transfer*, Vol. 84, pp. 207-213, 1962

Incropera, F. P., and DeWitt, D. P., *Fundamentals of Heat and Mass Transfer*, John Wiley and Sons, 1990.

Israelachvili, J., *Intermolecular and Surface Forces*, Academic Press, Florida, 1991.

Jagannadham, K.; "Multilayer Diamond Heat Spreaders for Electronic Power Devices", *Solid State Electronics*, Vol. 42, pp. 2199-2208, 1998.

Judd, R. L., and Hwang, K. S., "A Comprehensive Model for nucleate Pool Boiling Heat Transfer Including Microlayer Evaporation", *J. Heat Transfer*, Vol. 99, pp. 624-629, 1976.

Juric, D., and Trggvason, G., "Computations of Boiling Flows", *Int. J. Multiphase Flow*, Vol. 24, No. 3, pp. 387-410, 1998.

Kline, S.J. and McClintock, F.A., "Describing Uncertainties in Single Sample Experiments", *Mechanical Engineering*, Vol. 78, pp. 3-8, 1953.

Lai, M., Bell, J. B., and Colella, P., "A Projection Method for Combustion in the Zero Mach Number Limit", *Proceedings of the 11th AIAA CFD Conference*, pp. 776 – 783, Orlando, FL, 1993.

Lundgren, T. S., and Mansour, N. N., "Vortex Ring Bubbles", *J. Fluid Mech.*, Vol. 224, pp. 177-196, 1991.

Mikic, B. B. and Rohsenow, W. M., "A New Correlation of Pool Boiling Data and Effect of Heating Surface Characteristics", *J. Heat Transfer*, vol. 91, pp. 245-250, 1969.

Mudawar, I., and Anderson, T.M., "Optimization of Enhanced Surfaces for High Flux Chip Cooling by Pool Boiling," *Trans. ASME J. Electronic Packaging*, v115, pp. 89-100, 1993

Mikic, B.B., and Rohsenow, W.M., "A New Correlation of Pool Boiling Data Including the Effect of Heating Surface Characteristics", *J. Heat Transfer*, vol. 91, pp. 245-250, 1969.

Nakayama, W., Daikoku, T., Kuwahara, H., and Nakajima, T., "Dynamic Model of Enhanced Boiling Heat Transfer on Porous Surfaces, Part I: Experimental Investigation," *J. Heat Transfer*, vol. 102, pp. 445-450, 1980a.

Nakayama, W., Daikoku, T., Kuwahara, H., and Nakajima, T., "Dynamic Model of Enhanced Boiling Heat Transfer on Porous Surfaces, Part II: Analytical Modeling," *J. Heat Transfer*, vol. 102, pp. 451-456, 1980b.

Nakayama, W., Nakajima, T., and Hirasawa, S., "Heat Sink Studs Having Enhanced Boiling Surfaces For Cooling Microelectronic Components," *ASME Paper No.84-WA/HT-89*, 1984.

Oguz, H. N. and Prosperetti, A., "Bubble Entrainment by the Impact of Drops on Liquid Surfaces", *J. Fluid Mech.*, Vol. 203, pp. 143-179, 1990.

Osher, S. and Sethian, J.A., "Fronts Propagating with Curvature Dependent Speed: Algorithm Based on Hamilton-Jacobi Formulations", *Journal of Computational Physics*, vol. 79, pp-12-49, 1988.

Park, J.S.; Choi, J.H.; Cho, H.C.; Yang, S.S. and Yoo, J.S, "Flat Micro Heat Pipe Arrays for Cooling and Thermal Management at the Package", *Proceedings of the SPIE - The International Society for Optical Engineering*, Vol. 4408, pp. 424-429, Cannes, April 2001.

Paul, D. D., Ghiaasiaan, S. M., and Abdel-Khalik, S. I., "On the Contribution of Various Mechanisms to Nucleate Pool Boiling Heat Transfer", *ASME Proc. Pool and External Flow Boiling*, pp. 125-133, 1992.

Peterson, G. P., "Overview of Micro Heat pipe Research", *Applied Mechanics Review*, Vol. 45, pp. 175-189, 1992.

Peterson, G. P., "Modeling, Fabrication and Testing of Micro Heat Pipes: An Update", *Applied Mechanics Review*, Vol. 49, pp. 175-183, 1996.

Puckett, E. G., Almgren, A. S., Bell, J. B., Marcus, D. L., and Rider, W. G., "A high-order projection method for tracking fluid interfaces in variable density incompressible flows", *J. Comput. Phys.*, Vol. 130, pp. 269--282, 1997.

Ramaswamy, C., A Compact Two-Phase Thermosyphon Employing Micro Fabricated Boiling Enhancement Structures, Ph.D. Thesis, *University of Maryland*, College Park, MD, 1999.

Ramaswamy, C., Joshi, Y. and Nakayama, W., "Performance of a Compact Two-Chamber Two-Phase Thermosyphon: Effect of Evaporator Inclination, Liquid Fill

Volume and Contact Resistance”, *Proc. of the 11th International Heat Transfer Conference*, Kyongju, South Korea, Vol. 2., pp. 127-132, 1998.

Ramaswamy, C., Joshi, Y., Nakayama, W. and Johnson, W. B., “High Speed Visualization of Boiling from an Enhanced Structure”, *Int. J. Heat Mass Transfer*, Vol. 45, pp. 4761-4771, 2002.

Ramaswamy, C., Joshi, Y., Nakayama, W. and Johnson, W. B., “Semi-Analytical Model for boiling from Enhanced Structures”, *Int. J. Heat Mass Transfer*, vol. 46, pp. 4257-4269, 2003.

Saraswati, R. and Polese, F.J., “Aluminum Matrix Composite Heat Sinks for Microchips and Microcircuits”, *Proceedings of the SPIE - The International Society for Optical Engineering*, Vol. 3582, pp. 681-686, 1999.

Sepulveda, J.L.; Valenzuela, L. and Wilson, S.W., “Copper / Tungsten Mounts Keep Diode Lasers Cool”, *Laser Focus World*, Vol. 36, pp. 283-288, 2000.

Sharma, P. R., “Determination of Heat transfer rates in Nucleate Pool Boiling of Pure Liquids for a Wide Range of Pressure and Heat Flux”, *Proc. of 11th Int. Heat Transfer Conference*, vo. 2, pp. 467-472, Kyongju, South Korea, 1998.

Son,G., and Dhir, V.K., “Numerical Simulation of Film Boiling Near Critical Pressures with A Level Set Method”, *Journal of Heat Transfer*, Vol. 120, pp. 183 – 192, 1998.

Son, G., Dhir, V.K., and Ramanujapu, N., “Dynamics and Heat Transfer Associated with a Single Bubble During Nucleate Boiling on a Horizontal Surface”, *Journal of Heat Transfer*, Vol. 121, pp. 623 – 631, 1999.

Son, G., Dhir, V.K., and Ramanujapu, N., “Numerical Simulation of Bubble Merger Process on a Single Nucleation Site During Pool Nucleate Boiling”, *Journal of Heat Transfer*, Vol. 124, pp. 51 – 62, 2002.

Sussman, M., Smereka, P., and Osher, S., “A Level Set Approach for Computing Solutions to Incompressible Two-Phase Flow”, *J. of Computational Physics*, Vol. 114, pp. 146 – 159, 1994.

Sussman, M., Fatemi, E., Smereka, P., and Osher, S. J., "An Improved Level Set Method for Incompressible Two-Phase Flows", *J. Computers and Fluids*, Vol. 27, pp. 663--680, 1998.

Sussman, M., Almgren, A. S., Bell, J. B., Colella, P., Howell, L.H., Welcom, M. L., "An Adaptive Level Set Approach for Incompressible Two-Phase Flows", *J. Comput. Phys.*, Vol.148, pp. 81-124, 1999.

Take, K. and Webb, R.L., "Thermal Performance of an Integrated Plate Heat Pipe with a Heat Spreader", *J. Electronic Packaging*, Vol. 123, pp. 189-195, 2001.

Thome, J. R., *Enhanced Boiling Heat Transfer*, Hemisphere Publishing Corporation, NY, 1990.

Unverdi, S. O., and Tryggvason, G., "A Front Tracking Method for Viscous, Incompressible, Multi-Fluid Flows", *J. Comput. Phys.*, Vol. 114, pp. 146-159, 1994.

Wang, D.Y., Cheng, J.G., and Zhang, H.J., "Pool Boiling Heat Transfer from T-Finned Tubes at Atmospheric and Super-atmospheric Pressures," *Phase Change Heat Transfer*, Eds. V.K. Dhir, R. Greif and J. Fillo, ASME HTD Vol. 159, pp. 143 – 147, 1991.

Webb, R.L., *Principles of Enhanced Heat Transfer*, John Wiley & Sons, NY, 1994.

Webb, R.L., and Haider, I., "An Analytical Model for Nucleate Boiling on Enhanced Surfaces," *Pool and External Flow Boiling*, Eds. V.K. Dhir and A.E. Bergles, pp. 345 – 360, 1992.

Welch, S., and Wilson, J., "A Volume of Fluid Based Method for Fluid Flows with Phase Change," *J. Comput. Phys.*, Vol. 160, pp. 662 – 682, 2000.

Xin, M.D., and Chao, Y.D., "Analysis and Experiment of Boiling Heat Transfer on T-shaped Finned Surfaces," AIChE paper, 23rd National Heat Transfer Conference, Denver, Colorado, 1985.

Yoganand, S.N., Jagannadham, K., Karoui, A., and Wang, H., “Integrated AlN / Diamond Heat Spreaders for Silicon Device Processing”, *Journal of Vacuum Science and Technology A*, Vol. 20, pp. 1974-1982, 2002.

You, S.M., (1990), Pool Boiling Heat Transfer with Highly Wetting Dielectric Fluids, Ph.D. Thesis, Mechanical Engineering, *University of Minnesota*, Minneapolis, MN.

Zalesak, S., “Fully Multidimensional Flux Corrected transport Algorithms for Fluids”, *J. Comput. Phys.*, Vol.31, pp. 335-362, 1979.

Zuber, N., “Nucleate Boiling - the Region of Isolated Bubbles - Similarity with Natural Convection”, *International Journal of Heat and Mass Transfer*, vol. 6, pp. 53 – 56, 1963.